2010

Design and critical performance evaluation of horizontal axis hydrokinetic turbines

Suchi Subhra Mukherji

Department:

DESIGN AND CRITICAL PERFORMANCE EVALUATION OF HORIZONTAL AXIS HYDROKINETIC TURBINES

by

SUCHI SUBHRA MUKHERJI

A THESIS

Presented to the Faculty of the Graduate School of the

MISSOURI UNIVERSITY OF SCIENCE AND TECHNOLOGY

In Partial Fulfillment of the Requirements for the Degree

MASTER OF SCIENCE IN MECHANICAL ENGINEERING

2010

Approved by

Arindam Banerjee, Advisor
Rajiv Mishra
K.Chandrashekhara
Jonathan Kimball

ABSTRACT

The current work discusses the hydrodynamic performance of horizontal axis hydrokinetic turbines (HAHkT) under different turbine geometries and flow conditions. Hydrokinetic turbines are a class of zero-head hydropower systems which utilize kinetic energy of flowing water to drive a generator. However, such turbines often suffer from low-efficiency. A detailed computational fluid dynamics study was performed using a low-order k-ω SST (Shear Stress Transport) turbulence model to examine the effect of each of tip-speed ratio, solidity, angle of attack and number of blades on the performance of small HAHkTs with a power capacity of 10 kW. The numerical models (both two-dimensional and three-dimensional) developed for these purposes were validated with blade element momentum theory. The two-dimensional numerical models suggest an optimum angle of attack that maximizes lift as well as lift to drag ratio thereby yielding the maximum power output. In addition, our three-dimensional model is used to estimate optimum turbine solidity and blade numbers that produces maximum power coefficient at a given tip speed ratio. Furthermore, the axial velocity deficit downstream of the turbine rotor provides quantitative details of energy loss suffered by each turbine at ambient flow conditions. The velocity distribution provides confirmation of the stall-delay phenomenon that occurs due to the rotation of the turbine. In addition, it provides further verification of optimum tip speed ratio corresponding to maximum power coefficient obtained from the solidity analysis.

ACKNOWLEDGMENTS

I wish to express my deep sense of gratitude and sincere appreciation to my advisor Prof. Arindam Banerjee who guided me with diligence and patience throughout my thesis. He has always been extremely helpful, encouraging and a constant source of motivation. I would like to thank my committee members Prof. Rajiv Mishra, Prof. K. Chandrashekhara and Prof. Jonathan Kimball for their support and cooperation. In addition, I express my sincere appreciation to Prof. Rajiv Mishra for providing me with helpful suggestions throughout the project. I acknowledge the financial support from the Energy Research and Development Center (ERDC) of Missouri S&T and Office of Naval Research which made this work possible. I would also like to acknowledge my fellow members of Turbulent Mixing and Alternative Energetics Laboratory: Aaron, Raghu, Tim, Nitin, Varun and Pamela for sharing useful thoughts and engaging in fruitful discussions over the duration of this work. Special thanks to Ms. Katherine Wagner and Ms. Vicki Hudgins for their help at various stages of my MS program and with my thesis. I would also like to thank IT helpdesk for the software support function.

Last but not the least, I would like to thank my mother, my elder brother, my grandmother and all my family members for their constant support, cooperation and love; without them none of this would have been possible.

TABLE OF CONTENTS

LIST OF ILLUSTRATIONS

Figure Page

LIST OF TABLES

Table Page

1. INTRODUCTION

1.1. US ENERGY SCENARIO

Over the past decade, there has been a rapid push towards finding new renewable energy resources in order to counter the rapid depletion of fossil fuel reserves. At present, although the entire world is heavily dependent on fossil fuels with 72% of total electricity market share coming from coal, oil and natural gas respectively [2] , the crucial role of renewable energy resources cannot be underestimated for its global environmental concerns and rapid depletion issues. An urgent need to establish environmental friendly, low cost energy supply has therefore, necessitated the exploitation of new renewable energy resources. Hydro, wind, solar, nuclear and bio-fuels are regarded as the primary renewable energy resources which show promising power producing capabilities in present years as well as for next few decades. According to the Annual Energy Outlook, the primary energy consumption in 2008 crossed 99.3 quadrillion BTU of which only 7% was based on renewable energy resources (see Figure 1.1) [1-3]. Even though coal (23%) and petroleum (37%) remains the most important fuels for US electricity generation; the projection over the next 25 years suggests an improved market share of renewable resources to ~ 17% by 2035. However, by this time, energy consumption in the US will increase to 117.8 quadrillion BTU (Figure 1.2) [1-2]. The 2007 US Ocean Wave and Current Energy report by the Electric Power Research Institute (EPRI) estimated nearly 55 GW of new renewable capacity in US by 2020 [4]. Till date, however, the increased usage of efficient renewable energy resources resulted in only 9% overall growth of energy related CO_2 emission (0.4% growth per year) as compared to 14% increase in total energy usage expected over the period of 2008-2035 [1]. On this regard, a proper utilization of the aforementioned renewable technology principles offers a sustainable option to augment traditional energy technologies to meet the need of the present generation without compromising the ability of future generations to meet their own needs.

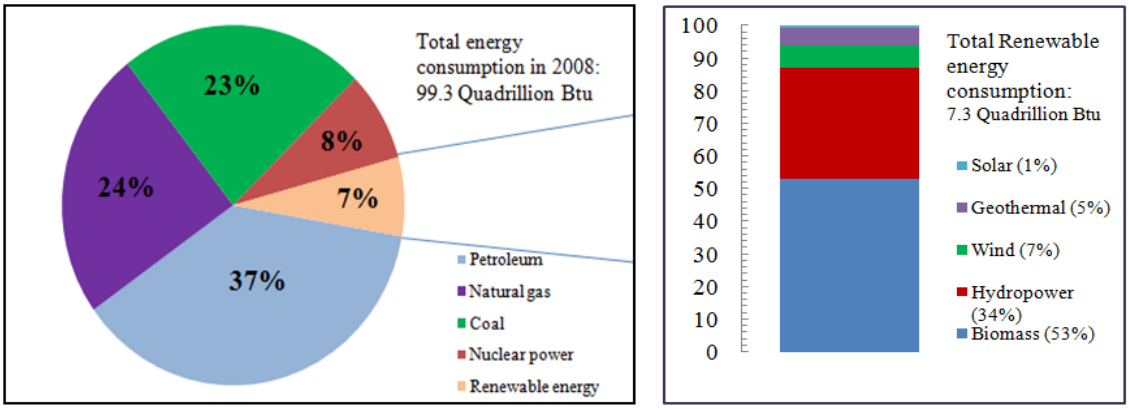

(a) (b)

Figure 1.1. (a) Primary Energy Consumption in USA for the year 2008. (b) Distribution of different renewable energy resources in USA for the year 2008 [1-2]

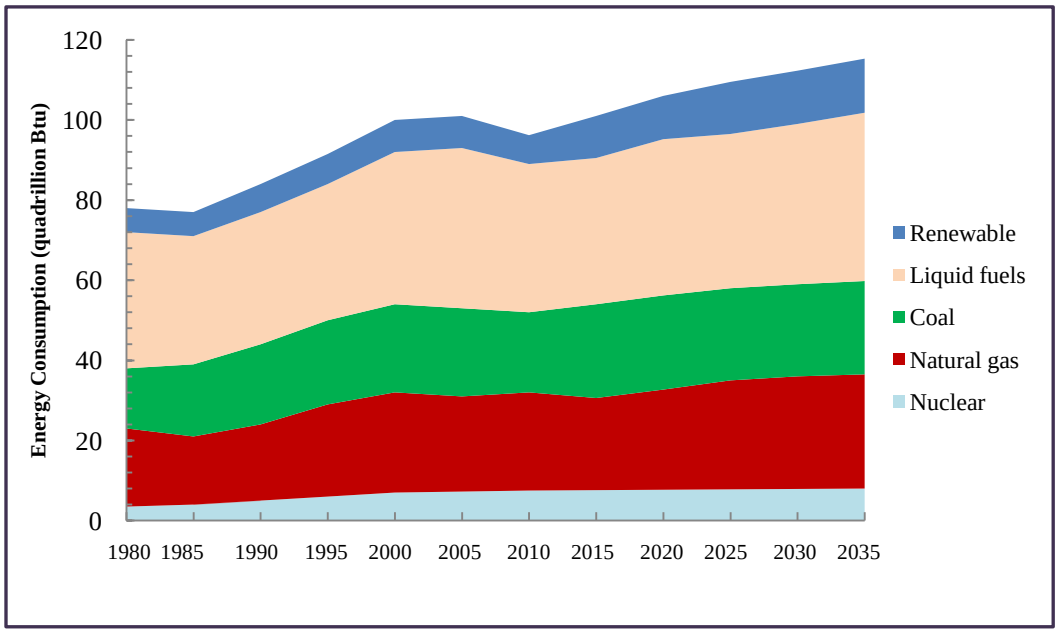

Figure 1.2. Projection of percentage shares of conventional fossil fuels and renewable energy resources for the next twenty five years [1]

1.2. HYDROPOWER: OVERVIEW

Hydropower is considered to be a sustainable energy resource owing to its potential to generate ~ 2 GW of energy utilizing potential energy of water with negligible environmental effect [5]. As seen in Figure 1.1, hydropower delivers 34% of total renewable energy production in USA, the second highest share after biomass (53%) [1-2]. However, the growth rate of large hydropower has declined in recent years as potential sites have already been utilized and new sites are unavailable mostly due to environmental, space and socio-political constraints [6]. Furthermore, the problem is aggravated by the huge construction costs of dams/reservoirs, power stations and other accessories which make it less feasible from an application point of view [7]. In the context of increased usage of alternative energies, focus has shifted to the exploitation of small scale hydropower energy which possesses significant economic advantages in reduced constructional, operational and maintenance costs while providing sufficient flexibility for wide range of application due to its modular and scalable design [8]. Over the last decade, small-scale micro hydropower systems with power output ≤ 20 kW have been primarily designed for low head applications (5-20 m) allowing the flexibility of its application along the entire river [9-12]. The primary limitation of these systems however is governed by its higher installation cost. For sites of a given power, head reduction is associated with increased volumetric flow rate. Therefore the penstocks and turbines need to be of larger size to carry this increased flow which inevitably makes it more expensive on a unit-kW basis compared to traditional higher head sites (dams). In addition, these micro-hydro power plants can only be installed at locations where a static head of water exists (5-20 m), making it suitable for only limited applications. A growing interest has been observed recently in developing turbines which offers an exciting proposition of extraction of energy from river under zero static head – a new class of turbines known as *hydrokinetic turbines* [13-16].

1.2.1. Design configuration of hydrokinetic turbines. Hydrokinetic turbines are designed to be deployed in river streams capturing kinetic energy from flowing water across a rotor which is coupled to an electromechanical energy converter that subsequently generates electricity without any diversion of the flow path (Figure 1.3). The principle of operation of hydrokinetic turbine is similar to wind turbine (Figure 1.4); the only difference being the difference in fluid density (water being 850 times heavier than air). The principle subsystems of a typical hydrokinetic turbine are shown in Figure 1.4 and include [17]:

- Rotor and hub: The rotor consists of the hub and blades of the turbine. The turbine blades are conventionally bolted to the hub. The design of rotor is considered to be a primary challenge from both hydrodynamics and economics standpoint. Details about the turbine blade designs are discussed in subsequent chapters.
- Drive-train: The drive train consists of the rotating parts of the turbine which includes a low speed shaft (on the rotor side), a gearbox, high speed shaft (on the generator side) and support bearings. The purpose of the gearbox is to speed up the rate of rotation of the rotor from a lower value to a rate suitable for driving a standard generator.
- Generator: The generator transforms mechanical energy from the rotor to electrical energy which is then passed on to the grid.
- Nacelle: Nacelle includes the turbine housing and main frame which provides for the mounting and proper alignment of drive-train components. The nacelle cover is hermetically sealed which protects the turbine components from water.
- Diffuser: A diffuser is provided around the hydrokinetic turbine to draw more fluid through it and also increase the available pressure drop across the turbine by recovering some of the velocity head downstream as pressure head. This option is however not used in all available designs on the market.
- Mounting structure: Includes supports and foundation for the entire turbine assembly.

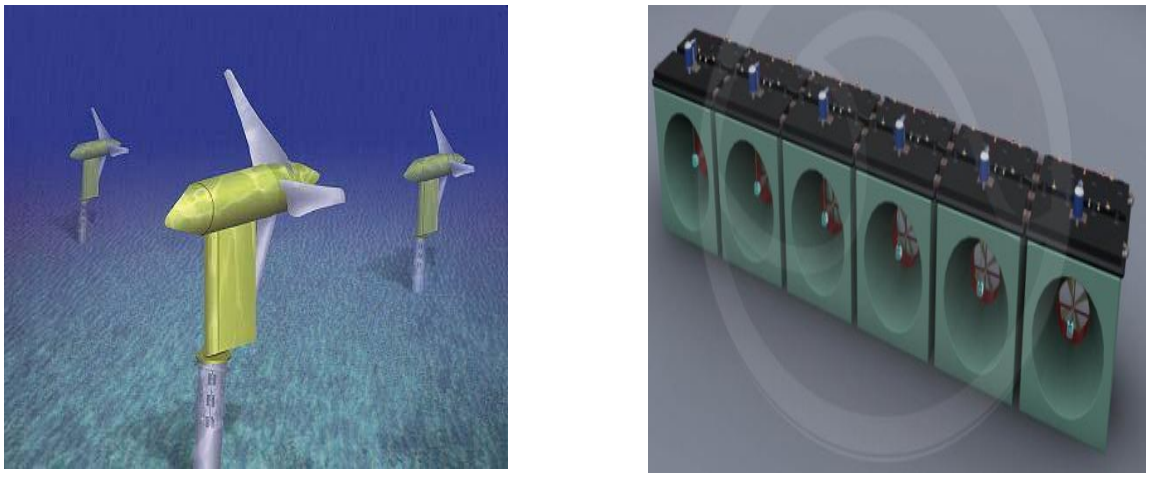

(a) (b)

Figure 1.3. (a) Axial hydrokinetic turbine developed by Verdant Power [15]; (b) arrays of hydrokinetic turbines developed by Hydro Green Energy [17]

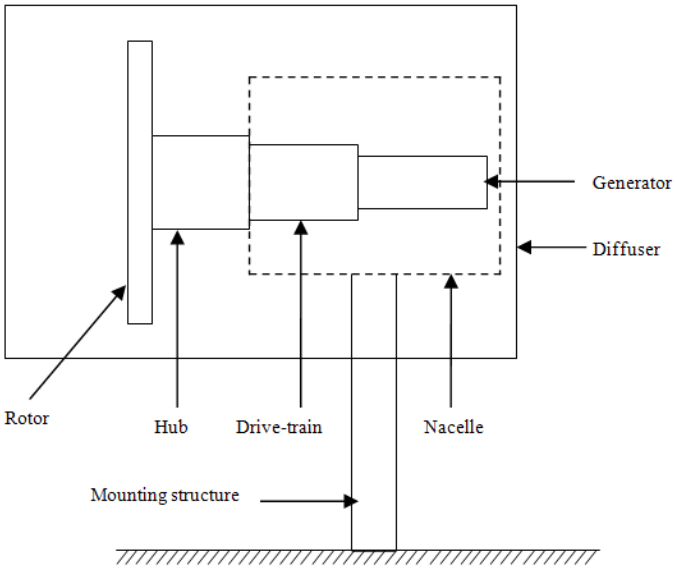

Figure 1.4. Schematic of a hydrokinetic turbine

The US has over 250,000 rivers, with a total of about 3.5 million miles of river banks. The longest river in the US is the Missouri river which is 2,540 miles long [18]. In addition, the Mississippi river, which flows through St. Louis, is the largest in terms of annual volumetric flow rate. Rolla and the Missouri S&T campus are strategically placed as we are at the heartland of the Missouri-Mississippi basin with over 3000 miles of river banks in the state. The placement of hydrokinetic turbines in the surrounding river basins therefore offer significant economic advantages to the local community [19]. From design/implementation point of view, the primary advantages associated with hydrokinetic turbines are:

- No alteration of natural pathways of streams: Unlike wind power, river flow is predictable and unidirectional in nature which eliminates the need of changing the flow direction or additional fast control mechanism (yawing is required in wind turbines) and allows fixed orientation of turbine rotors for long term application.
- Higher level of energy extraction due to near surface placement: The energy flux contained in water streams is dependent on the density of the fluid, cross-sectional area and fluid velocity.

$$P = \frac{1}{2}\rho A V^3 \tag{1.1}$$

  where, ρ is water density (equal to 998.2 kg/m^3), A is turbine swept area and V is the water flow velocity. Therefore, maximum energy can be extracted when the turbine is placed near the fluid surface.
- Minimal civil engineering work: These turbines are conventionally placed on floating pontoons (Figure 1.5), fixed to a structure on the surface or on the river bed (Figure 1.6). This significantly reduces the need of civil engineering work.
- Reduced environmental hazards- In contrast to large or micro hydropower systems, the impact of the hydrokinetic turbines on the river course, ecosystem and wildlife is small due to its compact scalable design.
- Use of available technologies- The basic turbine technologies such as rotor hub and blade, generator and other power convertors are readily available in market which reduces the overall cost of the system and enables lower level of technical sophistication for proper functioning of such turbines.

- Use of channel augmentation- Channel augmentation induces a lower pressure within a constrained area resulting in increased flow velocity. Turbines placed inside such channels will be subjected to higher flow velocity which increases total power capture significantly. These diffuser-augmented systems possess several practical challenges while implementing in a wind turbine due to the tower-head placement, variable orientation and size of the turbines (see Figure 1.7). The implementations of diffusers in hydrokinetic turbine are subjected to lesser hazards due to its unidirectional motion and near surface placement.
- Diversity of applications- The foremost objective of hydrokinetic turbines is production of electricity which have multiple other applications that include water pumping for storage, small industry, irrigation, human consumption and military usage and most importantly zero pollutant emission for generation of same amount of electricity.
- Noise and aesthetics- Unlike wind turbine, underwater installation of hydrokinetic turbines causes no noise disturbance and has negligible visual impact. The impact on river navigation, swimming and boating can be minimized by efficient design. At turbine installation locations, the placement of drawbridges or moveable bridge arrangements can also make unobstructed navigational pathway in rivers.

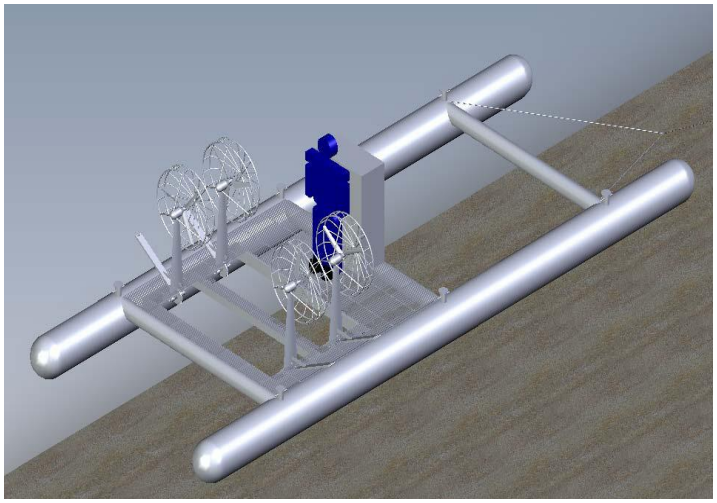

Figure 1.5. Pontoon structure with raised rotor implemented in Alaska river in-stream energy feasibility study [20]. Human figure on pontoon is 6 ft tall

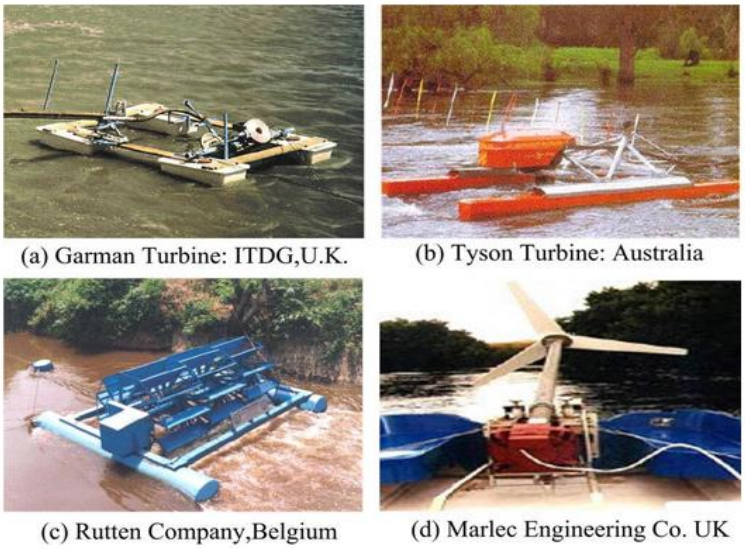

Figure 1.6. Various floating pontoon and fixed structure based hydrokinetic turbine designs developed over the last decade [21]

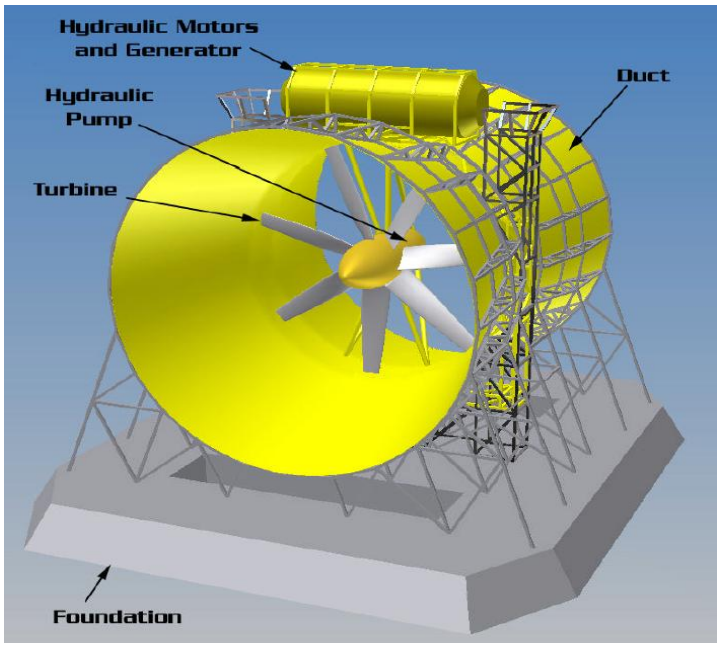

Figure 1.7. Rotech tidal ducted turbine developed by Lunar Energy [22]

1.2.2. Hydrokinetic turbines: Classification. Hydrokinetic turbines are primarily classified based on the direction of rotation of the turbine rotor relative to the water flow at a particular location. Conventionally two types of hydrokinetic turbines are: horizontal axis (Figure 1.8a) where the rotational axis of rotor is parallel to incoming water stream) [16, 20-22] and vertical or cross-flow turbine (Figure 1.8b) where rotational axis is perpendicular to the incoming water stream [6, 23-25]. A comparative analysis between horizontal axis hydrokinetic turbines (henceforth referred to as HAHkT) and vertical/ cross flow turbines has been discussed in Table 1.1. It has been observed that HAHkT has proven to be more efficient than its vertical axis counterpart owing to lower incidence losses, less vibration and more uniform lift forces [14, 17, 26]. The blades in HAHkT move perpendicular to the fluid motion receiving power through whole rotation. In contrast, vertical axis turbines involve various reciprocating actions requiring hydrofoil surfaces to back-track against the fluid for part of the cycle resulting in lower efficiency. In other words, horizontal axis turbine's swept area always faces the fluid as contrary to vertical axis turbines where swept area is perpendicular to the fluid motion. As a result part of the swept area is working while part of it is simply being blown around not at an optimal angle to generate lift resulting in lesser efficiency than HAHkT. In addition, the flexibility of placement of HAHkT to near water surface in rivers, self-starting behavior, absence of shaking force and less usage of materials makes HAHkT to be more efficient than vertical axis hydrokinetic turbines.

This MS thesis research focuses on design and critical performance evaluation of HAHkTs. Our hydrodynamic design of HAHkT illustrates the need of complex blade profiles which increases overall cost of the system due to increased manufacturing costs. Turbine blades are often subjected to steady load due to mean water speed, centrifugal load due to blade rotation and weight of the blades and cyclic or periodic load due to the rotation of the rotor. These loads serve as inputs for the design of blades followed by an appropriate material selection for the component. This problem however can be resolved with advanced composite blade design which produces both structural rigidity and higher hydrodynamic efficiency keeping the overall cost of the system to an optimum limit.

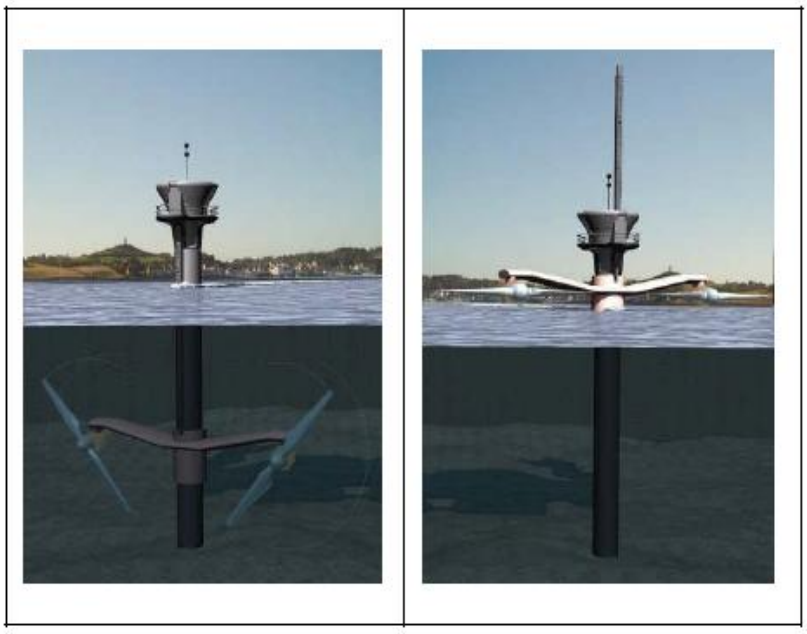

(a)

(b)

Figure 1.8. (a) Horizontal axis hydrokinetic turbine prototype Seagen developed by Marine Current Turbines Limited [30] (b) Vertical axis hydrokinetic turbines developed by New Energy Corporation Inc. [31]

Table 1.1. Comparison between horizontal axis and vertical/cross flow turbines

Characteristics	**Axial turbine**	**Vertical/Cross flow turbines**
Placement	Designed for either bottom structure mounting (BSM), floating (FSM) and near surface arrangements (NSM). This provides flexibility in selection of mounting systems.	These turbines are mainly placed with NSM arrangement allowing the generator to be placed above the water level resulting in lesser power production.
Efficiency	Possess higher efficiency due to lower incidence losses.(A loss that refers to any work done in turning the working fluid from its direction of approach to the rotor to the direction required by the blade passage)	Flow enters over one half of the periphery radially inward, and emerges over its other half flowing radially outward. The velocity near the center of vortex is higher than the velocity further away from center resulting in lower efficiency.
Self starting	Blades are designed to have sufficient taper and twist such that lift forces are exerted uniformly along the blade. Turbines are self starting in nature.	Turbines suffer from low or negative torque at tip-speed ratios which prevent the turbine from accelerating up to operating speeds. This creates a significant problem to low head less water speed sites.
Vibration	Not subjected to any vibration as a result of continuously changing angles of attack.	Turbine blades are subjected to cyclic tangential pulls and generate significant torque ripple at the output. Serious problem if frequency of vibration coincides with the resonant frequency of the support structure.

1.2.3. Hydrokinetic turbines: A technology review. Hydrokinetic power utilization started in 1978 with the development of the Garman Turbine for water pumping and irrigation [27]. Within a period of four years, a total of nine prototypes were built and tested on the White Nile (in Juba, Sudan) having a total of 15,500 operational hours. More recent commercial applications include turbines built by various companies in Europe, USA and Canada such as Rutten Company, Belgium [28], Tyson turbine [29], Marlec Engineering Co. Ltd. [30], Verdant Power [31] and Alternative Hydro Solutions Ltd., Canada [32]. A detailed list of all the existing hydrokinetic projects is given in Table 1.2. The Kinetic Hydro Power System (KHPS) developed by Verdant Power consists of a 5 m diameter three-bladed axial flow turbines rated at 35 kW and operates over a large range of speeds. The turbine rotor is coupled by a step up gear box which drives a grid-connected three-phase induction generator. The turbine operates at 1-2 m/s at a minimum water depth of 6 m in rivers, tidal estuaries and near shore oceans [31]. Hydro Green Energy LLC/Inc. has developed dual duct, axial flow, zero head current-based turbine arrays of 350 kW power capacities operating in river, ocean and tidal settings [33]. The turbines possess high capacity factors (more than 90%) for in-stream river and ocean current applications and surface suspension system provides operational maintenance and safety advantages. Thropton Energy Services manufactured a pontoon-mounted, low power, propeller fan style turbines designed as stand-alone units having maximum power output of 2 kW [34]. Marlec has teamed up their engineering and manufacturing expertise with Thropton Energy Services to develop Amazon Aqua Charger, a battery charging water current turbine. The turbine is lowered into a river or canal deeper than 1.75 m and generates power between water speeds 0.45-1.5 m/s. The tidal turbine generator developed by Clean Current Power Systems consists of a bi-directional ducted horizontal axis turbine with a direct drive variable speed permanent magnet generator. The commercial scale model is 14 m in diameter with 250 kW production capacity. The Underwater Electric Kite (UEK) system employs two axial flow turbines in a side-by-side configuration with each turbine consisting five blades driving single internal generator housed within the nacelle [31, 35]. The turbine is designed to operate in river, tidal and ocean currents and can extract power under operational flow velocity of 0.2 m/s or less.

Table 1.2. Current existing axial hydrokinetic technologies of different companies

Company	Device Type	Anchor system	Current State of the art	Water depth (m)	Water speed (m/s)	Rotor diameter (m)	System Capacity/ Efficiency
Verdant Power	Unducted kinetic hydro power system	Yaw pylon	six full scale turbines in arrays	7	1	5	70MW-hr energy; η = 36%
Hydro Green Energy	Ducted hydrokinetic turbine arrays	Surface suspension system	Operational in river, ocean and tides	1	1-3.5	3.6	Each = 2kW; array = 350 kW /NA
Thropton energy services	Unducted water current turbine	Moored in free stream to a post	Stand-alone units	$\geq$ 1.75	0.5-1.5	1.8-4	2kW capacity; η = 12-14%
Marlec	Unducted Amazon aquacharger	Mount on open moored boat	Power stored in batteries	1.75	0.45-1.5	1.8	500 Watt; η = 12%
Clean Current	Ducted Tidal turbine generator	Pylon, weighted base	Concept design and prototype	15	2.5-4.7	14	1-2 MW; 50% expected
Under-water Electric Kite	Ducted two axial turbines, side by side configuration	Secured to seabed using cable bridle	Design tested at different conditions	NA	2-4	2-5	$\geq$ 0.5 MW depending on site/NA.
PEEHR	Ducted hydroreactor stream accelerator	Extendable yaw piling at the sea floor	Prototypes of impeller tested at rivers	NA	2-3	1.2	15-30kW power capacity /NA
Hydro-helix Energies	Ducted axial turbines in row or matrix	Weighted base	60W model field tested	20	No data	8	250 kW/NA
Swann Turbines	Unducted Axial flow propeller	Extendable yaw pylon	Laboratory / Prototype	NA	1.8-2.8	1	NA/24%

The preliminary investigations on the use of hydrokinetic technologies for in-land water resources have also been conducted by several US Government organizations and laboratories such as US Department of Energy, Idaho National Laboratory [15] and EPRI [36] over last few years. There has been a common agreement from all the sectors regarding the potential of hydrokinetic technology as a next generation renewable energy resources.

1.2.4. Hydrokinetic turbines: Economic standpoint. The primary barrier of increased widespread usage of different renewable resources like solar, nuclear, photovoltaics and fuel cells is associated with the economics involved in its production. Although many of these resources are able to address the global environmental concerns (i.e. reduction of greenhouse gas emission) and energy security concerns, they are much more expensive than conventional fossil fuels like coal and oil making them economically unattractive. The initial cost of energy (COE) calculations for hydrokinetic systems are promising from the economic standpoint, primarily because the overall cost associated with proper functioning of hydrokinetic system is comparatively less compared to a traditional hydro wind turbines of similar capacity. The estimate was based on Simple Payback Period (SPP) for each system which is an indicator of the economic value of the potential project defined as the period of time required for the return on an investment to repay the sum of original investment. A shorter payback period is more preferable on this regard. The construction cost of Hoover dam back in 1930s was around $50 million for generating 2078 MW electricity. Assuming a 5% inflation rate, the cost of power is $1200/kW for construction only. Additional fixed costs associated with building turbine, penstock, power station and manpower result in a SPP of more than 5 years when selling cost is assumed 11 cents/kW-hr. Similar analysis can also be performed for wind turbines where average installation cost is $3000-5000/kW [37]. In comparison, hydrokinetic systems have an overall cost of $2000-2500/kW due to its smaller overall structures. According to Hydro-Volts, a 10 kW hydrokinetic turbine with15 years of product life would result in SPP of 4 years when fixed maintenance cost of $1000/year has been assumed [38]. Similar analysis has been undertaken by Verdant power who

suggests an average 3 year SPP where a large array of turbines justifies more profit compared to other two systems [15]. Figure 1.9 shows production cost comparisons of different energy resources expressed in $/kW-hour [15, 44-48]. It can be observed that hydrokinetic power production from river or tidal current costs less (6 cents/kW-hour) than most other renewable energy resources.

An important comparison can be drawn at this point between a wind turbine and a HAHkT from space and component size consideration as shown in Table 1.3. Assuming an average water speed of 2.5 m/s as observed in most of the rivers, the power density of HAHkT corresponds to 7.8 kW/m^2. In comparison, the power density for wind turbine was 1.1 kW/m^2 for average wind speed of 12 m/s. A power coefficient (C_P) of 0.35 was assumed for all calculations. This illustrates that HAHkTs offer better modularity, scalability and more economic design than a wind turbine for same power capacity. However the technical challenges associated with hydrokinetic turbines needs to be assessed to define appropriate technology classes, design of individual turbine components and power conversion systems for the hydrokinetic technologies before realizing true commercial success of the present technology.

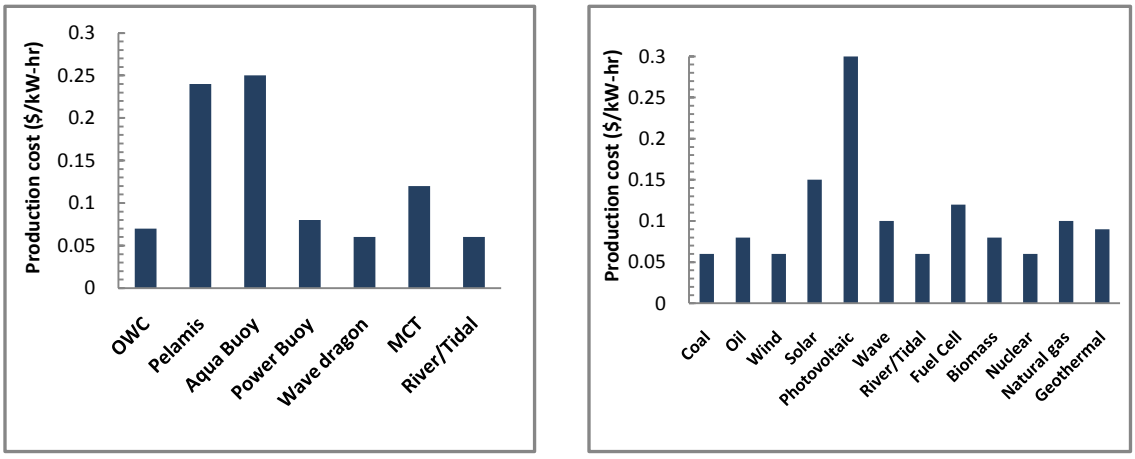

(a) (b)

Figure 1.9. Comparison between production cost of (a) different hydrokinetic systems and (b) different energy sources expressed in $/kW-hour

Table 1.3. Size comparison between wind power and hydrokinetic power systems

Parameter	**Wind Power**	**Horizontal/Vertical axis Hydrokinetic power**		
Power capacity	1 MW	100 units, 10kW each	1000 units, 1 kW each	
Turbine diameter	~ 60 m	2.1m	0.68 m	2.7 m
Flow cut-off speed	V ≈ 12 m/s	V ≈ 2.5m/s	V ≈ 2.5 m/s	V ≈ 1 m/s
Total surface/swept area	A ≈ 2800 m^2	A ≈ 3.7m^2; Total ≈ 370 m^2	0.366 m^2 Total ≈ 366 m^2	5.725 m^2 Total ≈ 5725 m^2
Power Density	1.1 kW/m^2	7.8 kW/m^2	7.8 kW/m^2	0.499 kW/m^2

1.2.5. Hydrokinetic turbines: Technical challenges. As an emerging class of energy resource, the underlying technical challenges and viabilities associated with hydrokinetic technology have not been properly assessed till date. The primary barriers include:

- Availability of resourceful sites: An ideal resourceful site requires detailed investigation of macro scale site assessment with focus on annual energy yield and analysis of river characteristics. The spatial and temporal flow properties of river along with the data regarding river depth, cross-section, navigation and aquatic life is required to extract energy in regular manner.
- Economic considerations: The success of present technology is highly dependent on the economics associated with capital, operations and maintenance cost, design simplicity, and material and labor engagement.
- Optimum systems design: An optimum systems design and configuration of individual units from cost and performance point of view and its compatibility with selected sites is a significant technical challenge for a HAHkT system.

Selection of optimum rotor configuration, number of blades, materials of different turbine components, and design of proper drive-train with suitable gearing and bearing mechanism is of prime interest. Quite often these HAHkTs suffer from low efficiency due to the non-optimized rotor configuration [39]. Moreover, systems performance that includes increased efficiency and better control are two important factors for maximizing power extraction. Among different aspects that are associated with the optimum rotor configuration, rotor hydrodynamics play a key role for efficient operation of hydrokinetic turbines which provides the motivation for the current work.

1.3. THESIS OVERVIEW

One of the primary technical challenges associated with proper implementation of HAHkTs deals with an optimum design of the entire system to maximize its efficiency. The current work aims at a detailed hydrodynamic study of HAHkTs to increase the power coefficient in order to maximize the amount of energy harnessed from the river flow. The overall goal of the current project deals with the thorough understanding of the governing parameters related to the hydrodynamics of HAHkTs and their influence on increasing the efficiency of the system. The thesis is organized as follows: an overview of the functional procedure and related hydrodynamic challenges of HAHkT is discussed in Chapter 2. The formulation of classical hydrodynamic theory, also termed as Blade Element Momentum (BEM) theory is also discussed with focus on useful definitions of all the related governing parameters associated with hydrokinetic system. Chapter 3 details the numerical CFD modeling methods to study the hydrodynamic performance of HAHkTs. The related features of commercial meshing software (GAMBIT 2.4.6) and a finite volume solver (Fluent 12.0) are also discussed. The simulation results are discussed in Chapter 4. The numerical model is validated with results from the BEM model. Furthermore, we discuss the hydrodynamic performance of HAHkT under different turbine geometries and flow conditions. This is followed by a turbine rotor design optimization based on the maximum efficiency of the system. Finally, Chapter 5 discusses our conclusion based on hydrodynamic design and optimization and the future work directions on this topic.

2. HYDRODYNAMICS OF HAHkT

2.1. BASIC OVERVIEW

Hydrokinetic energy conversion devices are designed to be deployed in a stream or current capturing kinetic energy from the flow to power a generator. Although the operational principle of these turbines are similar to that of wind turbines, the higher density of water results in much smaller hydrokinetic units when compared to wind turbine for the same rated power. This kind of small hydrokinetic unit is considered to be environmental friendly with water passing through the generator is being directed back into the stream with relatively small impact on surrounding ecology [40]. Although the density of water is 850 times higher than that of air, the average flow velocities for hydrokinetic turbines are normally an order of magnitude smaller than that of a wind turbine. This results in a similar operational range of Reynolds number (*Re*) for both hydrokinetic and wind systems allowing similar experimental hydrofoil/airfoil data to be used in the design process [40]. Over the years, wind turbines have grown in size with larger rotor and taller tower being designed to take the advantage of faster wind speeds when placed much higher from the surface. In contrast, hydrokinetic turbines are limited in size by the dimensions of the channel in which they are placed. Therefore in order to provide more flexibility with the usage of such turbines, the current work is based on the design of low capacity HAHkTs ($\leq$ 10 kW) due to their usage in military applications for powering advanced posts and civilian usage for power generation in small, rural hard to reach communities. The two most important aspects that are addressed in this work involve a detailed hydrodynamic analysis of hydrokinetic turbines and design optimization based on its performance. Unlike wind turbines, however, hydrokinetic turbines must be designed to avoid cavitation under which low pressures on the hydrofoil's surface results in local boiling of the water and lead to accelerated wear and increased load uncertainty. This chapter deals with various hydrodynamic aspects of HAHkTs that are discussed in the subsequent sections.

2.2. HYRODYNAMICS

2.2.1. Principle features of hydrodynamics. The prediction of hydrodynamic performance of HAHkTs is rendered complicated by several interrelated parameters such as blade profile, blade tip losses, rotational speed of the rotor and angle of attack. In addition flow conditions that include incident flow speed (average free-stream velocity) and free-stream turbulence effects the performance of the turbine. A non-dimensional similarity analysis suggests that overall performance of such turbines is primarily governed by four quantities:

- Reynolds number (*Re*) (i.e. ratio of inertia force to viscous force)
- Tip speed ratio (TSR) (i.e. ratio of blade tip speed to fluid speed)
- Solidity (σ) (i.e. ratio of total blade chord to turbine circumference) and
- Number of blades (*N*)

The effects of each of these quantities need to be carefully analyzed to develop a thorough understanding of the flow hydrodynamics. Depending on inlet flow conditions, the solidity and TSR need to be properly optimized since higher solidity is associated with low TSR and hence lower efficiency due to blade stalling at higher flow incidence. On the contrary, high TSR results in low lift coefficient due to lower AOA resulting in reduction of efficiency.

The flow in turbine blade tip and root region also becomes highly complicated due to the rotational effect of the turbine. Hydrokinetic turbines are associated with a downstream region of reduced flow speed which is termed as wake. A detailed study of near wake velocity distribution plays an important role in determining power extraction and power output for hydrokinetic turbines. Axial velocity deficit, wake width and turbulent properties of wake are associated with flow separation from the surface of the blade which in turn affects the efficiency of the turbine. Unlike wind turbines, hydrokinetic turbines are subjected to cavitation - a condition under which low pressure on the hydrofoil surface can result in local boiling of water and lead to accelerated wear on the blade surface. Cavitation primarily occurs in the region of high flow velocity where the local static pressure falls below the vapor pressure of the fluid resulting in formation of vapor bubbles [26, 41]. As water flows through the blade passage, these

vapor bubbles move to a higher pressure region which is associated with further bubble growth followed by sudden collapse creating extremely high pressure on blade surface. The impact of bubble collapse during cavitation is extremely critical since it erodes the blade solid surface (pitting corrosion) and hence affects smooth turbine operation. Cavitation, therefore, imposes restrictions on blade loading and blade design and proper analysis needs to be performed to avoid cavitation by proper optimization of pressure distribution on the blades to avoid the areas of high relative velocity. Before discussing different hydrodynamic aspects in a more detailed fashion, the definitions and mathematical formulations of the theoretical models are introduced next.

2.2.2. Basic definitions

***Tip speed ratio (TSR)*:** The tip speed ratio is defined as the ratio of the tangential velocity at the tip of the blade to the free stream flow velocity:

$$TSR = \frac{R\Omega}{U} \tag{2.1}$$

where, R is the radius of the turbine blade, Ω is the angular velocity of the rotor and U denotes the fluid velocity. The tip speed ratio dictates the operating condition of the turbine and it affects a number of flow parameters as will be discussed later on.

***Solidity (σ)*:** The turbine solidity is defined as the ratio of blade area to the turbine swept area, i.e. the fraction of the area occupied by the turbine blades:

$$\sigma(r) = \frac{Nc}{2\pi r} \tag{2.2}$$

where, N is the number of blades, c is the chord length and r is an arbitrary radial section along the blade span.

***Lift (L) and Lift Coefficient (C_L)*:** Lift is defined as the force acting on the hydrofoil normal to the free-stream direction. Lift force generated by the blades can be attributed to a distributed bound vortex via Kutta-Joukowski law [42]:

$$L = \rho U \Gamma \tag{2.3}$$

where, ρ is the fluid density and Γ is the circulation or vortex strength around the hydrofoil. The lift force is a consequence of the unequal pressure on the upper and lower hydrofoil surfaces. Lift coefficient is defined by:

$$C_L = \frac{L}{\frac{1}{2}\rho U^2 c} \tag{2.4}$$

Drag (D) and Drag coefficient (C_D): Drag is defined as the force in the flow direction arising from the viscous friction forces at the surface of the hydrofoil and from the unequal pressure on the hydrofoil surface. Drag coefficient is expressed as:

$$C_D = \frac{D}{\frac{1}{2}\rho U^2 c} \tag{2.5}$$

The lift and drag in Eq. (2.4) and Eq. (2.5) denotes forces per unit blade span respectively. These coefficients are again dependent on angle of attack (α) and *Re*. The lift force is a consequence of the unequal pressure on the upper and lower hydrofoil surfaces. However the drag force is due to both viscous friction forces at the surface of the hydrofoil and to unequal pressure on the hydrofoil surfaces facing toward and away from the incoming flow.

Power coefficient (C_P): The power coefficient is defined as the fraction of the power in the water that is extracted by the turbine rotor and is expressed as:

$$C_P = \frac{P}{\frac{1}{2}\rho U^3 A} \tag{2.6}$$

where, *P* is the power output of the turbine and *A* is the cross-sectional area or swept area of the turbine.

Thrust coefficient (C_T): The thrust coefficient for the integral thrust force (*T*) acting on the rotor can be defined as:

$$C_T = \frac{T}{\frac{1}{2}\rho U^2 A} \tag{2.7}$$

Pressure Coefficient (C_p): The pressure coefficient primarily dictates the generation of lift for the hydrofoil and is expressed as:

$$C_p = \frac{P - P_\infty}{\frac{1}{2}\rho U^2} \tag{2.8}$$

where, P denotes pressure at any location of the hydrofoil section and P_∞ denotes free stream ambient pressure.

Axial induction factor (a): It is defined as the fractional decrease in water speed between the free stream flow and the rotor plane:

$$a = 1 - \frac{U_x}{U} \tag{2.9}$$

where, U_x corresponds to axial velocity behind the rotor plane and U is the free stream flow speed. The angular induction factor (a') is similarly defined as the fractional increase in angular velocity due to the increased angular velocity at the blades from the conservation of momentum. These induction factors a and a' are related to the angle of relative water flow (ϕ) by:

$$\tan\phi = \frac{1-a}{(1+a')\lambda_r}; \quad \phi = \theta_P + \alpha \tag{2.10}$$

where, λ_r is the local tip speed ratio at any radial location r from the rotor hub, θ_P is the turbine pitch and α is the angle of attack. Under combined effect of free stream fluid flow and rotation of the turbine, the fluid velocity (U_{rel}) can be expressed as the resultant of both velocity components:

$$U_{rel} = (U^2 + \Omega^2 R^2)^{1/2} \tag{2.11}$$

The axial and tangential velocity components can also be expressed in terms of induction factors:

$$\begin{aligned} U_x &= (1-a)U \\ U_t &= (1+a')r\Omega \end{aligned} \tag{2.12}$$

The magnitudes of these induction factors will be iteratively determined to calculate the power coefficient of the turbine.

2.2.3. Blade element momentum (BEM) theory. The basic performance of hydrokinetic turbines can be modeled using blade element momentum (BEM) theory for high aspect ratio blades. The resulting flow resembles a two-dimensional flow over the blade section before blade stall. In BEM theory, the performance is analyzed along the rotor between radius r and radius ($r+\delta r$) to match the forces generated by the blade elements to the changes in momentum occurring in the fluid flowing through the rotor disc across thickness δr. Applying conservation of linear momentum to the control volume, the differential contribution of thrust (dT) and torque (dQ) can be expressed as a function of axial and angular induction factors:

$$dT = \rho U^2 4a(1-a)\pi r dr \tag{2.13}$$

$$dQ = 4a'(1-a)\rho U \pi r^3 \Omega dr \tag{2.14}$$

The formulation of BEM theory is based on the following assumptions:

(a) There is no hydrodynamic interaction between the blade elements
(b) Incompressible, inviscid and steady state flow field
(c) The forces on the blades are determined by the lift and drag characteristics of the hydrofoil shapes
(d) No cavitation phenomenon

The overall flow phenomenon over a hydrofoil and the associated relationships between various forces, angles and velocities at the turbine blade is shown in Figure 2.1. In the figure, θ_p is the section pitch angle defined by the angle between the chord line and the plane of rotation, θ_{p_0} is the blade pitch angle at the tip, θ_T is the blade twist angle, α is the angle of attack defined by the angle between the chord line and the relative water flow, ϕ is the angle of relative water flow, U_{rel} is the relative water velocity, dF_L is the incremental lift force, dF_D is the incremental drag force, dF_N is the incremental force normal to the plane of rotation and dF_T is the incremental force tangential to the swept area of the rotor. The twist angle is a function of the blade geometry whereas θ_p changes with the position of the blade. If the rotor has N blades, the total normal force on the section at a distance r from the center is given by:

$$dF_N = N\frac{1}{2}\rho U_{rel}^2 (C_L \cos\phi + C_D \sin\phi) c dr \tag{2.15}$$

where, dF_N is the force that contributes to the thrust of the turbine. The differential torque due to the tangential force operating at a distance r from the center is given by:

$$dQ = N\frac{1}{2}\rho U_{rel}^2 (C_L \sin\phi - C_D \cos\phi) c r dr \tag{2.16}$$

Eq. (2.15) and Eq. (2.16) can also be written substituting U_{rel} as a function of free stream water speed:

$$dF_N = \sigma' \pi \rho \frac{U^2 (1-a)^2}{\sin^2\phi} (C_L \cos\phi + C_D \sin\phi) r dr \tag{2.17}$$

$$dQ = \sigma' \pi \rho \frac{U^2 (1-a)^2}{\sin^2\phi} (C_L \sin\phi - C_D \cos\phi) r^2 dr \tag{2.18}$$

where, σ' is the local solidity defined as:

$$\sigma' = \frac{Nc}{2\pi r} \tag{2.19}$$

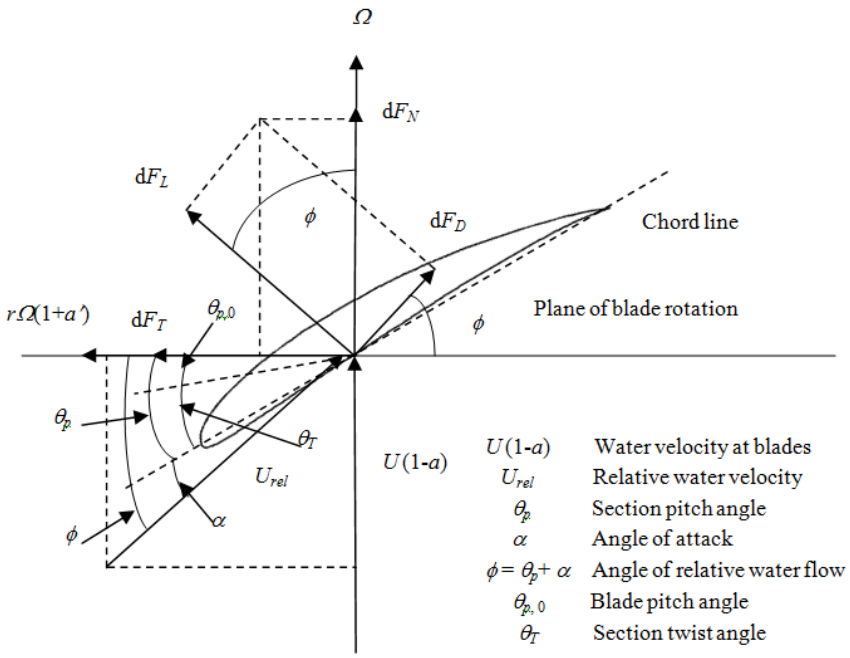

Figure 2.1. Blade geometry illustrating parameters used in BEM theory

According to the blade element momentum theory the differential thrust and torque obtained from momentum theory (Eq. 2.13 and Eq. 2.14) is equated with that obtained using blade element theory (Eq. 2.17) and Eq. 2.18). Assuming $C_D = 0$, the final expressions for a and a' are given as:

$$a = \frac{1}{\frac{4\sin^2\phi}{\sigma' C_L \cos\phi} + 1} \tag{2.20}$$

$$a' = \frac{1}{\frac{4\cos\phi}{\sigma' C_L} + 1} \tag{2.21}$$

The calculation of forces and the induction factors involves an iterative procedure which is repeated until the newly calculated values lie within acceptable tolerance limit. The power contribution from each annulus is given by:

$$dP = \Omega dQ \tag{2.22}$$

Therefore, the power coefficient C_P can be expressed as:

$$C_P = \frac{\int_{r_h}^{R} \Omega dQ}{\frac{1}{2}\rho\pi R^2 U^3} \tag{2.23}$$

where, r_h is the rotor radius at the hub of the blade. Substituting the expression of differential torque in Eq. (2.18) into Eq. (2.23) and performing further simplification, the final expression of C_P is obtained:

$$C_P = \frac{8}{\lambda^2}\int_{\lambda_h}^{\lambda} \lambda_r^3 a'(1-a)\left[1 - \frac{C_D}{C_L}\cot\phi\right] d\lambda_r \tag{2.24}$$

where, λ_h is the local tip speed ratio at the hub.

2.2.4. Limitations and improvements of BEM theory. In BEM theory, the thrust by the blades on the flow is assumed to be constant on an annular element of the rotor disc. This corresponds to an infinite number of blades which in reality is impossible. Moreover, the presence of finite number of turbine blades is associated with tip-loss from blade tips, a phenomenon observed in most wind turbines. The pressure on the suction side of the blade is always lower than that on the pressure side. As a result, water tends to flow around the tip from the lower to upper surface reducing lift and hence lower production near the tip. One of the most convenient methods to include this tip loss effect has been developed by Prandtl [43] who introduced a correction factor *F* into the thrust and torque equations described before. The correction factor is a function of the number of blades, the angle of relative water flow and the position on the blade and expressed as [17]:

$$F = \left(\frac{2}{\pi}\right)\cos^{-1}\left[\exp\left\{-\left(\frac{(N/2)[1-(r/R)]}{(r/R)\sin\phi}\right)\right\}\right] \tag{2.25}$$

where, the angle resulting from the inverse cosine function is assumed to be in radians. As observed in Eq. (2.25) the tip-loss correction factor characterizes the reduction in the forces at a radius *r* along the blade due to the tip-loss at the end of the blade and its value lies between 0 and 1. Incorporation of tip-loss correction factor results in following transformation of the thrust, torque and C_P equations:

$$dT = F\rho U^2 4a(1-a)\pi r\,dr \tag{2.26}$$

$$dQ = 4Fa'(1-a)\rho U\pi R^3\Omega dr \tag{2.27}$$

$$C_P = \frac{8}{\lambda^2}\int_{\lambda_h}^{\lambda} F\sin^2\phi(\cos\phi - \lambda_r\sin\phi)(\sin\phi + \lambda_r\cos\phi)\left[1 - \frac{C_D}{C_L}\cot\phi\right]\lambda_r^2 d\lambda_r \tag{2.28}$$

In BEM theory, the thrust forces determined from the momentum theory are equated with the forces obtained from blade element theory to determine the angle of attack at the blade. The momentum theory is however valid for axial induction factor (a) ≤ 0.5. A low water speed is associated with higher C_T and a. Increase in C_T, however, leads to an increase in the expansion of the wake which results in a velocity jump between upstream and downstream boundary conditions. The free shear layer at the edge of the wake becomes unstable which leads to formation of eddies start behind the rotor.

These eddies transport momentum from the outer flow into the wake and this condition is known as turbulent wake state [44]. The turbulent wake state is characterized by a large expansion of slip stream, turbulence and recirculation behind the rotor. Different empirical relationships have been made for C_T to fit with experimental measurements [45]:

$$C_T = 4aF(1-a) \quad \text{when } a \le a_c \tag{2.29}$$

$$C_T = 4F[a_c^2 + (1-2a_c)a] \text{ when } a > a_c \ \ (a_c \approx 0.2) \tag{2.30}$$

In case of $a > a_c$, the axial induction factor is evaluated as:

$$a = \frac{1}{2}\left[2 + K(1-2a_c) - \sqrt{(K(1-2a_c)+2)^2 + 4(Ka_c^2 - 1)}\right] \tag{2.31}$$

where, $$K = \frac{4F\sin^2\phi}{\sigma' C_N}; \quad C_N = C_L\cos\phi + C_D\sin\phi$$

Glauert's empirical relationship was derived to determine the overall thrust coefficient for a rotor. However, it can also be applied to calculate equivalent local thrust coefficients for each annular blade section which can be expressed as:

$$C_{T_r} = \frac{dF_N}{\frac{1}{2}\rho U^2 dA}; \quad dA = 2\pi r dr dr \tag{2.32}$$

2.2.5. Optimum blade shape design. The optimum blade shape for an ideal rotor needs to be determined taking wake rotation under consideration. For simplicity, the optimization considers $C_D = 0$ and Prandtl tip-loss factor $F = 1$. The optimization is performed by taking the partial derivative of the part of the integral for C_P given in Eq. (2.28) as:

$$\frac{\partial}{\partial\phi}\left[\sin^2(\cos\phi - \lambda_r\sin\phi)(\sin\phi + \lambda_r\cos\phi)\right] = 0 \tag{2.33}$$

Eq. (2.33) on further simplification finally yields the relationship between ϕ and λ_r and the expression of chord length (c) as:

$$\phi = \frac{2}{3}\tan^{-1}\left(\frac{1}{\lambda_r}\right) \tag{2.34}$$

$$c = \frac{8\pi r}{NC_L}(1-\cos\phi) \tag{2.35}$$

2.2.6. Wake region and velocity deficit. The fluid that passes through the cross-section of hydrokinetic turbine rotor exerts a torque on the rotor shaft and an equal and opposite torque is imposed upon the flow stream by the rotating blades. Consequently, the fluid rotates in a direction opposite to that of the rotor at the downstream location. The angular momentum is therefore, increased in the wake as a result of which fluid particles possess tangential velocity component in addition to the stream-wise flow component. In basic momentum theory, the fluid that passes through the rotor disc undergoes an overall change in velocity and a rate of change momentum, which arises from the pressure difference inside the rotor disc; whereas, the pressure outside the streamtube remains atmospheric. When wake rotation is introduced, the tangential component of the rotor wake flow produces an increase of its kinetic energy which is compensated by an additional fall in the static pressure (δp_r) to that of the one-dimensional theory [46]:

$$\delta p_r = \frac{1}{2}\rho\left(2\Omega a' r\right)^2 \tag{2.36}$$

Across the rotor, the value of angular induction factor (a') changes from 0 at the upstream of the rotor (no rotation) to a different value at the immediate downstream due to the tangential component ($2\Omega a' r$). Although the axial induction factor (a) for maximum power extraction is same for rotating as well as non rotating wake cases, a' varies with the radial position. The tangential velocity increases with decrease in radius and therefore the pressure also decreases creating the radial pressure gradient. This radial pressure gradient balances the centrifugal force on the rotating fluid. The pressure drop across the rotor disc caused by the rate of change of axial momentum adds to the pressure drop associated with the rotation of the wake. The usable part of the total available energy is therefore reduced resulting in smaller power coefficient when compared with linear momentum theory.

The wake of a turbine is conventionally divided into a *near wake* and a *far wake*. The near wake region is considered as the area one rotor diameter downstream to the rotor plane where the turbine geometry determines the shape of the flow field and the performance of the turbine. The near wake region is associated with reduced water speed and the velocity deficit is normally attained after one to two rotor diameters downstream.

Here the axial pressure gradient is primarily responsible for the development of the wake deficit. The effect of the number of blades, blade hydrodynamics including stalled flow, three-dimensional flow characteristics and tip vortices are the primary features in near wake region [47]. The far wake is the region beyond the near wake (Figure 2.2), where the focus is given on the mutual influence of the turbines when they are placed in cluster. In the far wake region, the actual rotor shape becomes less important, and more emphasis is given on wake modeling, wake interference (wake farms), turbulence modeling and other topological effects. The difference in velocity between the water inside and outside the wake results in a shear layer, which thickens as it moves downstream. As the thrust on the rotor increases, the wake velocity starts decreasing which ultimately results in larger shear due to the increased difference in flow velocities inside and outside the wake. For very high rotor loading, a large amount of kinetic energy of the incoming flow is converted to the large scale turbulent motion, leading to the turbulent wake state. The mixing of lower velocity fluid in the wake with the higher velocity outside the wake allows the momentum transfer which ultimately results in expansion of the wake and reduction of the velocity deficit. In brief, the near wake research is focused on the performance and physical process of power extraction whereas the far wake research is more focused on the mutual influence of individual turbines when they are placed in clusters. Under the clustered condition, the incident flow over the affected turbines has a lower velocity and higher turbulence intensity which results in lower power production and increase in unsteady loads.

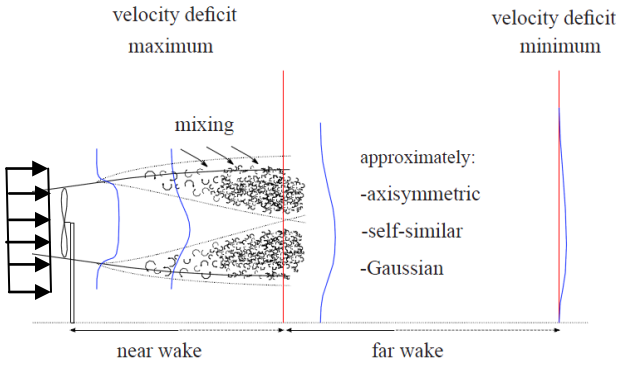

Figure 2.2. Velocity profile in the wake of a wind turbine [53]

2.2.7. Static and dynamic stall. The fundamental principle associated with the flow dynamics of hydrokinetic turbines is similar to the flow over a hydrofoil with the incoming flow at a given angle of attack (α) produces C_L to rotate the turbine blades. At low to moderate angle of attack, C_L varies linearly with α, where the flow moves smoothly over the hydrofoil and is attached over most of the surface as shown in Figure 2.3a. However as α becomes large, the flow tends to separate from the top surface (see Figure 2.3b), creating a large wake behind the hydrofoil. Inside the separated region, the flow starts recirculating and part of the flow moves in a direction opposite to the free-stream producing a reversed flow condition. This separated flow is caused by the viscous effects on the suction surface of the hydrofoil as a consequence of which lift is decreased and drag is increased for flows having high α. The total drag is composed of two individual components: the first one is termed as skin friction drag which is defined as the component of the integral of the shear stress over the body in the drag direction; the other drag is termed as pressure drag due to separation which is defined as the component of the integral of the pressure distribution over the body in the drag direction [48]. Under this condition, the hydrofoil is said to be stalled and the maximum value of C_L occurs just prior to the onset of stall. Beyond the static stall a substantial loss of C_L occurs with significant increase in C_D which governs the operating condition of α during fluid flow.

The flow in the hydrokinetic turbine blade tip and root region is three-dimensional in nature. Under the combined effect of centrifugal force along the blade span-wise direction and coriolis force in the chord-wise direction, the flow separation from the upper surface of the blades gets postponed as a result of which a much higher lift is achieved when compared to two-dimensional data. This phenomenon is termed as dynamic stall where rotation of turbine has a beneficial effect in delaying flow separation to a point further downstream toward the trailing edge of the hydrofoil.

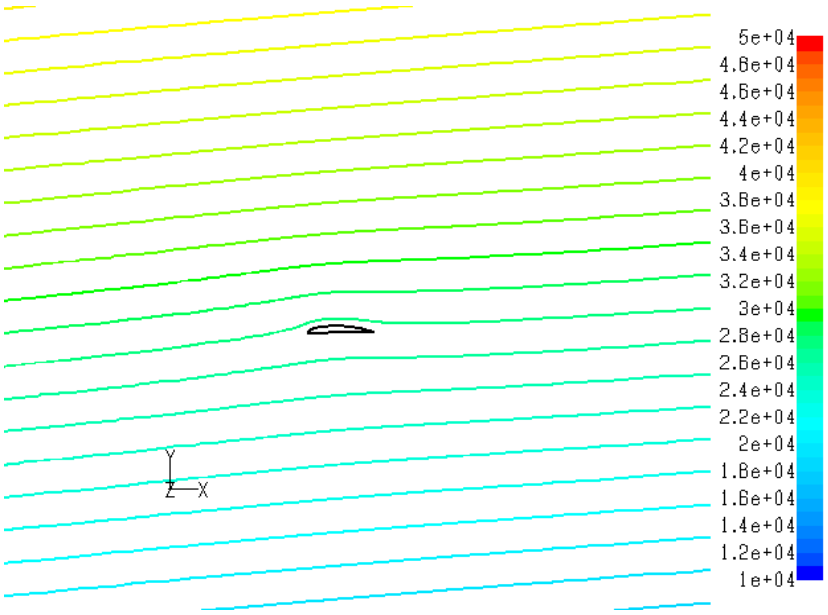

(a)

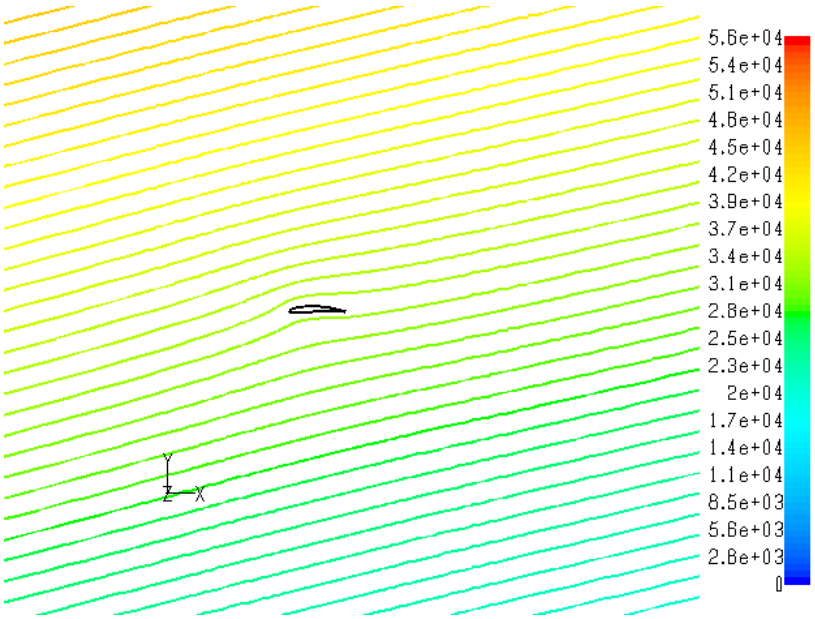

(b)

Figure 2.3. Contours of stream-functions (in kg/s) for flow over a hydrofoil under (a) attached flow condition at $\alpha = 2^{\circ}$ and (b) separated flow condition at $\alpha = 14^{\circ}$

2.3. PREVIOUS WORK

Over the last decade several experimental and numerical investigations have been reported on hydrokinetic and marine current turbines from the perspective of better understanding of flow dynamics and influence of the non dimensional parameters on the performance of the turbine. Consul discussed the influence of solidity on the increased performance of a cross flow turbine using two dimensional numerical simulation [25]. They performed full turbine unsteady CFD simulations using one equation Spalart-Allmaras (SA) and k-ω Shear Stress Transport (SST) turbulence models (k refers to turbulent kinetic energy and ω refers to specific dissipation rate) to evaluate C_L and C_D. The modeling results were compared with Darrieus turbine configurations tested at Sandia National Laboratory. An increase in maximum power coefficient with an increase in blade number was found which implies that with greater solidity the entire power curve shifts to a lower TSR value. Hwang performed two-dimensional simulations as well as experiments to understand the effect of variation of number of blades, chord length, TSR and shape of the hydrofoil on the overall performance of a cross-flow turbine [6]. A similar increase in the power coefficient at a lower TSR with increased rotor solidity was also found. In addition, the experiments showed good agreement with numerical results with an under-prediction of generated power due to the additional drag forces. Batten discussed the effect of blade pitch angle and changes in camber on stall performance and cavitation delay in marine current turbines [16, 21]. Myers performed BEM calculations and experimental study to determine power output over a range of flow speeds and blade pitch for horizontal axis marine current turbines [20]. Although their pre-stall power measurements agreed well with BEM theory, the post-stall measurements were over-predicted, primarily due to the failure of the theoretical model to accurately predict stall-delay under rotational motion. Although not investigated for HAHkT, near wake aerodynamics play a crucial role on the performance and physical processes of power extraction from the rotor rotation [44, 47, 49-50] in wind turbines. Vermeer [47] and Hu [49] showed helical curve trace from wind turbine blade tips with the wake rotation opposite to that of rotor. The axial velocity distribution and turbulence levels in the wake have also been discussed. In addition, Vermeer also discussed the formation of tip and root vortices based and the velocity and vorticity distribution over the wind

turbine blades based on the experiments. The properties of the tip vortices were investigated to determine the physical behavior of the wind turbine rotor with focus on wake expansion, vortex spiral twist angle and the strength of the tip vortex spiral itself. Wake characteristics of a horizontal axis marine current turbines have also been discussed by Myers and Bahaj [51] who indicated increased surface turbulence from water surface elevation measurement. Hu also performed the fundamental study of stall delay phenomenon for horizontal axis wind turbines by employing boundary layer analysis, numerical simulation and experimental measurement [52]. No extensive study has been reported till date that discusses the effect of solidity, angle of attack, blade number and stall delay for HAHkTs since these hydrokinetic turbines are comparatively newer concept and fundamental performance characteristics of HAHkT is yet to be properly analyzed.

2.4. PRESENT WORK

The objective of our present work focuses on detailed numerical investigation for performance evaluation of HAHkTs with ≤ 10 kW power capacities that extracts kinetic energy from river flows with an average depth of 5-10 meters. The optimum operating conditions and geometric characteristics of HAHkTs are determined using computational fluid dynamics (CFD) analysis. The purpose of the study is two-fold:

(a) It lays a strong foundation for designing a HAHkT system of 10 kW capacity with optimum geometric and performance characteristics, and

(b) Provides quantitative details regarding the maximum amount of power that can be extracted from a given flow condition using such turbines.

Conventional BEM theory assumes an equilibrium between the difference in momentum far upstream and far downstream and the forces acting on the rotor blades which is valid only when the flow is steady. However, the present case where the flow is highly unsteady, the dynamic nature of the inflow needs to be taken into account in order to accurately predict the turbine performance. In addition, results from BEM theory are generally in good agreement with field measurements for attached flow conditions. At higher flow velocities, BEM theory shows substantial discrepancies related to lack of the model in predicting stall effects [53-55]. Under deep stall, BEM theory fails to predict the power output with an acceptable accuracy. This is due to the fact that the present

condition cannot be modeled by static, two-dimensional hydrofoil data. Under fluid flow separation in the boundary layer, the outward span-wise flow generated by centrifugal and coriolis force decreases the boundary layer thickness, resulting in the lift coefficient being higher than that obtained from measurements for a non-rotating blade. As a remedy, a full description of the fluid flow field around such turbines can be done by solving Navier-Stokes equations subjected to unsteady inflow and rotational effects. The foremost step for designing a hydrokinetic system consists of selection of topology which includes rotor axis orientation, rotor speed, design tip speed ratio, solidity and number of blades selection. The present work therefore discusses the effect of these parameters on hydrodynamic performance evaluation for small HAHkTs. The detailed differential equations governing the fluid flows, Navier-Stokes equations, and the numerical methodology associated with the hydrodynamic modeling of HAHkT is discussed in the next chapter.

3. NUMERICAL MODELING OF HAHkT

3.1. COMPUTATIONAL FLUID DYANAMICS

Computational Fluid Dynamics (CFD) is a branch of fluid mechanics that uses numerical techniques and algorithms to solve the differential equations governing the fluid flow motion. With the revolutionary improvement in the computer capability over the last two decades, it has become more feasible in today's world to use CFD to solve problems that involves multiple non-linear differential equations. The CFD technique has acquired increased interest in recent years with focus in turbo-machinery due to its advanced capability of solving variety of fluid flow problems in different applications as it offers quite a few advantages. CFD is faster and cheaper which results in considerable reduction in time and costs when compared with comparable experimental methods. The assessment of different solutions can be made in the early phase of the design process, thus eliminating the tedious experimental procedure for all the models [56]. A full-size experimental study is hard to perform in some cases for which CFD modeling is an ideal tool. The numerical models of the physical problem often produce accurate and reliable results (when undertaken with necessary caution) due to the mathematical improvement of solution schemes and use of different physical models. The current work consists of numerical modeling of HAHkT using a commercial CFD code (Fluent 12.0). The entire modeling contains three phases which are conventionally used for any fluid flow problem:

(a) ***Preprocessor***: Here the physical problem is implemented into the mathematical model. The computational domain is then defined and divided into a certain number of elements which constitute the mesh or grid. This is followed by the setting of fluid properties and boundary conditions on the computational domain. Conventionally larger number of mesh elements produces more accurate results. However as higher number of elements is also associated with more CPU effort and computational time, grid convergence study is performed to determine the optimum number of mesh elements that will produce accurate results with

reasonable computational time and power. For the present work, GAMBIT 2.3.16 was used as the preprocessor to create the geometrical model.

(b) ***Solver***: The numerical solution algorithm is the basis of a CFD code. The operating procedure for a CFD solver consists of three major steps: the problem unknowns are modeled by means of simple analytical functions; the governing equations are discretized for the fluid flows and modified by substituting the above mentioned functions and finally solving the algebraic system of equations. The present study uses a commercial finite volume CFD code Fluent 12.0 which perform the following operations [56]:

- Division of domain into discrete control volumes using a computational grid
- Integrate the governing equations over each control volume within the computational domain. Here the integral forms of the conservation equations are applied to the control volume defined by a cell to obtain the discrete equations for the cell.
- Discretize the flux terms (which deal with convection and diffusion processes) using finite difference approach to obtain an algebraic system of equations for the discrete dependent variables such as velocities, pressure, temperature and other conserved scalars and finally
- Solve the algebraic system of equations with iterative methods.

In brief the CFD code finds a numerical solution such that mass, momentum, energy and other relevant quantities are being conserved for each cell where the value corresponds to the value of the flow variables at the cell centers and values at other locations are obtained by suitable interpolation. The finite volume technique can be readily applied to any general cell shape in two-dimensional and three-dimensional domain and obtain the discretized equations for mass, momentum and energy [57].

(c) ***Post-processing***: This section includes the solver output which consists of set of solution variables associated to the given grid nodes or volumes. The data is collected and processed in a suitable fashion in order to produce a physical representation of the solution. Primarily post-processing includes domain and grid

visualization, iso-surface, vector and contour plots of solution variables, two-dimensional and three-dimensional plots and path-lines and particle tracking for a fluid flow problem.

3.2. REYNOLDS AVERAGING AND TURBULENCE MODELING

For all fluid flow problems, the mathematical model is bases on the fundamental mass, momentum and energy conservation equations. The equations for conservation of mass or continuity can be written as:

$$\frac{\partial u_i}{\partial x_i} = 0 \tag{3.1}$$

The conservation equation for momentum can be expressed as [58]:

$$\rho \frac{\partial u_i}{\partial t} + \rho u_j \frac{\partial u_i}{\partial x_j} = -\frac{\partial p}{\partial x_i} + \frac{\partial \tau_{ij}}{\partial x_j} \tag{3.2}$$

where, p is the pressure, ρ is the density of the fluid and τ_{ij} is the viscous stress tensor defined by:

$$\tau_{ij} = 2\mu S_{ij}; \quad S_{ij} = \frac{1}{2}\left(\frac{\partial u_i}{\partial x_j} + \frac{\partial u_j}{\partial x_i} \right) \tag{3.3}$$

where, μ is the effective molecular viscosity and S_{ij} is the strain rate tensor. Eq. (3.2) is commonly known as Navier-Stokes equation. The difficulty associated with turbulence modeling using CFD arises from the fact that turbulent flows exhibit much small scales than laminar flows (scales at which energy dissipation takes place) which results in extremely finer small scale structures at higher Reynolds number (*Re*). However, the time-dependent solutions of the Navier-Stokes equations for high *Re* turbulent flows in complex geometries require the smallest scales of the motions to get resolved for the entire domain. Resolving all turbulent scales of smallest eddies amounts to huge computational power which is practically not feasible. Therefore closure models have been constructed to represent the behavior of small scales using Reynolds Averaged Navier Stokes (RANS) schemes [44, 59]. In RANS methods, the turbulent fluctuations are averaged and this modeling approach is widely employed to most of the practical engineering applications due to the reduction of computational power and resources. Fluent 12.0 was chosen for performing three-dimensional numerical simulations and pre-

processor GAMBIT was employed for building geometry and mesh generation. A variety of RANS closure models are available in Fluent which includes Spalart Allmaras, k-ε (ε is the dissipation) and its variants such as Renormalization group (RNG) k-ε and Realizable k-ε, k-ω and its variant such as k-ω SST and Reynolds stress model (RSM). All these models find separate applications in various engineering field depending on the nature of the problem. However, the choice of an appropriate turbulence model for simulating rotating HAHkT will be discussed in subsequent sections of this chapter.

In Reynolds averaging, the solution variables in the exact Navier-Stokes equations are decomposed into the mean and fluctuating components. For velocity components:

$$u_i = \bar{u}_i + u_i' \tag{3.4}$$

Substituting expressions of this form for the flow variables into the instantaneous continuity and momentum equations and taking a time average yields the ensemble-averaged continuity and momentum equations which can be expressed as [60]:

$$\frac{\partial \rho}{\partial t} + \frac{\partial}{\partial x_i}(\rho u_i) = 0 \tag{3.5}$$

$$\frac{\partial}{\partial t}(\rho u_i) + \frac{\partial}{\partial x_j}(\rho u_i u_j) = -\frac{\partial p}{\partial x_i} + \frac{\partial}{\partial x_j}\left[\mu\left(\frac{\partial u_i}{\partial x_j} + \frac{\partial u_j}{\partial x_i} - \frac{2}{3}\delta_{ij}\frac{\partial u_l}{\partial x_l}\right)\right] + \frac{\partial}{\partial x_j}(-\overline{\rho u_i' u_j'}) \tag{3.6}$$

where, δ_{ij} is the kronecker delta function. Eqs. (3.5) and (3.6) are called Reynolds-averaged Navier-Stokes equations with the same general form as the instantaneous Navier-Stokes equations with the velocities and other solution variables now representing ensemble-averaged values. Additional Reynolds stress term (last term) appeared in Eq. (3.6) represents the effect of turbulence which needs to be modeled in order to obtain a closure equation.

3.3. MODELING TECHNIQUES

3.3.1. Choice of reference frame. Conventionally Fluent solves the equations of fluid flow in an inertial (stationary) reference frame. However, the numerical modeling of HAHkT is complicated due to the rotation of the turbine blades coupled with turbulence and stall effects. A moving reference frame was therefore, incorporated to take the blade rotation into account and transform the unsteady flow in an inertial (stationary) frame to a steady flow in the non-inertial (moving) frame. When a moving reference frame is activated, the equations of motions are modified to incorporate the additional acceleration terms which occur due to the transformation from the stationary to the moving reference frame. Solving these equations in a steady state manner, the flow around the moving parts can be modeled. The schematic of the transformation from inertial (stationary) coordinate system to non-inertial (rotating) coordinate system is shown in Figure 3.1. When the equations of motion are solved in the rotating reference frame, the equations are computed using relative velocity formulation. For the relative velocity formulation, the governing equations of an incompressible fluid flow for a steadily rotating frame can be written as:

Conservation of mass:

$$\nabla \cdot \vec{U}_r = 0 \tag{3.7}$$

Conservation of momentum:

$$\rho\left[\frac{\partial}{\partial t}(\vec{U}_r) + \nabla \cdot (\vec{U}_r \vec{U}_r) + (2\vec{\Omega} \times \vec{U}_r + \vec{\Omega} \times \vec{\Omega} \times \vec{r})\right] = -\nabla p + \nabla \cdot \tau_r \tag{3.8}$$

where, $\vec{U}_r$ is the relative velocity viewed from rotating reference frame, Ω is the rotational speed of the turbine, $\rho(\vec{\Omega} \times \vec{\Omega} \times \vec{r})$ is the centrifugal force and ∇p is the pressure gradient across the turbine. The viscous stress tensor (τ_r) is defined as:

$$\tau_r = \mu_{eff}\left[(\nabla \vec{U} + \nabla \vec{U}^T) - \frac{2}{3}\nabla \cdot \vec{U} I\right] \tag{3.9}$$

where, U is the absolute fluid velocity and I is the identity tensor. The molecular viscosity (μ_{eff}) is the sum of the dynamic viscosity (μ) and turbulent viscosity (μ_t); μ_t being calculated from a representative turbulence model.

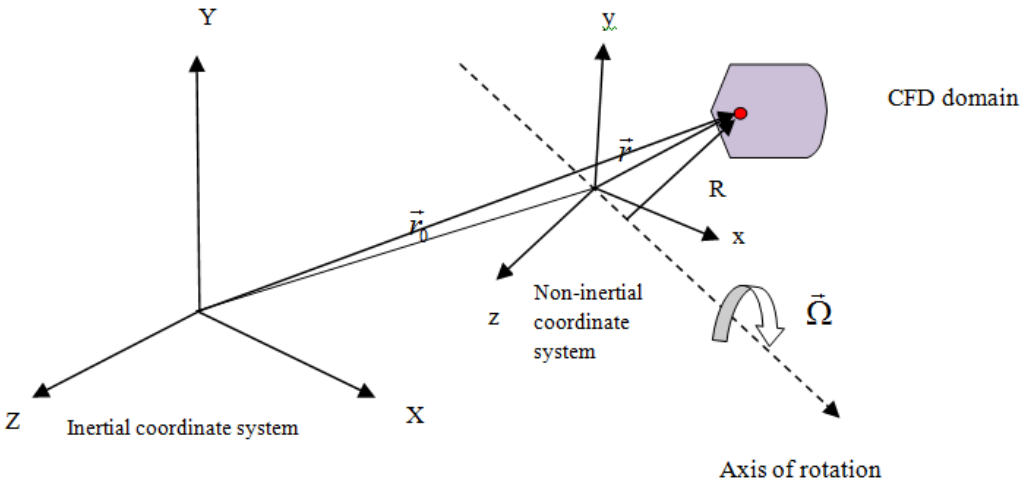

Figure 3.1. Schematic of inertial and non-inertial reference frame

3.3.2. Turbulence models. The Reynolds averaged approach to turbulence modeling as discussed in §1.2 requires that the Reynolds stresses in Eq. (3.6) are appropriately modeled. A common method employs the Boussinesq hypothesis [59] to relate the Reynolds stresses to the mean velocity gradients:

$$-\rho u_i' u_j' = \mu_t \left(\frac{\partial u_i}{\partial x_j} + \frac{\partial u_j}{\partial x_i} \right) - \frac{2}{3} \left(\rho k + \mu_t \frac{\partial u_k}{\partial x_k} \right) \delta_{ij} \tag{3.10}$$

where, k is the turbulent kinetic energy. The Boussinesq hypothesis is used in different turbulence models such as one equation Spalart-Allmaras model and two-equation models such as k-ε and k-ω models where ε is the turbulence dissipation rate and ω is the specific dissipation rate. The advantage of this approach is the relatively low computational cost associated with the computation of the turbulent viscosity μ_t [57]. For the present study, three turbulence models were chosen due to their superiority from other models in providing accurate flow-field predictions under adverse pressure gradient and separated flow conditions both of which are prevalent in HAHkTs [44, 47, 57, 61-63]. A brief summary of all the three models are discussed below.

Spalart-Allmaras model: The Spalart-Allmaras model [64-65] is a one-equation model for the transport of kinematic eddy (turbulent) viscosity. The model is effectively a low-

Re model, requiring the viscosity affected region of the boundary layer to be properly resolved. The transport equation for ν_t is given as:

$$\frac{\partial}{\partial t}(\rho \nu_t) + \frac{\partial}{\partial x_i}(\rho \nu_t u_i) = G_\nu + \frac{1}{\sigma_{\nu_t}}\left[\frac{\partial}{\partial x_j}\left\{(\mu + \rho \nu_t)\frac{\partial \nu_t}{\partial x_j}\right\} + C_{b2}\rho\left(\frac{\partial \nu_t}{\partial x_j}\right)^2\right] - Y_\nu + S_{\nu_t} \tag{3.11}$$

where, G_ν is the production of turbulent viscosity, Y_ν is the destruction of turbulent viscosity that occurs in the near-wall region due to wall blocking and viscous damping, σ_{ν_t} and C_{b2} are the constants, ν is molecular kinematic viscosity and S_{ν_t} is a user-defined source term. The model is designed specifically for aerospace applications involving wall-bounded flows and has been shown to give good results for boundary layers subjected to adverse pressure gradients. In recent times the model is also gaining popularity in the turbomachinery applications.

Realizable k-ε model: The *k-ε* model is a semi-empirical two-equation model based on model transport equations for the turbulence kinetic energy (*k*) and its dissipation rate (ε). This is the simplest complete model of turbulence in which the solution of two separate transport equations allows the turbulent velocity and length scales to be determined independently [66]. The basic assumption of the *k-ε* model is that the flow is fully turbulent and the effects of molecular viscosity are negligible which limits the model for fully turbulent flows. The Realizable *k-ε* model is a recently developed model which differs from the standard *k-ε* model in two important ways: The Realizable *k-ε* model contains a new formulation for the turbulent viscosity. A new transport equation for ε has been derived from an exact equation for the transport of the mean-square vorticity fluctuation. The modeled transport equations for *k* and ε in the Realizable *k-ε* model can be expressed as:

$$\frac{\partial}{\partial t}(\rho k) + \frac{\partial}{\partial x_j}(\rho k u_j) = \frac{\partial}{\partial x_j}\left[(\mu + \frac{\mu_t}{\sigma_k})\frac{\partial k}{\partial x_j}\right] + G_k + G_b - \rho\varepsilon - Y_M + S_k \tag{3.12}$$

$$\frac{\partial}{\partial t}(\rho \varepsilon) + \frac{\partial}{\partial x_j}(\rho \varepsilon u_j) = \frac{\partial}{\partial x_j}\left[(\mu + \frac{\mu_t}{\sigma_\varepsilon})\frac{\partial \varepsilon}{\partial x_j}\right] + \rho C_1 S\varepsilon - \rho C_2 \frac{\varepsilon^2}{k + \sqrt{\nu\varepsilon}} + C_{1\varepsilon}\frac{\varepsilon}{k}C_{3\varepsilon}G_b + S_\varepsilon \tag{3.13}$$

$$C_1 = \max\left[0.43, \frac{\eta}{\eta+5}\right]; \quad \eta = S\frac{k}{\varepsilon}; \quad S = \sqrt{2S_{ij}S_{ij}}$$

In these equations, G_k represents the generation of turbulent kinetic energy due to the mean velocity gradients, G_b is the generation of turbulent kinetic energy due to buoyancy, Y_m represents the contribution of the fluctuating dilatation in compressible turbulence to the overall dissipation rate, C_2 and $C_{1\varepsilon}$ are constants, σ_k and σ_ε are the turbulent Prandtl numbers for k and ε respectively and S_k and S_ε are user defined source terms. Details of the model can be found in the original paper [57, 67]. The Realizable k-ε model provides superior performance for flows involving rotation, boundary layers under strong adverse pressure gradients, separation and recirculation.

***k*-ω SST (Shear Stress Transport) model**: In the k-ω turbulence models the transport equation of the turbulent kinetic energy is solved together with the equation of the specific rate of dissipation of turbulent kinetic energy defined as $\omega = \varepsilon / k$. The model performs well with fee shear flows, flat plate boundary layer flows, adverse pressure gradient flows and separated flows. The k-ω SST model is based on the robust and accurate combination that uses k-ω model in near wall region [59] and k-ε model in far field region [57, 62, 68]. For flows having adverse pressure gradients, the level of eddy viscosity primarily determines the accuracy of the turbulence model in predicting flow separation. Since the standard k-ω model fails to predict pressure induced separation, the model is reconstructed enforcing Bradshaw's observation that turbulent shear stress is proportional to the turbulent kinetic energy in the wake region of the boundary layer [62]. Therefore, using the k-ω formulation, the model solves for the transport of turbulent shear stress which controls the level of eddy viscosity in the outer part of boundary layer. However, since the k-ω model has strong sensitivity to the free-stream value outside the boundary layer, a transformed k-ε model is applied on the far wall region due to its insensitive nature to free stream turbulence [61-62]. The governing equations for k-ω SST model is given by the following equations:

$$\frac{\partial}{\partial t}(\rho k) + \nabla\cdot(\rho k\vec{U}) = \tau_{ij}\nabla\vec{U} - \beta^*\rho\omega k + \nabla\cdot\left[(\mu+\sigma_k\mu_t)\nabla k\right] \tag{3.14}$$

$$\frac{\partial}{\partial t}(\rho\omega) + \nabla\cdot(\rho\omega\vec{U}) = \frac{\gamma}{\nu_t}\tau_{ij}\nabla\vec{U} - \beta\rho\omega^2 + \nabla\cdot\left[(\mu+\sigma_\omega\mu_t)\nabla\omega\right] + 2(1-F_1)\rho\sigma_{\omega 2}\frac{1}{\omega}\nabla k\nabla\omega \quad (3.15)$$

where F_1 denotes the blending function which is designed in such a manner that it assumes the value of unity inside the viscous sub-layer where original k-ω model is activated and it gradually switches to zero in the wake region where transformed k-ε model is activated.

$$\psi = F_1\psi_1 + (1-F_1)\psi_2 \quad (3.16)$$

where, ψ is the constant for the k-ω SST model when ψ_1 corresponds to the constants of k-ω model and ψ_2 corresponds to k-ε model constants. The model constants for k-ω are defined as follows:

σ_{k1} = 0.85, $\sigma_{\omega 1}$ = 0.5, β_1 = 0.075, a_1 = 0.31, β^* = 0.09, κ = 0.41, $\gamma_1 = \beta_1/\beta^* - \sigma_{\omega 1}\kappa^2/\sqrt{\beta^*}$

The eddy viscosity is defined as: $\nu_t = \frac{a_1 k}{\max(a_1\omega;\Phi F_2)}$ where Φ is absolute value of vorticity and F_2 is given by: $F_2 = \tanh(\arg_2^2)$; $\arg_2 = \max(2\frac{\sqrt{k}}{0.09\omega y};\frac{500\nu}{y^2\omega})$; here y is the distance between two immediate cell surfaces. The model constants for k-ε model are defined by: σ_{k2} = 1.0, $\sigma_{\omega 2}$ = 0.856, β_2 = 0.0828, β^* = 0.09, κ = 0.41, $\gamma_2 = \beta_2/\beta^* - \sigma_{\omega 2}\kappa^2/\sqrt{\beta^*}$ along with: $\nu_t = \frac{k}{\omega}$; $\tau_{ij} = \mu_t(\frac{\partial U_i}{\partial x_j} + \frac{\partial U_j}{\partial x_i} - \frac{2}{3}\frac{\partial U_k}{\partial x_k}\delta_{ij}) - \frac{2}{3}\rho k\delta_{ij}$;

$\arg_1 = \min[\max(\frac{\sqrt{k}}{0.09\omega y};\frac{500\nu}{y^2\omega});\frac{4\rho\sigma_{\omega 2}k}{CD_{k\omega}y^2}]$ where δ_{ij} is Kronecker delta function and $CD_{k\omega}$ is the positive portion of the cross-diffusion term that appeared while transforming k-ε model into a k-ω formulation for far wall region:

$CD_{k\omega} = \max(2\rho\sigma_{\omega 2}\frac{1}{\omega}\frac{\partial k}{\partial x_j}\frac{\partial\omega}{\partial x_j}, 10^{-20})$. These features make the k-ω SST model more accurate and reliable for adverse pressure gradient flows which are prevalent in HAHkTs.

3.3.3. Flow domain generation and boundary conditions. The present study assumes steady, incompressible flow where numerical solutions were carried out for both two-dimensional and three-dimensional flow geometries using FLUENT 12.0. The geometrical models for two-dimensional (stationary) and three-dimensional (rotating) boundary conditions were created using the preprocessing tool GAMBIT. The choice of hydrofoil for HAHkT is primarily governed by the geometry that that produces maximum lift coefficient (C_L) as well as maximum lift to drag ratio (C_L/ C_D) under the operating range of *Re*. Increase in curvature on the upper (suction) surface of the hydrofoil increases the camber which ultimately results in increased C_L for a given *Re*. To validate this, two different hydrofoils NACA-2412 [6] and SG-6043 were chosen for two-dimensional numerical simulations. As per the name convention, NACA-2412 hydrofoil has 2% camber on its suction surface with maximum camber present at 0.4 times chord length (c) measured from the leading edge and thickness of the hydrofoil being 12% of c. Previous studies have also used SG-6043 airfoil for the design of small wind turbines due to its capability of producing large C_L/ C_D in the *Re* range of 10^5-10^6 [69-71]. Since the *Re* for our case also lies within this range, the SG-6043 airfoil was selected another hydrofoil for the HAHkT blades. This blade, however, has 6% camber which generates more lift and thereby increases the performance of the hydrofoil. The computational domain for both hydrofoils along with specified boundary conditions is shown in Figure 3.2. The hydrofoil coordinates were imported from the hydrofoil geometry database [72] and the mesh was created using structured quadrilateral cells around the hydrofoils. The computational domain is assumed to be sufficiently large compared to the chord length (c) to enable larger area of flow visualization around the hydrofoil. The geometry contains approximately 1.9×10^4 quadrilateral cells across the domain which extends up to 20 chord lengths away from the hydrofoil in the horizontal direction and 12 chord lengths away in vertical direction. A finer mesh has been applied on the vicinity of the hydrofoil to obtain better flow characteristics and flow orientation very near to surface. Quadrilateral elements were used to mesh the entire geometry to ensure uniform aspect ratios of cells across the domain. Grid resolution requirements were well established by keeping small enough initial normal spacing from the hydrofoil surface yielding y^+ ($= \rho u_\tau \Delta y/\mu$) < 5, where u_τ is the friction velocity and Δy is the cell size.

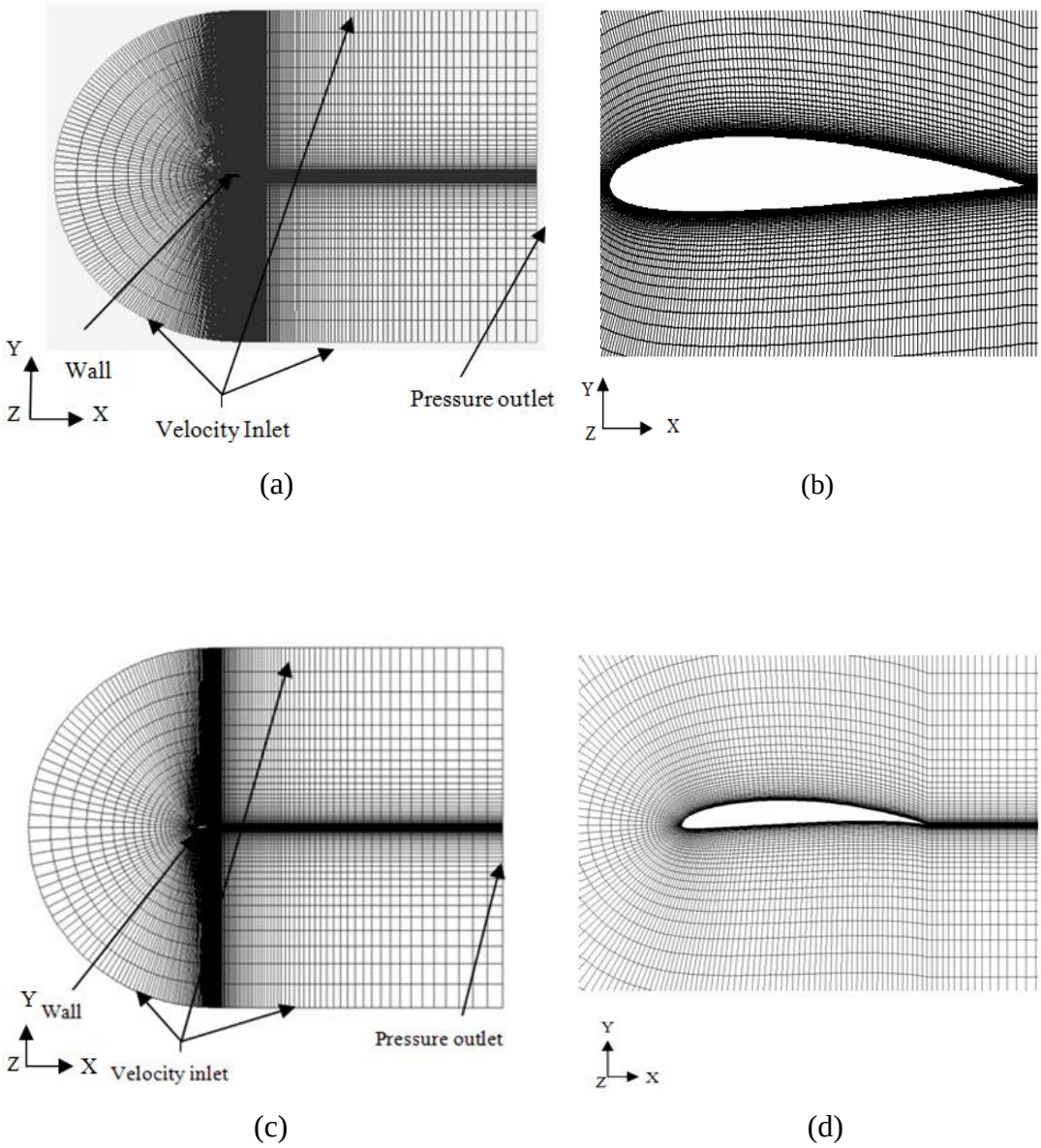

Figure 3.2. Two-dimensional domain along with boundary conditions for (a) NACA-2412 and (c) SG-6043 hydrofoil; (b) and (d) refers to the grid near the hydrofoil for NACA-2412 and SG-6043 hydrofoil

Since the design of the HAHkTs is based on effective water velocities of 1.75-2.25 m/s as observed in most of the rivers [13], a mean water speed of U_∞ = 2 m/s was chosen for the current work. The top, bottom and left surfaces have been given velocity inlet boundary conditions with turbulence intensity (I) of 3% and length scale (l) of 0.02m derived from the empirical relationship based on the given flow condition: $I = 0.16(\mathrm{Re})^{-1/8}$ and $l = 0.07L$, where L is computed from the physical dimension of the object, i.e. chord length for the present case. A pressure outlet boundary condition is provided on the right surface with zero gauge pressure and turbulent viscosity ratio is set at a value of 10. The pressure outlet boundary condition sets a specific static pressure at outlet and radial equilibrium distribution is added for rotating domain simulations as a result of which the pressure gradient is expressed as a function of the distance from the axis of rotation r and the tangential velocity component (u_θ).

$$\frac{\partial p}{\partial r} = \frac{\rho u_\theta^2}{r} \tag{3.17}$$

An untwisted, constant pitch turbine of radius R = 1m was chosen for the three-dimensional rotating condition. The computational domain consists of two cylinders; the inner one and outer one extending 10 rotor diameters and 11 rotor diameters respectively in the axial direction (see Figure 3.3a). The turbine blade has SG-6043 hydrofoil section and is placed inside the inner cylinder as shown in Figure 3.3b. Multiple reference frames have been adapted with a stationary outer cylinder and rotating inner cylinder and an interior boundary between the two. Since the boundary between the two zones is conformal i.e. mesh node locations are identical at the meeting boundary, the interior boundary condition enables particles to pass through the inner boundary to outer one. Velocity inlet and pressure outlet boundary conditions are applied with turbulence specifications same as that for the two-dimensional simulations. A symmetry boundary condition has been provided on the periphery of the outer cylinder indicating zero normal gradients for all flow variables at the symmetry plane. The final domain contains approximately 2.7 million unstructured tetrahedral/hybrid cells with $50 \leq y^+ \leq 350$. Second order upwinding discretization schemes have been employed for all the variables and SIMPLE (Semi-implicit method for pressure linked equation) algorithm was selected for solving pressure-velocity coupling [73]. The PRESTO (pressure staggering options)

scheme has been adopted due to its superiority for flows with steep pressure gradient such as the present case [74]. Convergence criteria have been set such that the residuals for the continuity, *x*-momentum, *y*-momentum, *z*-momentum, *k* and ω are less than 10^{-4}. Details of the simulation parameters are provided in Table 3.1.

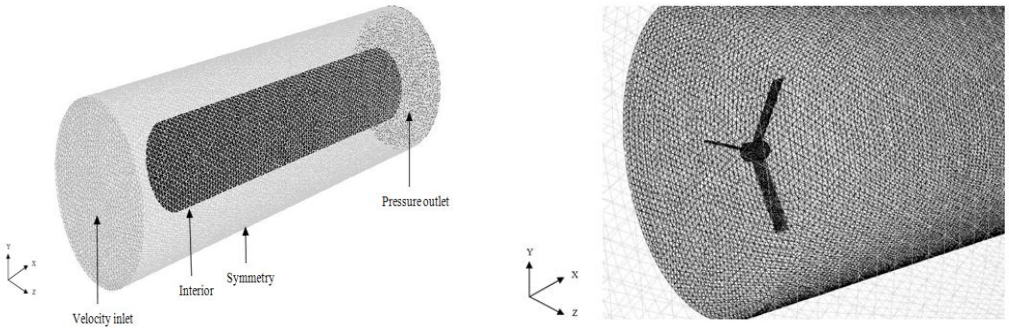

(a) (b)

Figure 3.3. (a) Three-dimensional domain of HAHkT along with boundary conditions (b) grid near the rotor hub

3.3.4. Grid convergence. While developing the finite-difference approximation of the governing equations, the truncation error of the discrete system determines the deviation between the exact and numerical solution. As number of grid points is increased and grid spacing is reduced, the error in the numerical solution decreases and the proper agreement between the numerical and exact solutions is established. When the numerical solutions obtained on different grids agree to within a level of tolerance specified by the user, they are referred to as *grid converged* solutions. The concept of grid convergence applies to the finite-volume approach as well, where the numerical solution, if correct, becomes independent of the grid as the cell size is reduced. For the present case, the grid independence study was performed by calculating the torque generated at the center of the rotor hub using eight different grid sizes with total number of cells (N_{total}) varying between 3.9×10^5 and 4.6×10^6 (see Figure 3.4).

Table 3.1. Parameters for CFD analysis using FLUENT

Hydrofoil	NACA-2412, SG-6043
Density (ρ)	998.2 kg/m^3
Pressure (p)	101.3 kPa
Rotor radius (R)	1 m
Chord length (c)	0.2 m
Number of blades (N)	2-4
Blade pitch (θ_P)	10°
Rotor speed (Ω)	3-8 rad/s
Fluid speed (U_∞)	2 m/s
Turbulence model	k-ω SST
Interpolating scheme	2nd order upwind
Pressure scheme	PRESTO
Residual error	1×10^{-4}

The fractional change in the magnitude of the torque was calculated based on the formulation:

$$\%\ Error = \frac{|T - T_0|}{T_0} \times 100 \tag{3.18}$$

where T denotes torque at different grid sizes and T_0 denotes torque correponding to grid independent (maximum grid size) geometry. A grid independent solution with a nearly constant magnitude of torque was observed beyond $N_{total} = 2.7\times10^6$ where the difference was $< 1\%$; hence suggesting adequate grid resolution for the present study. Based on such grid resolution, the computation time for each simulation varied between 6-8 CPU hours when four to six processors were used using Fluent parallel interface on a machine having 2.4 GHz processor speed and 24 GB of RAM.

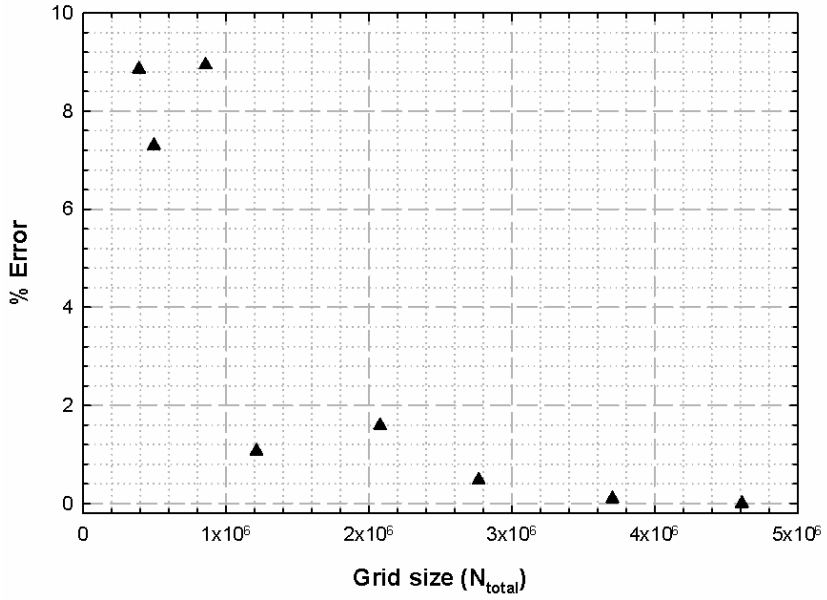

Figure 3.4. Grid independence study for the numerical model

3.4. MODELING FLOW CAVITATION

Cavitation plays a major role in any hydraulic turbines and can lead to fatal failure of the hydraulic structures if not avoided or at least controlled. Due to the rapid development and broader application of powerful computers and the ability to save costs and time in comparison with experiments, numerical techniques have become increasingly popular in recent years. Amongst different cavitation models that exist in literature the Schnerr and Sauer cavitation model [57, 75-76] is used in the present work. The assumptions for a standard two-phase cavitation models are:

(a) The system under investigation must consist of a liquid and a vapor phase

(b) A mass transfer takes place between the liquid and gas phase. Both bubble formation (evaporation) and collapse (condensation) are taken into account in the cavitation models

(c) The cavitation models are based on the Rayleigh-Plesset equation, describing the growth of a single vapor bubble in a liquid

(d) The input material properties used in the cavitation models can be constants, functions of temperature or user-defined.

With the multiphase cavitation modeling approach, a basic two-phase cavitation model consists of using the standard viscous flow equations governing the transport of mixture (Mixture model) or phases (Eulerian multiphase) and a conventional turbulence model (k-ε model). In cavitation, the liquid-vapor mass transfer (evaporation and condensation) is governed by the vapor-transport equation:

$$\frac{\partial}{\partial t}(\alpha\rho_{\mathrm{v}}) + \nabla\cdot(\alpha\rho_{\mathrm{v}}\vec{V}_{\mathrm{v}}) = R_e - R_c \tag{3.19}$$

where, v is the vapor phase, α is the vapor volume fraction, ρ_{v} is the vapor density, $\vec{V}_{\mathrm{v}}$ is the vapor phase velocity, R_e and R_c are the mass transfer source terms connected to the growth and collapse of the vapor bubbles respectively. The terms R_e and R_c are modeled based on the Rayleigh-Plesset equation describing the growth of a single vapor bubble in a liquid. In a flowing liquid with zero velocity slip between the fluid and bubbles, the bubble dynamics equation can be derived from the generalized Rayleigh-Plesset equation as:

$$R_B\frac{D^2R_B}{Dt^2} + \frac{3}{2}\left(\frac{DR_B}{Dt}\right)^2 = \left(\frac{P_B - P}{\rho_l}\right) - \frac{4\nu_l}{R_B}R_B - \frac{2S}{\rho_l R_B} \tag{3.20}$$

where, R_B is the bubble radius, ρ_l is the liquid density, P_B is the bubble surface pressure and P is the local far-field pressure. According to the Schnerr and Sauer cavitation model, the vapor volume fraction has the general form:

$$\frac{\partial}{\partial t}(\alpha\rho_{\mathrm{v}}) + \nabla\cdot(\alpha\rho_{\mathrm{v}}\vec{V}) = \frac{\rho_{\mathrm{v}}\rho_l}{\rho}\frac{D\alpha}{Dt} \tag{3.21}$$

The relationship that connects the vapor volume fraction to the number of bubbles per unit volume of liquid can be expressed as:

$$\alpha = \frac{n_b \frac{4}{3}\pi R_B^3}{1 + n_b \frac{4}{3}\pi R_B^3} \tag{3.22}$$

The mass transfer rate (R) and bubble radius (R_B) can be similarly expressed as:

$$R = \frac{\rho_v \rho_l}{\rho} \alpha(1-\alpha) \frac{3}{R_B} \sqrt{\frac{2(P_v - P)}{3\rho_l}} \tag{3.23}$$

$$R_B = \left(\frac{\alpha}{1-\alpha} \frac{3}{4\pi} \frac{1}{n} \right)^{1/3} \tag{3.24}$$

The numerical models discussed in section 3.3 and section 3.4 was employed to perform the simulations of HAHkT under different flow conditions and turbine geometries.

4. RESULTS

4.1. VALIDATION OF THE THREE-DIMENSIONAL NUMERICAL MODEL

The performance of a hydrokinetic turbine can be characterized by the power coefficient (C_P) and thrust (T) of the turbine. The power coefficient determines the amount of energy captured by the rotor while the rotor thrust influences the structural design of the rotor. A detailed list of the numerical simulations and their individual objectives is given in Table 4.1. Before establishing the influence of the non-dimensional variables (defined in the chapter 3) on the turbine performance, the numerical model was first validated with existing theoretical and experimental results. We systematically validate our results by cross-comparing both the two-and three-dimensional numerical simulation results against BEM theory while using water as working fluid. Our three-dimensional simulations are validated with wind tunnel experimental data of Duquette *et al*. [77].

4.1.1. Validation with BEM theory. In order to validate the three-dimensional numerical model, the overall performance of HAHkT was computed and cross-compared with results from BEM theory under the range of TSR (1.5-4.5) and angle of attack (0°-14°). The results are plotted in Figure 4.1, a maximum C_P of 0.15 was obtained from the three-dimensional numerical model at TSR = 3.5. In comparison a maximum C_P value of 0.16 was obtained from BEM theory at TSR = 3. At low values of TSR = 1.5, flow incidence becomes high which results in increased angle of attack for a fixed pitch turbine blade as in the present case. The maximum power at low TSR is therefore limited by blade stalling (for details refer to §2.2.7), whereas the limiting factor for high TSR is guided by lower lift due to the lower angle of attack. The peak C_P was observed to lie between these two extreme limits yielding a bell shaped curve for both cases. However, a significant deviation in C_P was observed at TSR = 1.5 and can be attributed to stall due to higher flow incidence, where blade lift reaches its peak value and further increase in angle of attack results in decrease in lift.

Table 4.1. List of simulations performed for hydrodynamic modeling of HAHkT

Type	# of Simlns	Variables	Constants	Objectives
2D	33 (11×3)	Angle of attack, turbulence models	Inlet velocity and zero outlet gauge pressure	Lift and drag characteristics with NACA-2412 hydrofoil using three distinct turbulence models
	33 (11×3)	Change of hydrofoil, angle of attack, turbulence models	Inlet velocity and zero outlet gauge pressure	Lift and drag characteristics for SG-6043 hydrofoil and comparison with NACA-2412 using same turbulence models
	8 (4×2)	Flow velocity and Static pressure	Angle of attack, Realizable k-ε model	Effect of cavitation number on cavitation onset
	4	Angle of attack	Cavitation number, Realizable k-ε model	Effect of angle of attack on cavitation onset
3D	8	Cell size	Inlet velocity and outlet static pressure, k-ω SST turbulence model	Grid independence study to obtain sufficiently fine geometry for accurate flow predictions and performance analysis
	7	TSR and Angle of attack	Rotor geometry, inlet velocity, outlet zero gauge pressure	Validation of numerical model with BEM theory for a given range of TSR
	7	TSR and Angle of Attack	Rotor geometry, inlet velocity, outlet zero gauge pressure	Validation of numerical model with experiments and BEM theory (air as working fluid)
	7	TSR, solidity (R/c) and angle of attack	inlet velocity, outlet zero gauge pressure	Effect of solidity (R/c ratio) on turbine performance
	21 (7×3)	TSR, angle of attack and # of Blades	R/c ratio, inlet velocity and outlet zero gauge pressure	Effect of blade numbers and solidity on turbine performance

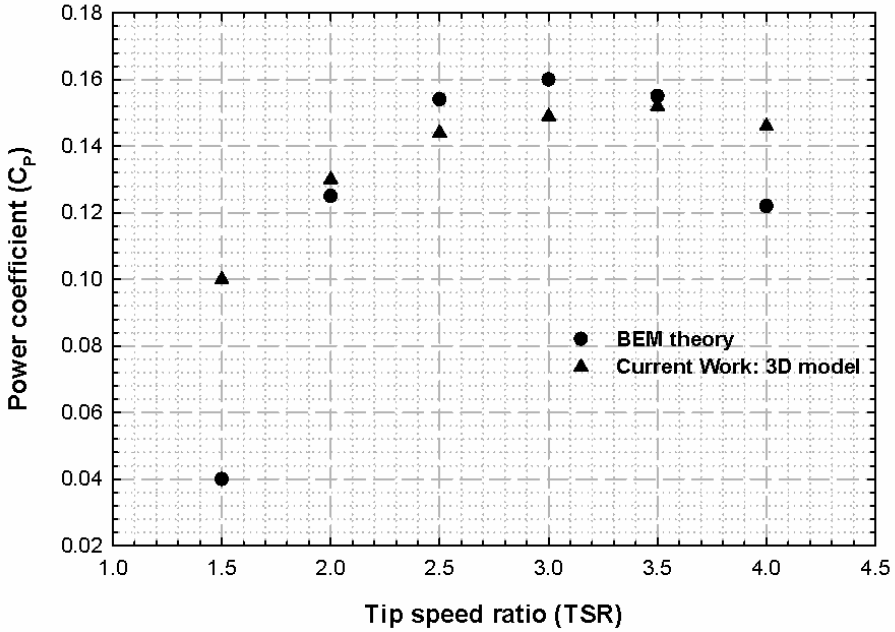

Figure 4.1. Comparison of the power coefficient using both BEM theory and three-dimensional Fluent simulations

The results obtained from BEM theory conventionally offer good agreement with numerical simulations and experimental measurements under attached flow condition on the surface of the blades [52]. However, under the effect of three-dimensional rotation of turbine rotor, the centrifugal acceleration causes radial flow in the boundary layer and Coriolis force accelerates the flow in the chord-wise direction. The combined effect of both these forces causes a delay in stall with simultaneous increase in lift value compared to two-dimensional BEM theory where the flow along span-wise and chord-wise direction are neglected.

Figure 4.2 illustrates validation of thrust coefficient (C_T) obtained by three-dimensional numerical simulations with BEM theory. Both results show similar increasing trend with C_T obtained from BEM theory leveling off at TSR > 3.5. In BEM theory C_T is calculated from equating thrust forces to the product of cross-sectional area and the pressure difference between the two sides of actuator disc. The forces on the turbine blades are determined only by the lift and drag characteristics of the hydrofoil. Therefore the value of the axial induction factor (a) governs the nature of C_T and causes it to level off beyond a particular point. However, this discrepancy can be attributed to the fact that the three-dimensional numerical results incorporate both axial and angular

induction factors due to rotational motion of the turbine. Since the rotation adds further pressure drop across the turbine rotor plane and further reduces the kinetic energy of the flow, the thrust is overestimated in BEM theory which only considers axial induction factor.

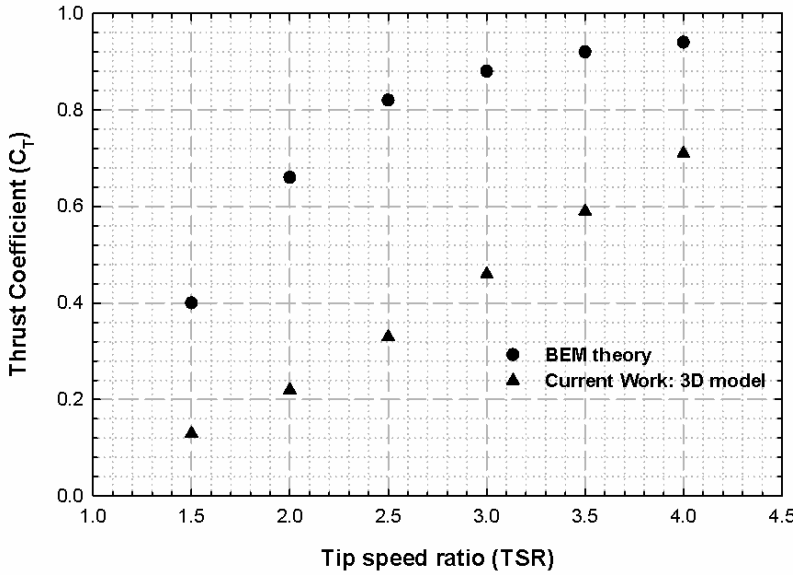

Figure 4.2. Comparison of thrust coefficient using both BEM theory and three-dimensional Fluent simulations

4.1.2. Validation with experiments. Our three-dimensional numerical model was further validated with experimental data; the overall performance of the HAHkT was computed and compared to wind-tunnel experiments performed by Duquette *et al*. [70]. The comparison is plotted in Figure 4.3. It was observed that BEM theory over-predicts the C_P value by an average value of 20% for most of the operating range of TSR ranging between 1 and 3. This over-prediction can be attributed to the uniform inflow assumption over each rotor disc annulus where the blade elements are placed at equally spaced radial locations. This results in poor resolution of turbine loading in the tip region where the loading rapidly drops to zero from a finite value. The abrupt variation of air forces at the tip region leads to an over-prediction of peak power and associated C_P [54]. As seen in Figure 4.3, the numerical results agreed quite consistently with both experimental and theoretical data fits over the entire operating range of TSR.

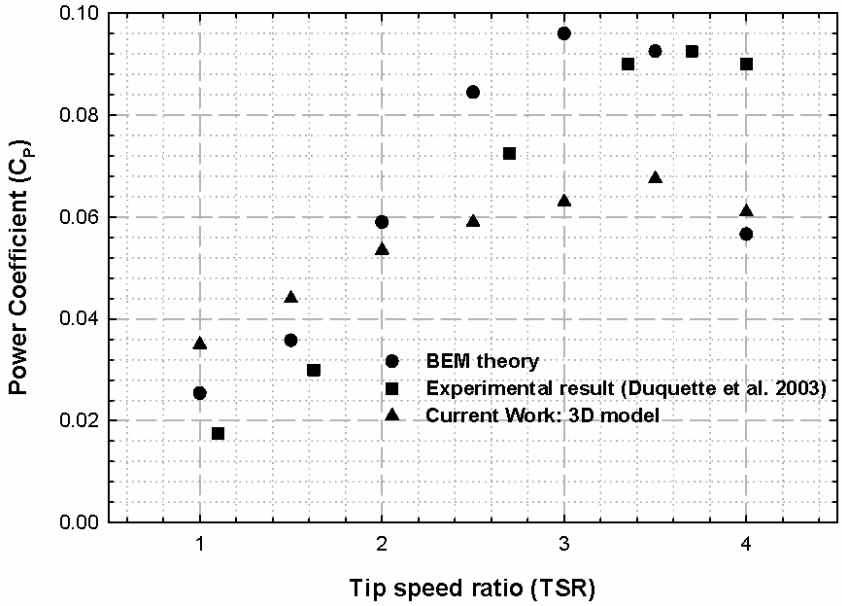

Figure 4.3. Comparison of 3D numerical model with BEM theory and experimental investigation as reported in [75]

4.2. PERFORMANCE EVALUATION OF HAHkT

4.2.1. Two-dimensional calculation for performance evaluation. The HAHkT performance is often associated with optimum lift and drag characteristics of the turbine blades depending on flow speed and α. For a fixed flow speed, both C_L and C_L/C_D ratio needs to be calculated across a range of α to determine the optimum operating point. Accordingly two-dimensional numerical simulations were performed using two different hydrofoil shapes: SG-6043 and NACA-2412, the primary difference between the two being the change in camber on the hydrofoil surface (see Figure 4.4 and Figure 4.5). Since the Reynolds number (*Re*) for the flow ~ 4×10^5 when considering an average flow stream velocity (~2 m/s), flow turbulence becomes important and needs to be accounted for. We utilize three distinct turbulence models:

(a) Spalart-Allmaras (SA) model [64]

(b) Realizable k-ε model [67] and

(c) k-ω SST model [62].

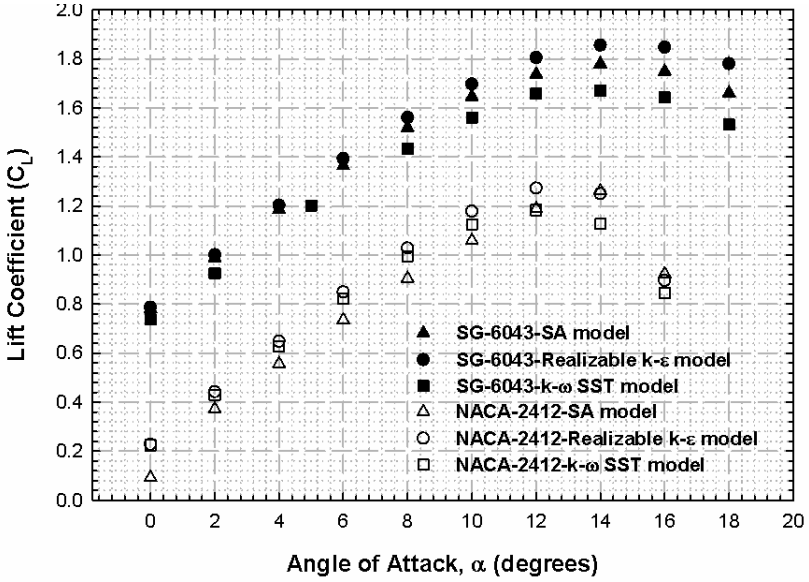

Figure 4.4. Comparison of lift coefficient obtained from both SG-6043 and NACA-2412 hydrofoil using SA, Realizable *k-ε* and *k-ω* SST models

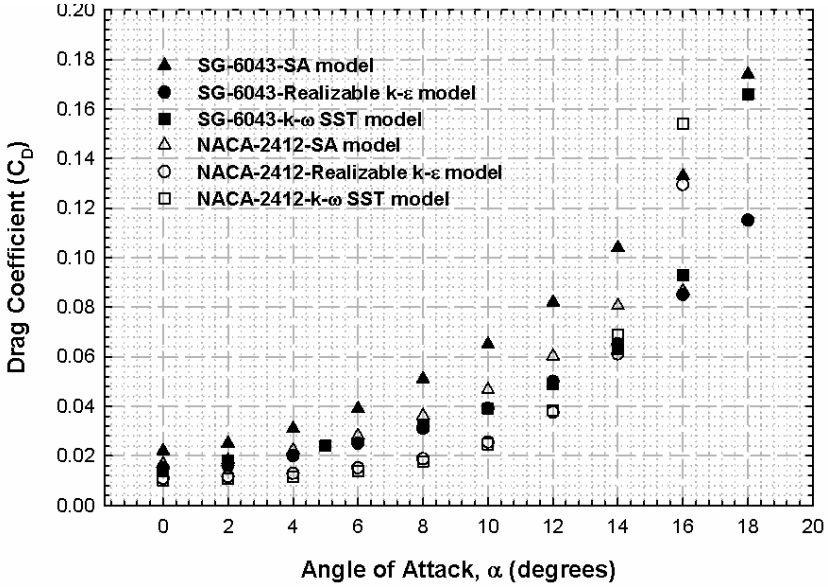

Figure 4.5. Comparison of drag coefficient obtained from both SG-6043 and NACA-2412 hydrofoil using all three turbulence models

The three turbulence models were chosen based on accurate prediction of flows having an adverse pressure gradient and boundary layer separation [59, 62, 65, 78]. It can be observed from that SG-6043 hydrofoil produced greater C_L and C_D (see Figure 4.4 and 4.5) when compared with NACA-2412. We conjecture that the former hydrofoil has higher (6%) camber compared to the latter hydrofoil (2% camber) which results in greater pressure reaction at the hydrofoil surface and subsequently generate higher C_L and C_D. At low to moderate angles of attack, C_L varies linearly with α where the flow moves smoothly over the hydrofoil and is attached to most of the surface. However, as α becomes large, the flow tends to separate from the top surface of the hydrofoil creating a large wake behind the hydrofoil. This can be better visualized from the pressure coefficient and velocity contours for $\alpha = 5^{\circ}$ and $\alpha = 14^{\circ}$ as shown in Figure 4.6. When a fluid flows over a solid surface, the influence of friction between the surface and the fluid adjacent to the surface creates a frictional force known as shear force which retards the relative motion. There is a favorable pressure gradient up to a minimum pressure point falling in the direction of flow. This helps to stabilize the boundary layer. Downstream of the minimum pressure point, however, the thickening boundary layer has to flow against an adverse pressure gradient. Here viscous effects reduce momentum within the boundary layer, and the thickness of the layer further increases so that the external flow sees a body which does not appear to close to a point at the trailing edge. A wake is formed as the boundary layer streams off the section. As α is increased, the point of minimum pressure moves towards the leading edge, with increasingly high suction being achieved. This means that the pressure then has to rise by a greater extent downstream of the minimum pressure point and that the length of hydrofoil surface exposed to the rising pressure is increased. The resulting adverse pressure gradient becomes more severe as angle of attack is further increased. This has serious implications for the boundary layer, which is always likely to separate from the surface under such conditions. Figure 4.7 also shows an increased C_L/C_D ratio for SG-6043 when compared with NACA-2412 counterpart due to the increased camber effect.

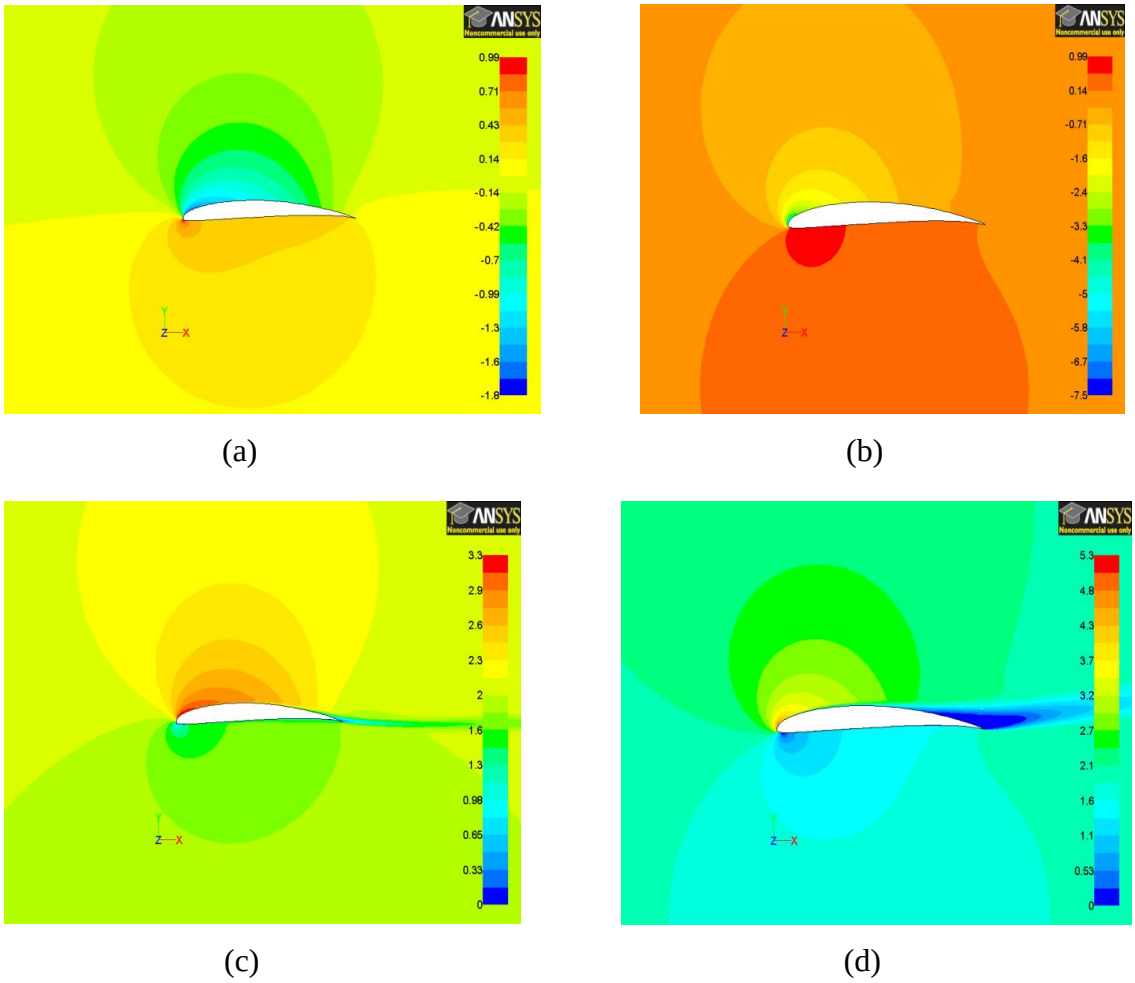

Figure 4.6. Contour of pressure coefficient for (a) α = 5° (attached flow) and (b) α = 14° (separated flow). Contour of velocity magnitude (expressed in m/s) for the same (c) attached and (d) separated flow conditions

The profiles of C_L as a function of α obtained from the various turbulence models are also compared with BEM results reported by Duquette *et al*. [71]. As shown in Figure 4.8, under the attached flow condition in which the turbine flow incidences lie below the static stall angle (α_{stall}), C_L increases almost linearly with α for all turbulence models with $(C_L)_{max}$ observed at $\alpha_{stall} \sim 14^{\circ}$. As α is increased beyond α_{stall}, flow separation tends to set in early from the trailing edge of the hydrofoil with the generation of large wakes resulting in decreased lift and increased pressure drag. It has been observed that C_L for the attached flow condition is over-predicted by ~ 6-10% using SA and Realizable k-ε model whereas a very close agreement can be observed for k-ω SST model with less than 4% deviation from BEM theory.

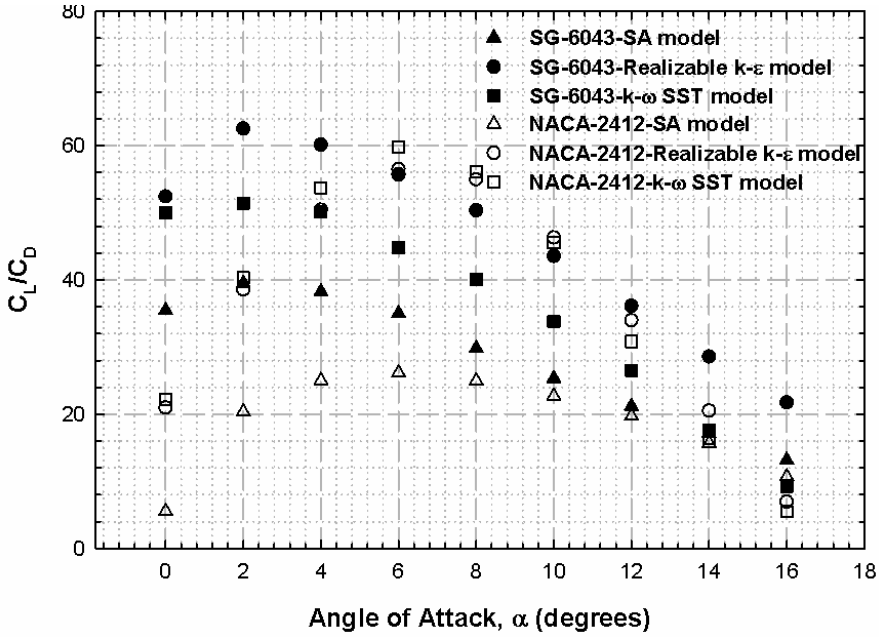

Figure 4.7. Comparison of lift to drag ratio obtained from both SG-6043 and NACA-2412 hydrofoil for different angles of attack

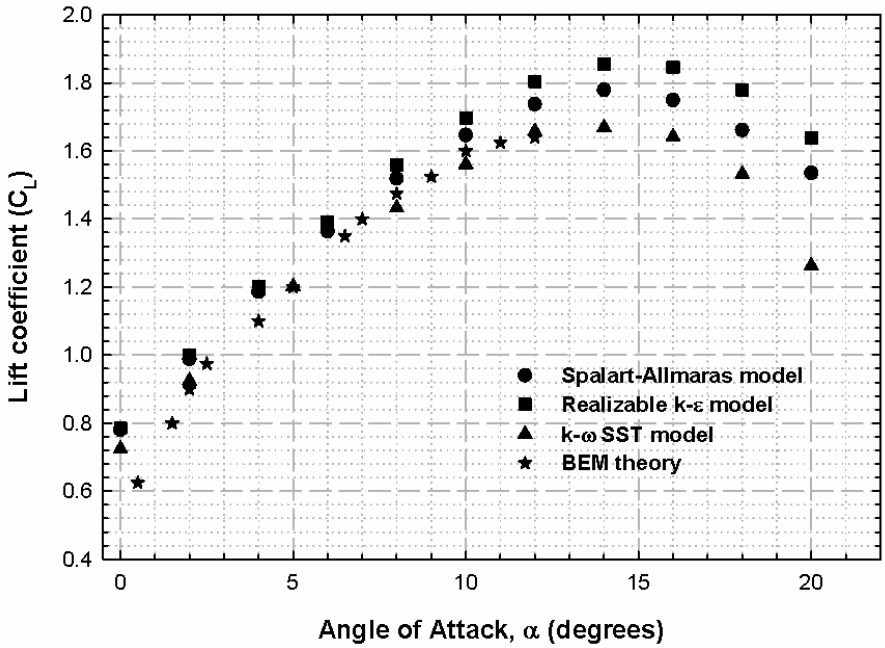

Figure 4.8. Lift coefficient distribution for SG-6043 hydrofoil using BEM theory and SA, Realizable k-ε and k-ω SST turbulence models

SA model is primarily a low *Re* model which solves a single model transport equation for kinematic eddy viscosity (ν_t). As result, the SA model performs better flow predictions for the flows where viscosity-affected region of the boundary layer needs to be properly resolved such as the present case [79]. The RKE model proposed by Shih *et al*. [78] also provides superior performance compared to the standard k-ε model [68] for the present flow condition due to its new model formulation based on the dynamic equation of mean-squared vorticity fluctuation. Details of the formulation can be found elsewhere [78]. As discussed in section 3.3.2, the k-ω SST yielded the most accurate C_L values when compared to BEM theory due to its improved formulation for predicting the adverse pressure gradient in hydrofoil flows. Figure 4.9 shows the lift to drag coefficient ratio (C_L/C_D) distribution using BEM theory and the three turbulence models; the objective was to determine an optimum angle of attack (α_{opt}) for SG-6043 hydrofoil. While BEM theory predicts $\alpha_{opt} = 4^\circ$, all three turbulence models predicted a smaller $\alpha_{opt} = 2^\circ$ corresponding to maximum C_L/C_D ratio. It is interesting to note that the magnitude of $(C_L/C_D)_{max}$ corresponding to a 4° angle of attack using BEM theory matches quite closely with that of RKE model with < 5% deviation even though k-ω SST offers best prediction of C_L/C_D over the entire operating range of angle of attack.

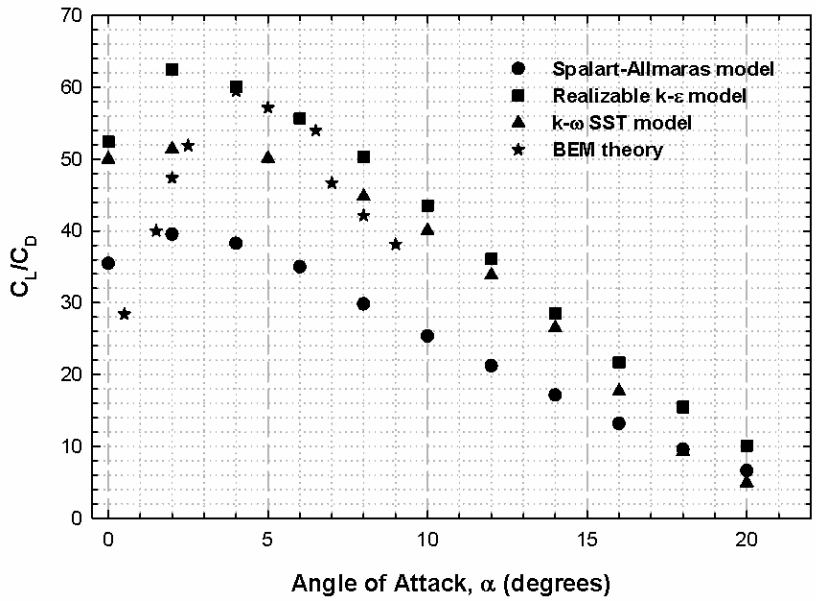

Figure 4.9. Variation of lift to drag ratio with different angle of attack using BEM theory and SA, Realizable k-ε and k-ω SST turbulence models

4.2.2. Three-dimensional calculation for performance evaluation. An optimum design of HAHkT is associated with turbine solidity (σ) and TSR since these two variables primarily control the volume of fluid which can be utilized for power extraction. The power output of a turbine is proportional to the thrust that the turbine exerts on the flow. However, the increase in thrust is also associated with a simultaneous increase in flow impedance resulting in lower energy flux and flow velocity. In order to establish a proper balance between σ and TSR, an intermediate σ at a given flow condition is sought. A turbine of zero solidity provides no lift while its infinite solidity counterpart would prevent fluid to flow through rotor plane resulting in zero mechanical work. Thus, in order to examine the influence of solidity on turbine performance, three-dimensional numerical simulations were performed using a three-bladed turbine with radius to chord ratios (R/c) of 4, 5 and 6 respectively. The results are plotted in Figure 4.10. As solidity is increased by ~ 25%, corresponding to decrease of R/c from 5 to 4, maximum rotor power becomes higher by ~ 30% and location of TSR corresponding to maximum C_P changes from 3.5 to 3. Observing the trend for all three R/c ratios, it can be inferred that a rotor having larger solidity generates maximum power at a lower TSR. A lower TSR results in increase of angle of angle of attack and therefore, increased lift and torque for a higher solidity turbine. Increased flow impedance along with a corresponding increase of solidity forces the turbine rotor to produce maximum power at a reduced TSR thereby shifting the maximum C_P towards left. The effect of the number of blades (N) on the performance of a HAHkT is also investigated using two, three and four bladed turbines. As shown in Figure 4.11, for a constant σ = 0.095, turbines with two and three blades achieved larger C_P than with four blades. This effect is caused by increased blockage due to increased number of turbine blades rotating at a constant RPM. As a result, less flow can pass through the turbine decreasing flow entrance velocity at the rotor plane and ultimately resulting in less power extraction. All three turbines however produce maximum C_P at a constant TSR = 3.5 since the solidity is held constant. If instead the effect of number of blades being investigated under constant R/c it can be observed that increased number of blades results in better power coefficient with a maximum C_P of 0.23 occurring at a value of TSR = 2.5.

As turbine solidity is approximately doubled from 0.064 to 0.127, the resulting C_P has also doubled from 0.112 to 0.224 implying strong influence of solidity on turbine performance (see Figure 4.12). The results also indicate that the initial starting torque of a four bladed turbine is higher than that of the other two cases. This is expected since more blades will contribute more lift resulting in increased torque at the rotor hub. Since increase in number of blades also corresponds to increase in turbine solidity, the power curve is shifted towards a lower TSR, a feature also observed in Figure 4.9. Furthermore, the results obtained from Figures 4.9-4.12 provide useful insight for choosing turbine solidity for user-specific applications. Higher solidity turbines will be used when higher initial starting torque and lower rotational speed is required such as water pumping [80]. On the contrary, lower solidity turbines should be considered where lower torque and higher rotational speeds are necessary such as the production of electricity.

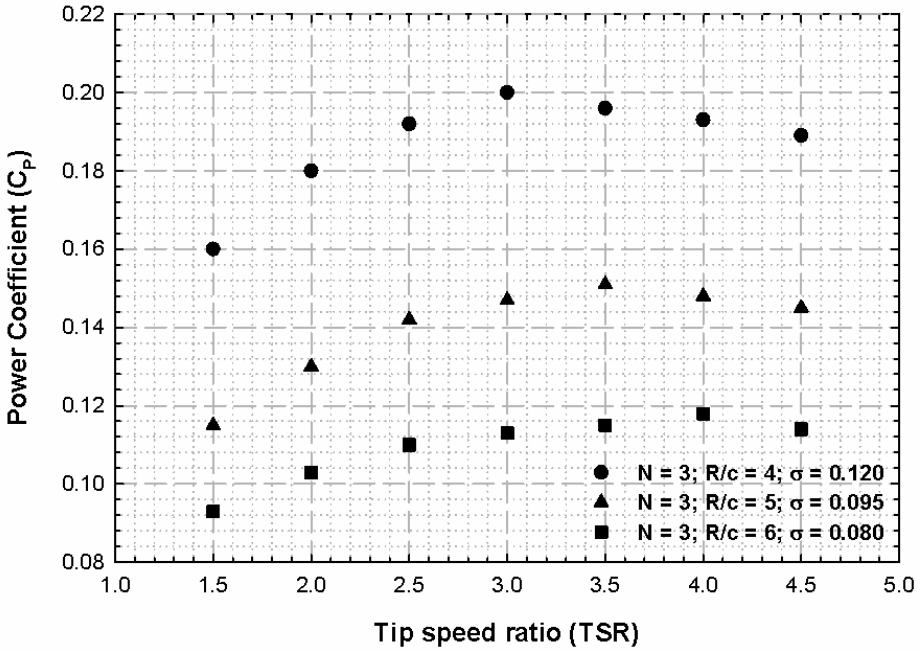

Figure 4.10. Comparison of power coefficient versus tip speed ratio under different turbine solidities for $N = 3$

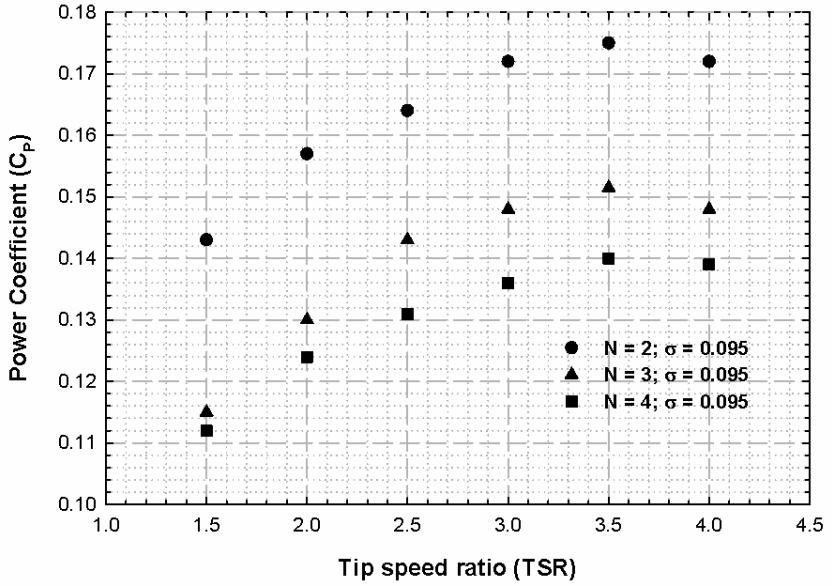

Figure 4.11. Comparison of power coefficient versus tip speed ratio under different turbine blade numbers when σ is kept constant

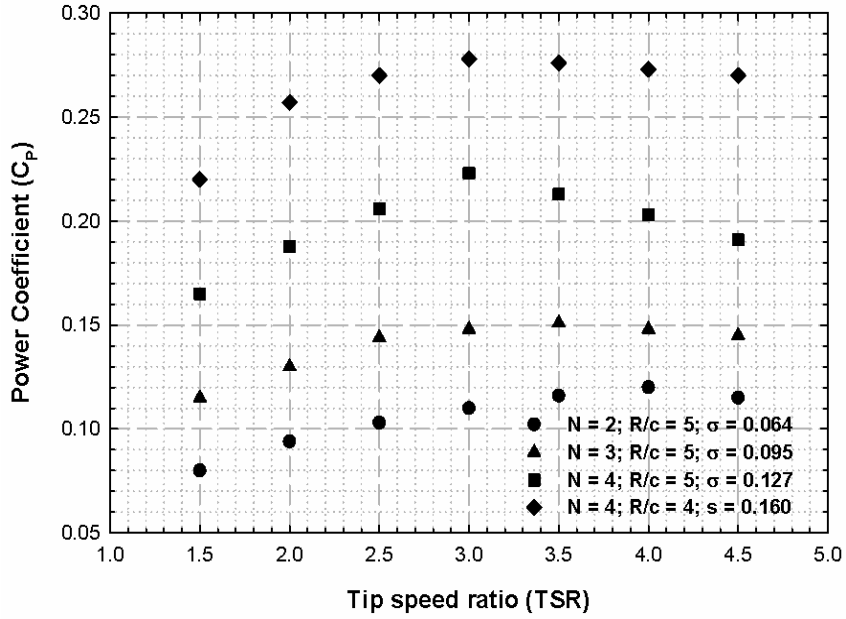

Figure 4.12. Effect of blade numbers on the performance of HAHkT using 2, 3 and 4 blades when R/c = 5 is held constant

4.3. WAKE STUDY

4.3.1. Rotational effect and stall delay. The axial velocity distribution normalized by free-stream flow speed (U_∞) along the non-dimensional radial location (r/R) is compared for stationary two-dimensional and rotating three-dimensional flow in Figure 4.13. A large axial velocity deficit ($U_x/U_\infty < 1$) was observed in the wake region behind the trailing edge for two-dimensional hydrofoil and a similar phenomenon has also been observed behind the rotor hub for the three-dimensional geometry. However, the magnitude of axial velocity deficit as plotted in Figure 4.13 and obtained from two-dimensional simulation is much higher compared to the three-dimensional case. Both the two-dimensional and three-dimensional runs were performed under identical *Re* (= 4×10^5) and α (= 18°). The mismatch in axial velocity occurs due to the stall-delay phenomenon of HAHkT where the flow separation from the hydrofoil surface is reduced to some extent due to the rotation of the turbine blades resulting in lower U_x/U_∞ in the wake region. As described earlier in §3.1, the stall-delay phenomenon for the three-dimensional rotating condition is effectively a consequence of centrifugal acceleration causing radial flow along the blade span and coriolis acceleration causing the flow in the chord-wise direction. This delays flow separation to a location further downstream. The two-dimensional stationary condition also fails to predict the exact location of peak axial velocity deficit since the suction side of the hydrofoil is subjected to greater velocity deficit than the pressure side. This results in a rightward shift of peak axial velocity distribution for the stationary condition and indicates that the maximum velocity deficit occurs at a positive radial location near to the pressure side of the hydrofoil. The prediction of stall-delay phenomenon for two-dimensional and three-dimensional cases can be further verified by observing their pressure coefficient contours as shown in Figure 4.14. For $\alpha = 18^\circ$, a large pressure drop (negative pressure coefficient) can be observed very near to the leading edge in the two-dimensional case (see Figure 4.14a) indicating the point of flow separation. However, the effect of rapid pressure drop in three-dimensional condition (see Figure 4.14b) is postponed and dispersed across the entire suction surface due to the effect of turbine rotation.

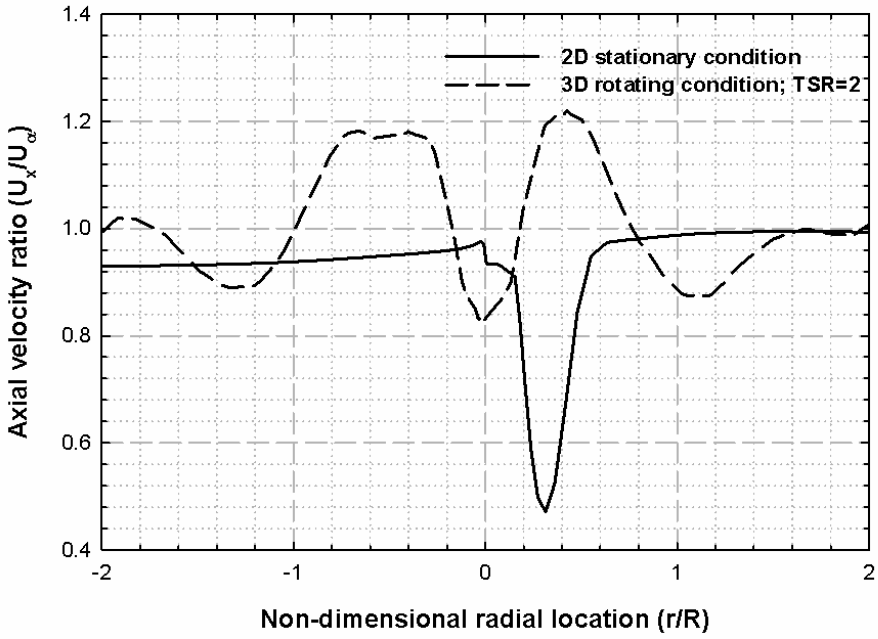

Figure 4.13. Comparison of axial velocity distribution along the radial location for both two-dimensional stationary condition and three-dimensional rotating conditions

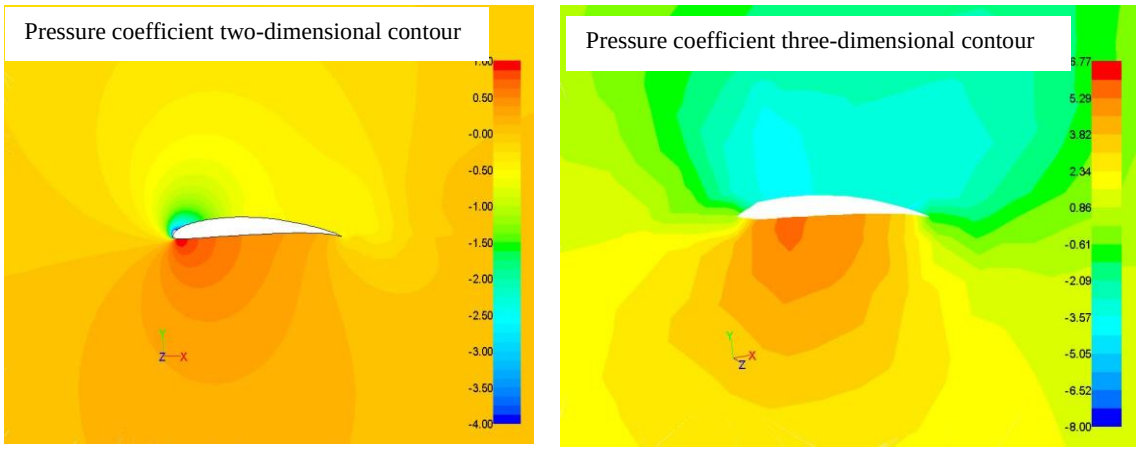

(a) (b)

Figure 4.14. Comparison of pressure coefficient contours for (a) two-dimensional (stationary) and (b) three-dimensional (rotating) condition for $\alpha = 18^{\circ}$

4.3.2. Turbulence parameters and vortex formation. Figures 4.15 (a-c) illustrates the normalized axial, radial and tangential velocity distribution in the non-dimensional radial direction at various downstream axial locations. The axial velocity deficit behind the turbine rotor confirms the expansion and decay of wake phenomenon. The width of the wake increases and axial velocity deficit decreases with increase in downstream distance. In addition, with an increase in radial distance from rotor hub, the axial velocity gradually attains the value of an undisturbed flow resulting in a flattening of the velocity profile beyond one rotor diameter in both directions. At $x/R = 4$, a rapid decrease in axial velocity deficit also implies simultaneous disappearance of wake. The magnitude of radial velocity was observed to be comparatively smaller than the axial velocity for the entire operating range of TSR (see Figure 4.16); a confirmation that axial velocity distribution has greater influence on the power output i.e. efficiency of the turbine. At the rotor downstream, the direction of water flow is opposite to that of the rotor resulting in increased angular momentum in the turbine wake. The flowing water is therefore, subjected to a tangential velocity component along with the axial velocity in stream-wise direction as seen in Figure 4.15c. The axial velocity deficits for two-bladed, three-bladed and four bladed turbines under the operating range of TSR are listed in Table 4.2. A greater axial velocity deficit of ~ 20% has been observed for TSR= 2 compared to ~ 8% as observed for TSR = 3. The maximum axial velocity deficit occurs just behind the turbine hub where maximum amount of energy has been absorbed by the rotor. Since a decrease in TSR is also associated with a greater volume of flow energy being transferred to the wake or recirculation region, the resultant behind the turbine rotor power output becomes less for a value of TSR = 2 compared to TSR = 3 as observed in Figure 4.10. Increase in number of blades also produces increased flow impedance resulting in 60% axial velocity deficit for a four-bladed turbine as compared to 30% for its two-bladed counterpart at a fixed TSR = 2. This again confirms the effect of blade numbers on turbine performance as shown in Figure 4.12.

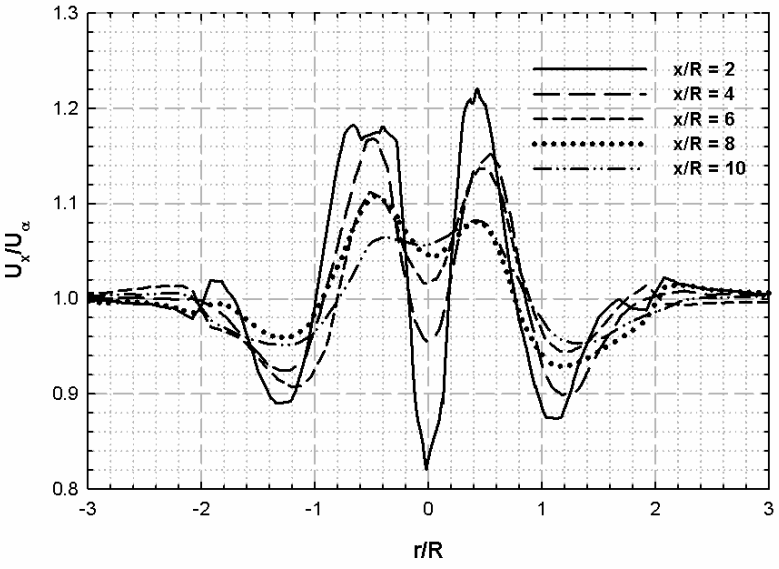

(a)

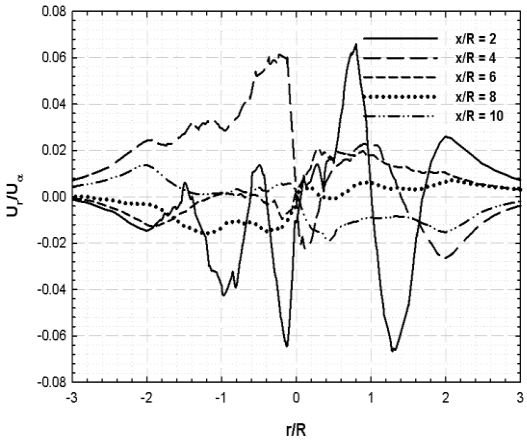

(b)

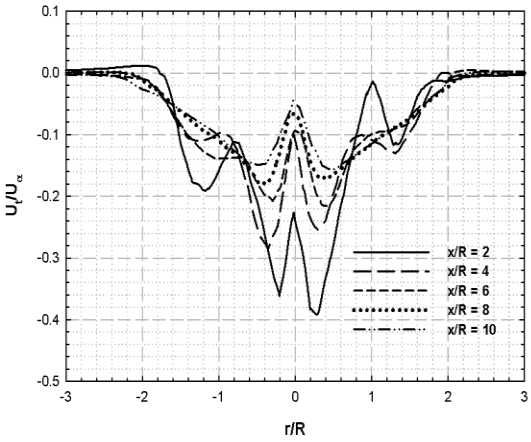

(c)

Figure 4.15. Variation of (a) axial, (b) radial and (c) tangential velocity distribution at different rotor downstream locations calculated at TSR = 2

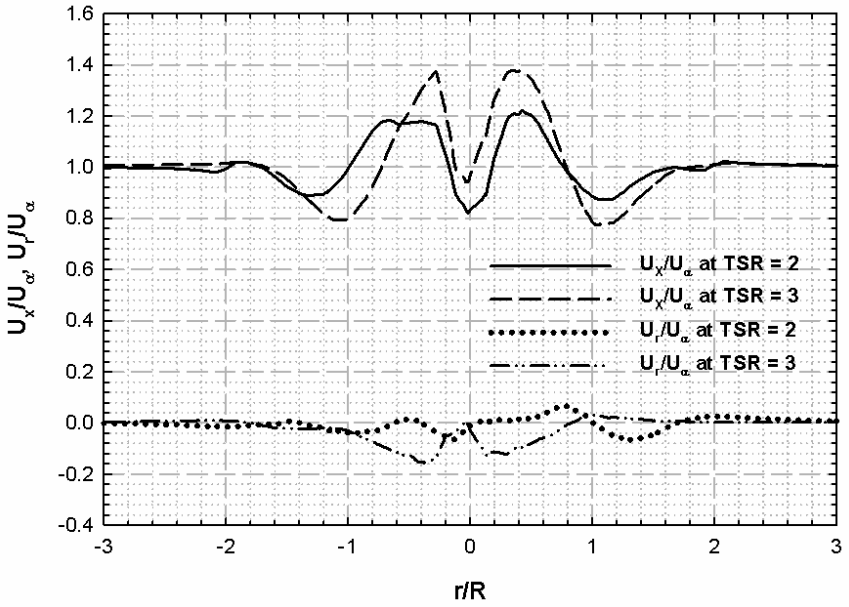

Figure 4.16. Comparison of axial and radial velocity distribution at x/R = 2 for TSR = 2 and 3 respectively

Table 4.2. Axial velocity deficit (U_x/U_∞) for different number of blades

No. of Blades	TSR = 2	TSR = 2.5	TSR = 3	TSR = 3.5
2	0.755	0.925	0.960	0.995
3	0.702	0.728	0.837	0.915
4	0.607	0.629	0.652	0.725

The velocity peaks on both sides of the rotor hub indicate the presence of strong tip vortices on the hydrofoil surface. This can be better visualized in the axial vorticity contour plot in Figure 4.17. A localized region with strong tip vortices can be observed where the axial velocity is higher than U_∞ resulting in negative axial induction factor. Figure 4.18 depicts the downstream development of the wake vortices from the hydrokinetic turbine. The combined effect of the stream-wise water flow and circular motion of turbine blade tips produces a trailing helical vortex at the rotor downstream.

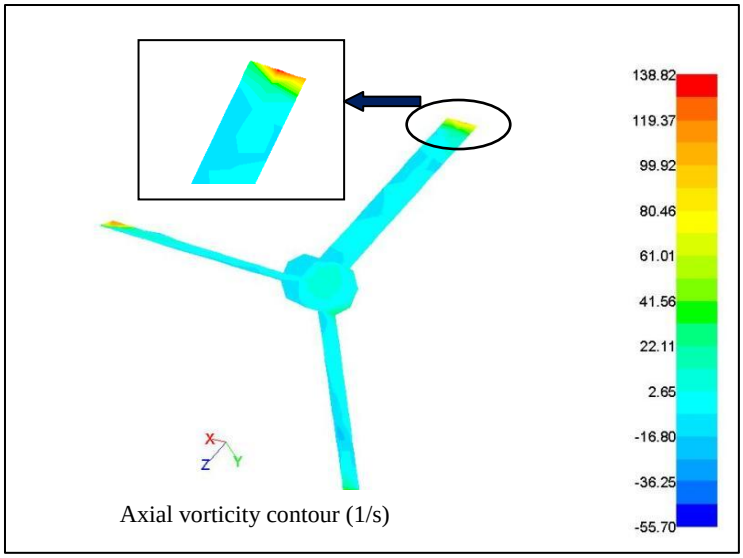

Figure 4.17. Contour of axial vorticity in rotor hub plane at TSR = 2 showing the presence of strong tip vortices

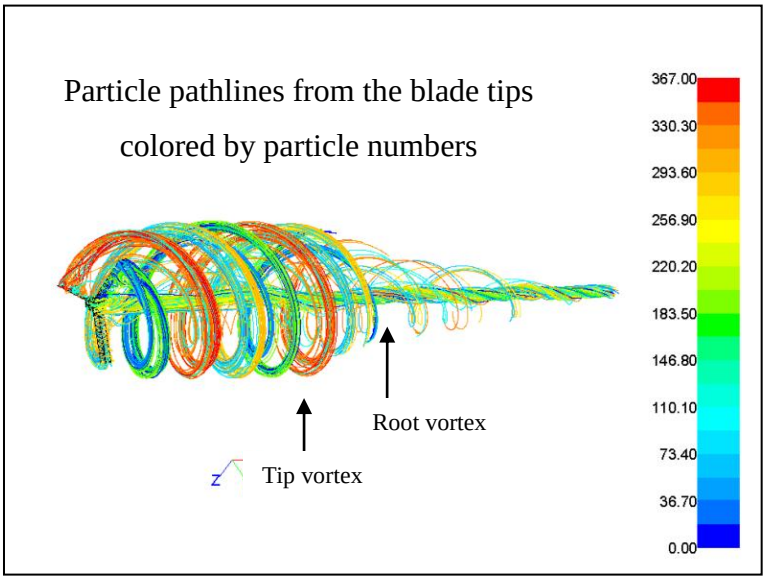

Figure 4.18. Helical vortices being shed from the turbine blade tips

In addition, to the turbine tip vortices, a central vortex is also formed beside the root of the rotor hub. However, since the velocity at the backside of the rotor hub is low, the flow pathlines appear to be straighter as it moves further downstream. The axial vorticity contours can also be used to identify the transition from the near wake to the far wake. In Figure 4.19 the axial vorticity component is plotted on radial cut at different axial locations within the wake. The presence of strong vortices can be observed close to the rotor surface. Under turbine rotation, the rotor decelerates the flow and the flow begins to rotate in the direction opposite to the rotor. In other words, the wake locations shift in the direction opposite to the direction of rotation of the rotor during the downstream development of the wake. The tip vortices can be visualized from the blade surfaces starting at the rotor hub plane until half rotor radius downstream. The shed vortices initially appear as distinct vortex structures which gradually merge into a continuous vortex street at a short distance from the rotor plane. The transition from near wake to far wake can also be observed beyond 1 rotor radius downstream. The tip vortices has a greater influence on axial velocity than the radial or tangential velocity and beyond one rotor diameter downstream the presence of individual blades disappear and velocities are averaged circumferentially.

The pressure coefficient, turbulent kinetic energy and turbulent intensity can be similarly obtained along the radial location for different axial positions downstream of the rotor at 2*R*, 4*R*, 6*R*, 8*R* and 10*R* respectively. A sharp pressure gradient can be observed in Figure 4.20 at 2*R* (near wake) and 4*R* location indicating the formation of wake at the near downstream location. Gradually it recovers some of the pressure head as it moves further downstream location resulting in gradual flattening of the profile. The turbulent kinetic energy profiles in Figure 4.21 and turbulence intensity profiles in Figure 4.22 explain a higher turbulence level in the wake region when compared with non-wake region. A significant increase in turbulent kinetic energy and turbulent intensity is observed in the region of wake centerline and also at the tip of the turbine blades due to the formation of the tip vortices.

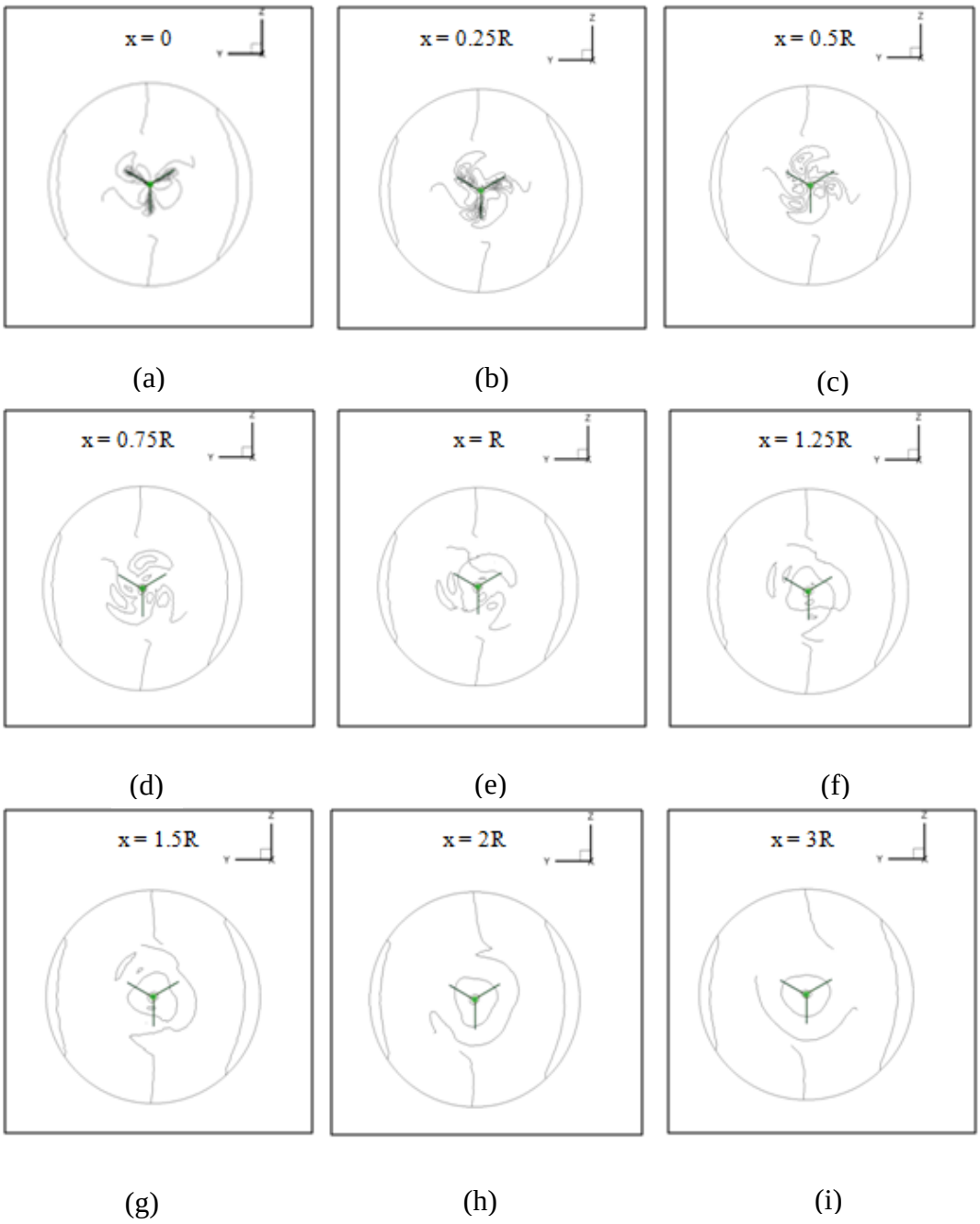

Figure 4.19. Contours of axial vorticity at different axial locations along the rotor downstream for TSR = 2

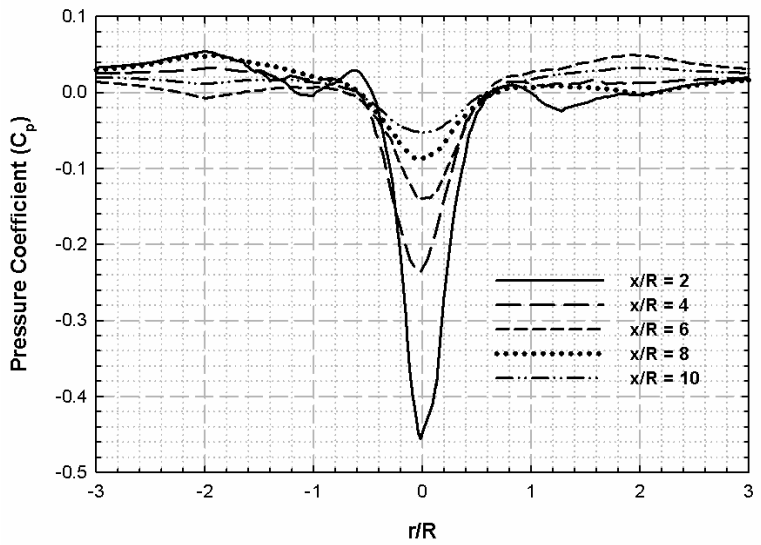

Figure 4.20. Pressure contour along the radial direction at different rotor downstream locations for TSR = 2

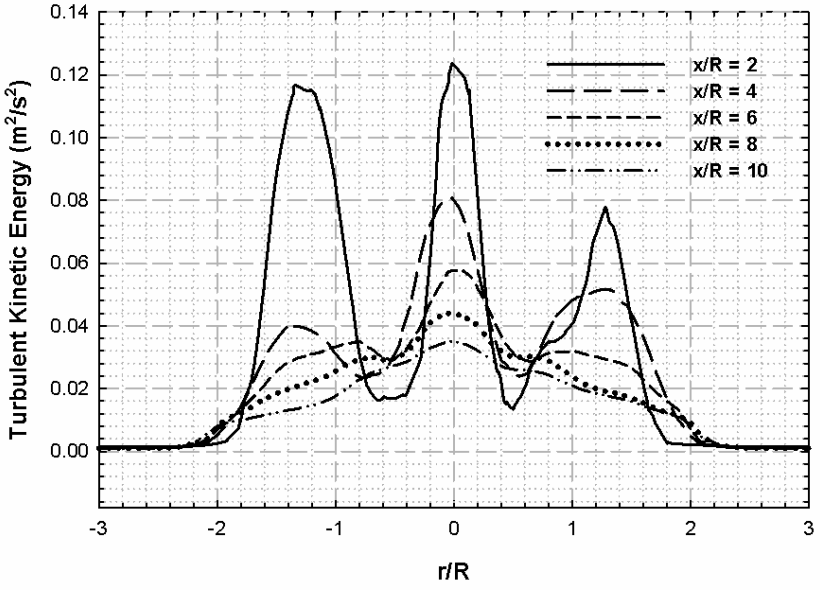

Figure 4.21. Turbulent kinetic energy contour plot along the radial direction at different rotor downstream locations for TSR = 2

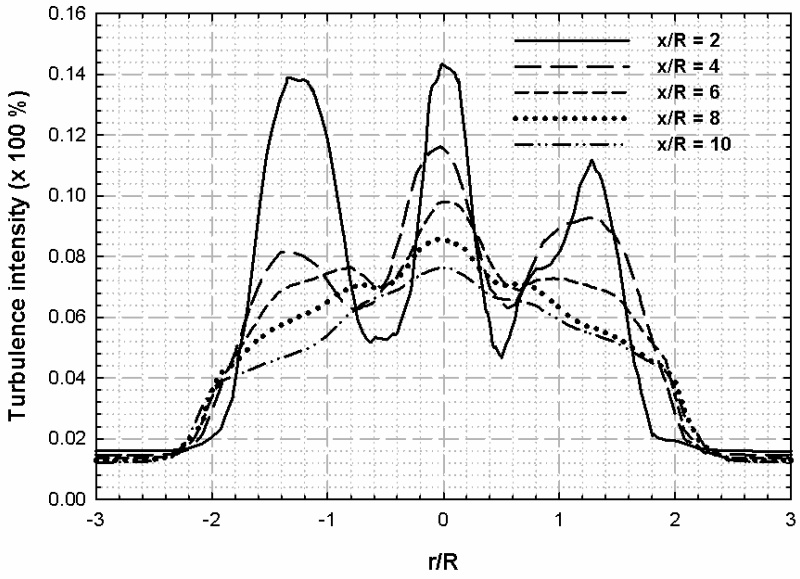

Figure 4.22. Turbulence intensity distribution in the wake region for TSR = 2

The magnitudes of the axial velocity deficit can also be utilized to determine the energy loss from a turbine. Assuming the same mass of fluid upstream and downstream of a turbine, a fractional energy loss ($\Delta E/E_0$) from a turbine can be defined based on thekinetic energy formulation as follows:

$$\frac{\Delta E}{E_0}(\%) = \frac{U_\infty^2 - U_x^2}{U_\infty^2} \times 100 \tag{4.1}$$

Based on Eq. (4.1) the turbine with TSR = 2 incurs ~ 35% energy loss in the wake region behind the turbine. However, under the same circumstances, the turbine with TSR = 3 loses only 15% of its energy which further confirms higher efficiency of the system.

4.4. CAVITATION ONSET

4.4.1. Effect of cavitation number. The cavitation analysis was performed using the SG-6043 hydrofoil section with unit chord length. The objective was to calculate the static pressure on the hydrofoil surface for various cavitation numbers (Σ) and flow angle of attack (α). The Cavitation number and pressure coefficient (C_p) can be calculated as:

$$\Sigma = \frac{P_\infty - P_v}{\frac{1}{2}\rho_l U_\infty^2} \tag{4.2}$$

$$C_p = \frac{P - P_\infty}{\frac{1}{2}\rho_l U_\infty^2} \tag{4.3}$$

where, P_∞ is the static pressure on the hydrofoil surface, P_v is the saturation vapor pressure. As HAHkTs will be placed below the water surface, the static pressure at the hydrofoil surface will be the summation of the ambient static pressure and pressure due to the head of the water above the hydrofoil. Therefore, in order to predict the onset of cavitation, the static pressure on the hydrofoil surface needs to fall below the saturation vapor pressure of the hydrofoil. For the present study, a two-dimensional steady state multi-phase calculation was performed to simulate the presence of vapor in the hydrofoil separation region. A Realizable k-ε model with standard wall function was selected as a turbulence model due to its superior performance prediction for flows involving adverse pressure gradient, separation and recirculation [75, 81]. The working fluid for the present case is water at 300K with liquid density of 1000 kg/m^3, vapor density of 0.02558 kg/m^3, saturation vapor pressure of 3540 Pa and surface tension of 0.0717 N/m. The computational grid for the present study is same as the two-dimensional grids used for lift and drag prediction for the given hydrofoil and discussed earlier in Chapter 3. A no-slip, no-flux boundary condition to the velocity on the surface of the hydrofoil was applied along with a constant velocity at the inlet and pressure outlet at the outlet boundary.

The first objective of the current work deals with determination of minimum resultant flow velocity given by Eq. (2.11) for the onset of cavitation. For a fixed angle of attack (α), the flow inlet velocity was therefore varied between 11.5 m/s and 14 m/s to observe the minimum velocity when the exit pressure was set at zero gauge pressure (See

Figure 4.23). It was observed from that a flow velocity of 12 m/s enables formation of vapor bubbles on the suction surface of the hydrofoil initiating cavitation. Further increase in flow velocity or decrease in cavitation number results in increased percentage of vapor faction volume which results in a larger cavity length on the hydrofoil surface. However, for a constant flow velocity, increase in gauge pressure gradually eliminates the possibility of the onset of cavitation as shown in Figure 4.24. When gauge pressure (P_{gauge}) is increased from zero to 20 kPa for two different flow velocities, the vapor volume fraction decreases in both cases showing less tendency of forming vapor bubbles due to the higher static pressure on the hydrofoil surface.

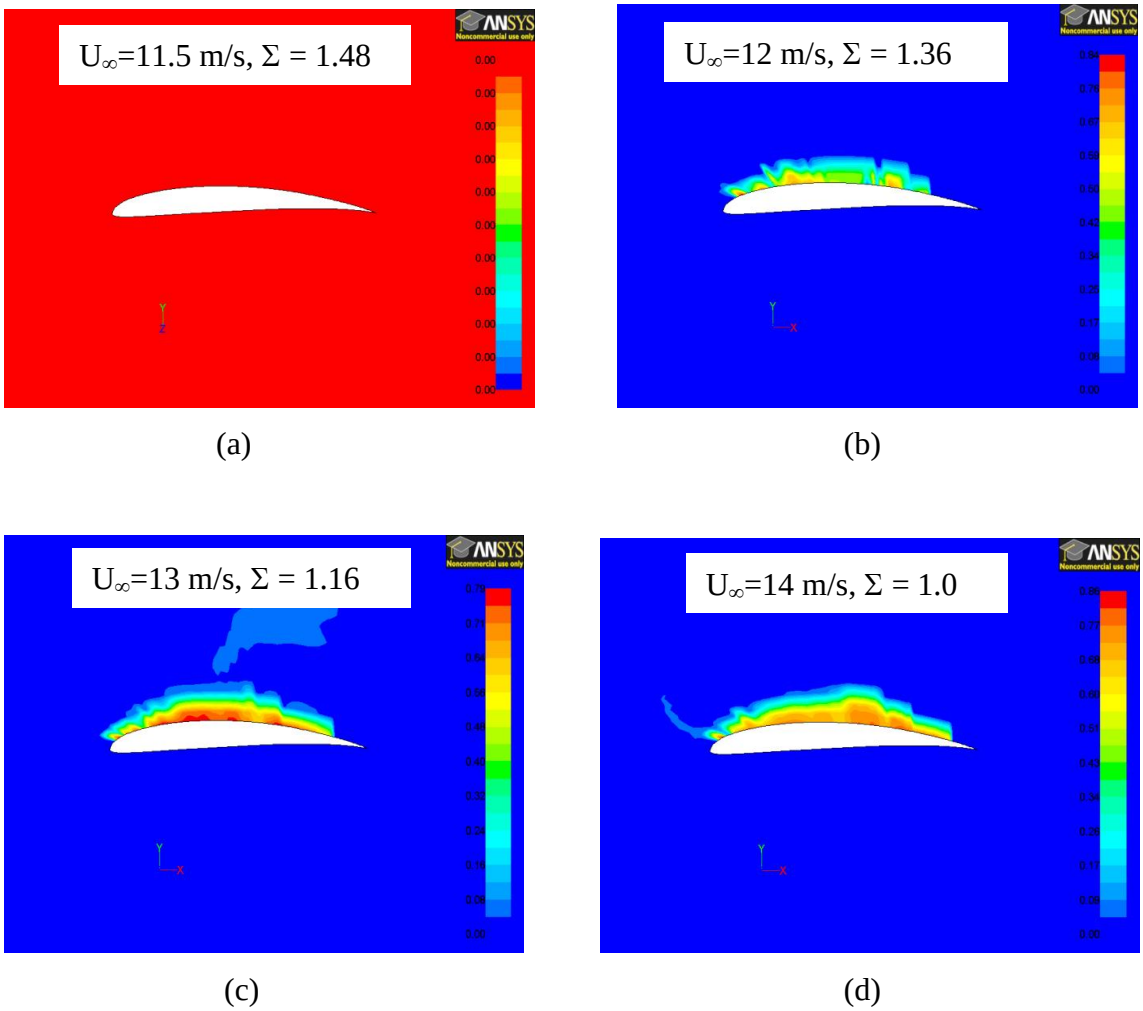

(a) (b)

(c) (d)

Figure 4.23. Computed vapor volume fraction contours at different flow conditions

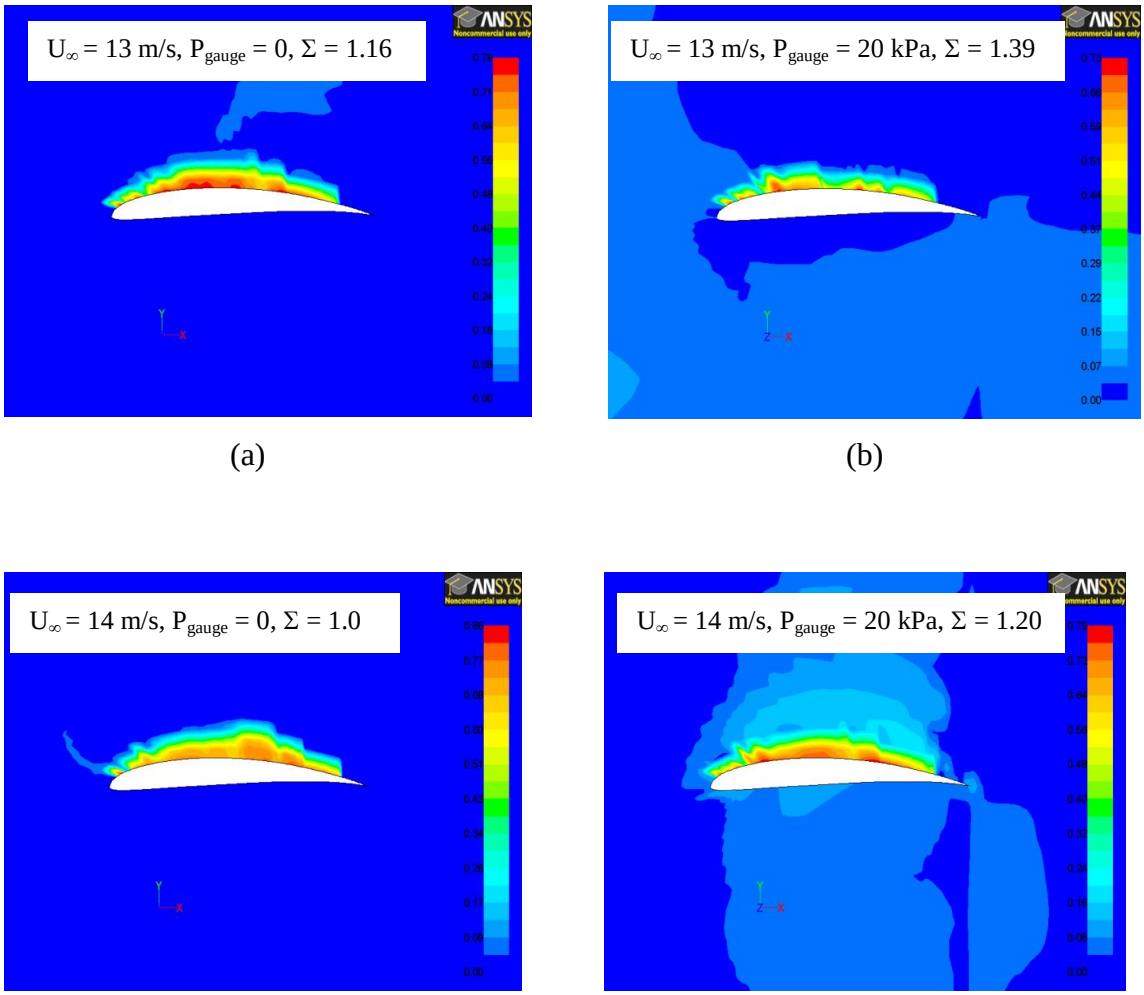

(a) (b)

(c) (d)

Figure 4.24. Computed vapor volume fraction distributions at different cavitation numbers for different gauge pressure (P_{gauge})

4.4.2. Effect of angle of attack. For a fixed Σ = 1.36, the flow α was varied between 0° and 6°. The results are shown in Figure 4.25, at lower values of α (0° and 2°) no vapor formation was observed at the hydrofoil surface. However, as α increases beyond 4° formation of vapor bubbles can be observed on the suction surface. As α increases the vapor region moves to the front (upstream) of the hydrofoil and length of the cavity grows in size on the upper surface of the hydrofoil. Therefore, it can be concluded that a hydrofoil is subjected to cavitation when the incoming flow speed reaches 12 m/s or angle of attack becomes more than 4° for a given Σ. For a river water speed of 2 m/s, depending on the TSR, the maximum incoming flow speed for our numerical case varied between 3.5-9.5 m/s which shows no cavitation will occur when such turbines are placed inside rivers.

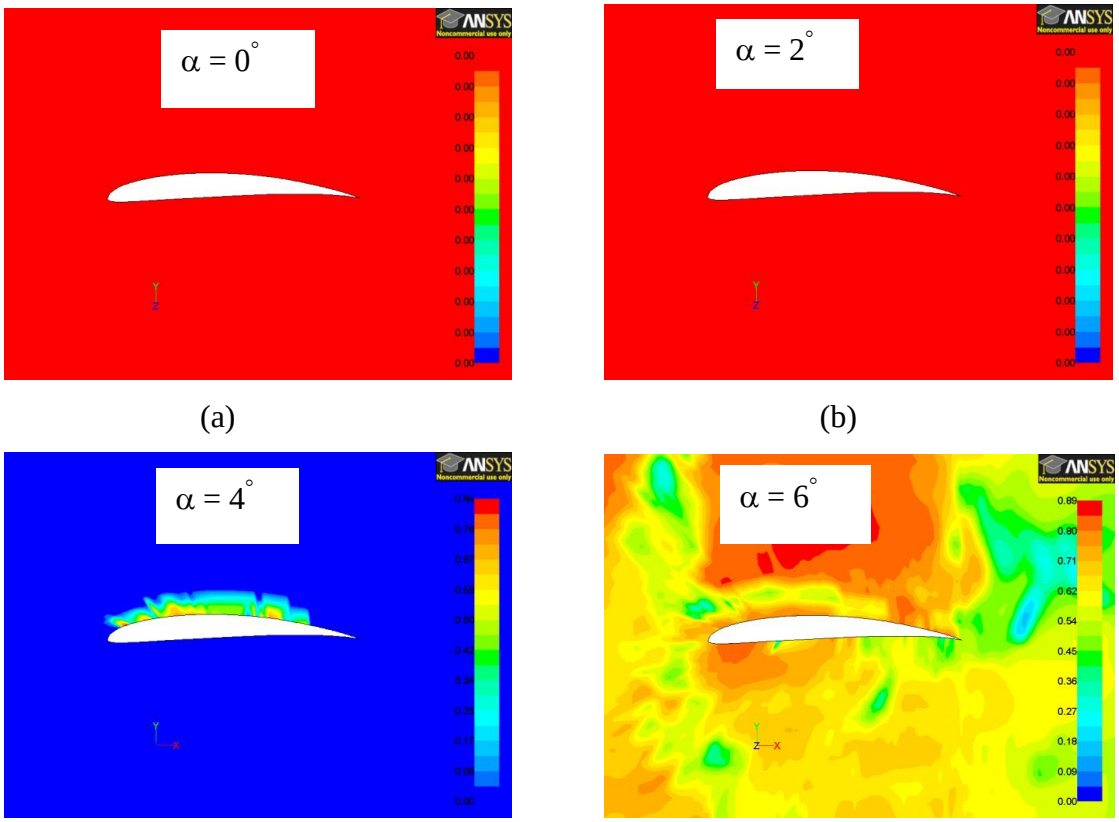

Figure 4.25. Computed vapor volume fraction distributions at different cavitation numbers for different angles of attack (U_{rel} = 12 m/s)

5. CONCLUSIONS AND FUTURE WORK

5.1. SUMMARY

The primary objectives of the current work deals with review of basic hydrokinetic systems and understand the hydrodynamics associated with its principle of operation. A CFD-RANS finite volume methodology has been applied to solve the flow conditions. The numerical modeling employs a rotating reference frame methodology to transform an unsteady flow in an inertial (stationary) frame to a steady flow in a non-inertial (moving) reference frame. The effect of several non-dimensional hydrodynamic parameters on the turbine performance has been analyzed. The numerical results were validated with both theoretical Blade Element Momentum theory using water and with experimental observation using air as working fluid. The numerical results showed good consistency with both the theoretical and experimental model and depending on the accuracy of validation, they provide strong foundation for future modeling purpose. The effects of each of the non-dimensional quantities such as TSR, solidity, number of blades ad Reynolds number need to be carefully analyzed to increase the efficiency of the hydrokinetic turbines. The detailed significant findings are summarized as below:

(a) Numerical investigations were performed using both two-dimensional (stationary) and three-dimensional (rotating) models to examine the performance of HAHkTs under different turbine solidities ranging 0.064 - 0.127, angle of attack 0° - 20° and blade numbers 2 - 4. The validation of the numerical studies were performed using BEM theory which considers two dimensional lift and drag characteristics to determine the turbine loading under different flow TSR.

(b) The results obtained from BEM theory offer good agreement for attached flows on the surface of the blades. In other words, for higher TSR the numerical results match consistently with the theoretical model. However, for lower TSR, BEM theory is inadequate and under-predict the turbine rotor power output when the blades are subjected to stalled condition.

(c) The discrepancies observed between the BEM and three-dimensional numerical models result from the turbine rotation which causes stall-delay phenomenon in

the latter case under the combined effect of span-wise radial acceleration and chord-wise coriolis acceleration. This results in increased lift coefficient and hence greater C_P for three-dimensional case when compared with two-dimensional data.

(d) Three different turbulence models such as one-equation Spalart-Allmaras model, two-equation Realizable k-ε model and two-equation k-ω SST models were chosen for two-dimensional numerical modeling of HAHkT. The results suggest an optimum angle of attack of 14° corresponding to maximum lift for SG-6043 hydrofoil whereas a 2° angle of attack indicates point of maximum lift to drag ratio. The increased camber in SG-6043 resulted in increase in C_L compared to NACA-2412 under same operating condition. The k-ω SST model yielded the most accurate C_L values when compared to the BEM theory due to its improved formulation for predicting the adverse pressure gradient in hydrofoil flows.

(e) The three-dimensional results for optimum design have suggested a strong dependence of maximum C_P on TSR when different turbine geometries (i.e. solidity, angle of attack and number of blades) are being considered. Increase in turbine solidity and blade numbers results in increased C_P under the entire operating range of TSR studied with maximum C_P observed in lower TSR.

(f) Finally, the axial, radial and tangential velocity distribution along the radial distance at one rotor diameter downstream location has been investigated. The effect of stall-delay phenomenon in three-dimensional model has been confirmed when compared stationary two-dimensional case indicating delay of separation at further trailing edge of the hydrofoil. In addition, a lesser axial velocity deficit and hence a lesser energy loss at higher TSR further confirms higher C_P of HAHkTs. The axial velocity deficit behind the turbine rotor confirms the expansion and decay of wake phenomenon. The width of the wake increases and axial velocity deficit decreases with increase in downstream distance.

(g) A hydrofoil is subjected to cavitation when the incoming flow speed reaches 12 m/s or angle of attack becomes more than 4° for a given cavitation number.

5.2. FUTURE WORK

The numerical analysis performed in the present work consists of constant chord, constant pitch turbine geometry. However, advanced turbine blade geometries would involve development of variable chord, variable pitch geometries similar to the actual wind turbine blades. Future work will involve the following:

***Hydrodynamics*:** Numerical modeling of variable chord and variable pitch turbine geometries (see Figure 5.1) will be useful to obtain more efficient and innovative blade profiles. In addition, transient modeling of two-dimensional hydrofoil needs to be performed to investigate the dynamic stall effects under turbine rotation. Furthermore, incorporation of diffuser around the turbine will be another challenging task and numerical investigation will be required to design the diffuser such that an increased power extraction can be achieved.

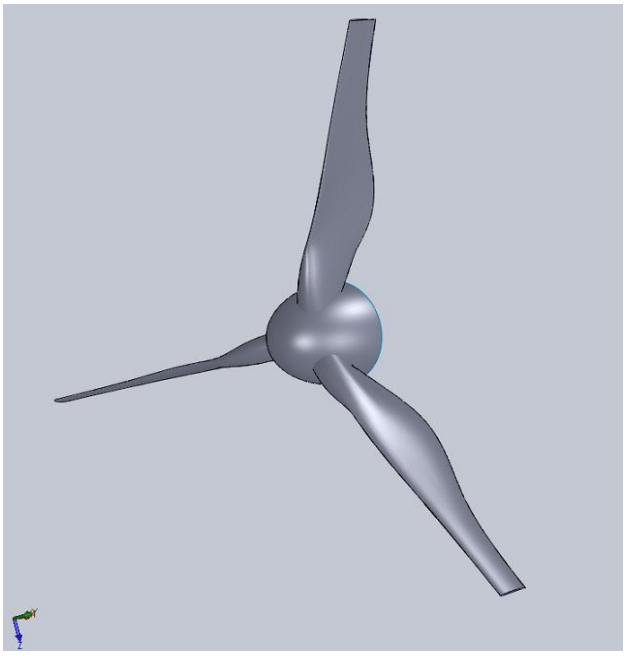

Figure 5.1. Variable chord turbine blade geometries using hydrofoil sections FX-77 W343 and SG-6043 (from hub to tip)

***Multivariate Design Optimization*:** The two fundamental objectives of the design of hydrokinetic turbines deal with maximizing Annual Energy Production (AEP) and minimizing Cost of Energy (COE). In order to solve such multi-objective problem, a

multivariate optimization method is required to search for the Pareto-optimal design solutions with respect to AEP and COE. The method will be based on the coupling of hydrodynamic model implementing the blade element momentum theory and an evolutionary algorithm which will attempt to address general indications for the choice of fundamental decision parameters that will enable maximum AEP density at minimum COE. A preliminary optimization analysis was performed and is provided in Appendix B.

***Structural Aspects*:** Materials selection plays a pivotal role in decreasing the overall cost and weight of the turbine while performing at maximum efficiency [82-84]. A computer based system developed by Ashby *et al*. known as Cambridge Engineering System (CES) will be applied to ensure that the task was performed effectively and the decision making process was carried out in selection of materials from the vast number of materials that are available in literature. The concept of material and process attributes are considered which are mapped on material and process selection chart to obtain potential candidate materials for that purpose. The choice behind selection of appropriate materials is governed by primary design constraints (non-negotiable, essential conditions) which include tensile and fatigue strength of materials, fatigue endurance, fracture toughness, corrosion resistance etc. and secondary design constraint (negotiable but desirable) that include materials cost. Since most of the material selection problems consist of more constraints than free variables, a systematic multiple constraint principle needs to be implemented in order to account for such situations. Furthermore, quite often the selection involves conflicting objectives where the mass needs to be minimized while at the same minimizing cost as well which essentially require the use of trade-off methods.

***Prototypes testing and model validation*:** Once the hydrodynamic, structural and materials performance analysis is performed for a HAHkT of rated power capacity, a prototype needs to be built depending on the given design parameters and water channel dimensions in which it is going to be tested. The prototype testing will help to validate the results obtained from existing theoretical and numerical models for a given flow condition and will also provide a strong foundation before it is scaled up for real life applications.

APPENDIX A.

BLADE ELEMENT MOMENTUM THEORY

A1. BLADE ELEMENT MOMENTUM THEORY

Blade element momentum theory was used to validate the numerical model of HAHkT. However, in order to obtain the axial (a) and angular (a') induction factors, iterative solution method is sought. The method starts with initial guesses for a and a' from which the flow conditions and new induction factors are calculated. The procedure consists of 4 steps:

(a) Guess value of a and a'
(b) Calculate the angle of relative fluid flow.
(c) For a given pitch turbine blade, calculate the angle of attack and corresponding C_L
(d) Update a and a'

The process is then repeated until the newly calculated induction factors are within some acceptable tolerance of the previous ones. A MATLAB code was written for this purpose which enables calculation of C_P using BEM theory. The expression for C_L can be obtained using a curve-fit function on from is obtained by using a curve fitting function on Figure 4.8. A 4th order polynomial function has been approximated with a R^2 value of 0.9994 as shown in Figure A1.

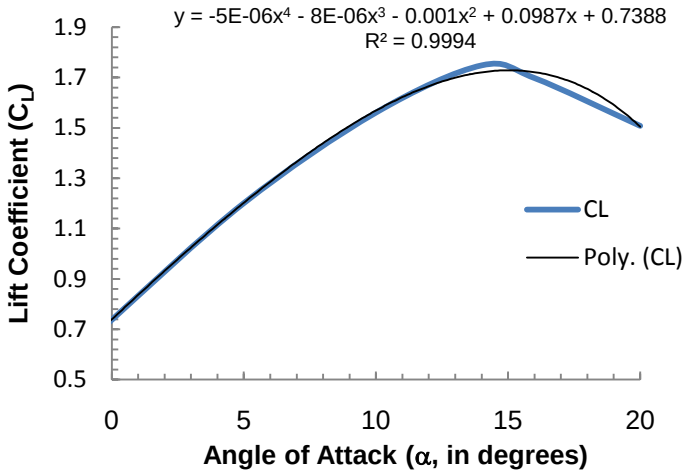

Figure A1. Curve-fitting of the C_L vs. α plot for SG-6043 hydrofoil

MATLAB CODE

```
clear all;
% number of blades
n = 3.0;
% fuid velocity in m/s
V = 2.0;
% Rotational velocity in rad/sec
omega = 6.0;
%  constant chord length in meters
c = 0.2;
% turbine radius in meters
r =0.3;
% hub and tip distance in terms of radius in meters
xs = 0.1*r;
xt = r;
% define solidity
sigma = (n*c)/(2.0*pi*r);
% initial guess
lambda = (r*omega)/V;
lambda
phi= (2.0/3.0)*(atan(1/lambda))*(180/pi);
theta = 10; % setting pitch angle
alpha = phi-theta;
alpha;
% determination of lift and drag coefficient
cl=-(0.000005*(alpha)^4)-(0.000008*(alpha)^3)-(0.001*(alpha)^2) + (0.0987*(alpha)) + 0.7388;
%cd=(0.0000002*(alpha)^5)-
(0.0000033*(alpha)^4)+(0.000002*(alpha)^3)+(0.0003*(alpha)^2)+(0.001*alpha)+0.0134;
cl;
%initial guess of axial and angular induction factors
a0 = 1.0/(1.0+((4.0*sin(phi*pi/180)*sin(phi*pi/180))/(sigma*cl*cos(phi*pi/180))));
b0 = 1.0/((4.0*cos(phi*pi/180)/(sigma*cl))-1.0);
% subsequent iterations
finished=0;
sum=1;
while (finished==0)
exp = (1.0-a0)/((1.0+b0)*lambda);
phi1=(atan(exp))*(180.0/pi);
alpha1 = phi1-theta;
alpha1;
clnew=-(0.000005*(alpha1)^4)-(0.000008*(alpha1)^3)-(0.001*(alpha1)^2) + (0.0987*(alpha1)) + 0.7388;
% p1 and p2 are the recalculated axial and angular induction factors
p1=1.0+((4.0*sin(phi1*pi/180)*sin(phi1*pi/180))/(sigma*clnew*cos(phi1*pi/180)));
p2=(4.0*cos(phi1*pi/180)/(sigma*clnew))-1.0;
anew=1/p1;
bnew=1/p2;
 if (abs(anew-a0)<1.0e-3),
   if (abs(bnew-b0)<1.0e-3),
    finished=1;
   end;
  end;
```

```
  a0=anew;
  b0=bnew;
  sum=sum+1;
  if (sum>5),
   finished=1;
  end;
end;
anew
bnew
out=((lambda)^3)*(1-anew)*bnew;
out
```

APPENDIX B.

HYDRODYNAMIC OPTIMIZATION THEORY

B1. HYDRODYNAMIC OPTIMIZATION THEORY

The hydrodynamic design of a horizontal axis hydrokinetic turbine is a complex procedure which is characterized by several trade-off decisions to obtain an optimum efficiency of the system. The success of the optimization design is however, dependent on the definition of the design objectives and limitations of the solution space. The definition of the solution space is again dependent on the extent of freedom of the design variables. As mentioned in section 2.2.1, the hydrodynamic performance of HAHkT is primarily governed by tip-speed ratio, solidity, Reynolds number and number of blades. It is well understood that these parameters play a key role in determining the overall hydrodynamic performance of HAHkT. However, it is not yet ascertained that which combination of the parameters need to be selected to achieve most optimized design based on the efficiency. The two fundamental objectives that are associated with design of hydrokinetic system are to maximize the Annual Energy Production (AEP) and to minimize the Cost of Energy (COE). For a given COE, a rotor should be designed in such a manner that will provide maximum AEP. On the other hand, the entire system should have a lower COE for a given AEP. The COE is a general figure of merit and it leads to a homogeneous comparison between different turbines. On the other hand, AEP depends strongly on the turbine size and rated power of the system which is again dependent on the hydrodynamics associated with the operation of the turbines. Therefore, in order to obtain a more optimized design configuration for our present study, the influence of the above mentioned variables on the governing hydrodynamic model needs to be understood. BEM model is used for this purpose to calculate the hydrodynamic performance of such turbines where the design variables are rated power of the turbine, the radius, chord length and pitch angle distribution. The improvement or optimization of the existing design is rated in terms of Power Coefficient (C_P) of the turbine. In addition, the turbine rotor is designed to follow a power curve for a range of rotational speed of the turbine under a given flow condition. The following section will provide more details regarding the hydrodynamic optimization procedure for the present study.

B2. OPTIMIZATION METHODOLOGY

As a starting point for the hydrodynamic optimization, a three-bladed HAHkT turbine rotor can be modeled as a single blade entity with four radial stations. These radial stations were selected along the blade radius: (1) at 25% radius, (2) at 50% radius, (3) at 75% radius and (4) 95% radius. The turbine rotor model was simplified by choosing some geometric characteristics of the rotor as constants and others as design variables. A constant rotor radius of 1m and inlet flow speed of 2 m/s was chosen as a reference design. The design rotational speed is selected between 3-10 rad/s based on the minimum and maximum RPM that the turbine blades will be rotating under given river current speed. The chord length and pitch angle distributions along the blade become the design variables for rotor optimization. These rotor design variables are modulated to achieve the peak hydrodynamic performance possible for the rotor in the design rotational speed range. Once the initial values, chord and pitch distributions are provided, the angle of attack (α) is calculated and MATLAB was used to calculate the resultant rotor power output and C_P using BEM theory taking both Prandtl tip-loss and Glauert's correction factor under turbulent wake state. Table A1 provides the summary of the design variables for rotor optimization. The pitch angle or twist distribution determines the angle at which the hydrofoil profile "sees" the fluid flow. The local angle of attack at a radial point is the difference between the angle of relative flow and the pitch angle. As the rotational speed increases from root to tip of a blade, the flow angle decreases. Assuming that the hydrofoil profiles used at the radial stations experience their peak lift values in a similar angle of attack range, the typical fixed-pitch hydrokinetic turbine blade will have a pitch angle distribution which is greater at the root of the blade and smaller near the tip. Knowing the extents of the river water speed, rotational speed range and a particular hydrofoil, it is possible to estimate the range of flow angles and thus angles of attack to be encountered at each radial station. For the present case, the angle of attack is chosen to be 14° as obtained from lift characteristics in Chapter 4. The MATLAB code for the hydrodynamic optimization routine is given below. The power curve from the hydrodynamic optimization of the given turbine blades is shown in Table B1. The maximum C_P of ~ 0.45 can be observed for a corresponding TSR = 4.25 showing

significant improvement when compared with constant-chord and fixed pitch turbine blades.

Table B1. Design variables for the rotor optimization

Design Variables	**Design Value**	**Minimum Value**	**Maximum Value**
Radius (m)	1	NA	NA
River speed (m/s)	2	NA	NA
Rotational speed (rad/s)	NA	3	10
Chord (1) (m)	0.25	0.245	0.255
Chord (2) (m)	0.26	0.14	0.37
Chord (3) (m)	0.17	0.09	0.255
Chord (4) (m)	0.12	0.074	0.17
Pitch angle (1) (deg)	20	16	25
Pitch angle (2) (deg)	8	4	12
Pitch angle (3) (deg)	1.5	-2	5
Pitch angle (4) (deg)	-2	-5	1

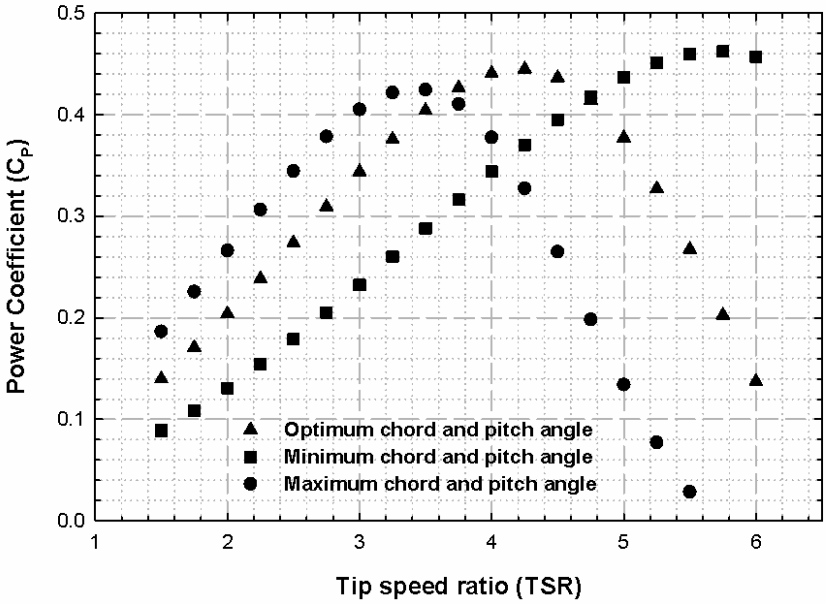

Figure B1. The power coefficient plot for different TSR using variable chord and variable pitch turbine blades

MATLAB CODE

```
% performance evaluation of horizontal axis hydrokinetic turbine
% Inputs: Rotor radius = R (in meters)
% flow speed = V (in m/s)
% Design variables: chord distribution and pitch distribution
% Output power coefficient (CP)
% chord distribution
clc
clear all
R = 1;
V = 2;
%axif = 0.1 % initial guess of axial induction factor
%atif = 0.1 % initial guess of angular induction factor
N = 3; % Number of blades
visc = 0.001; % dynamic viscosity of water in kg/ms
rho = 998.2; % density of water in kg/m3
omega = 3:0.5:10; % rotational velocity in rad/s with increment of 0.5 units
tsratio = omega*R./V;
len = length(omega);
ac = 0.2; % glauert's thrust correction factor
```

```
 % constant influencing magnitude of blade chord
% radius distribution along the span of the blade with r = r/R
r = [0.25 0.5 0.75 0.95];
chord=[0.25 0.26 0.17 0.12]; %chord length in meters
pitch=[20 8 1.5 -2]; %pitch angle in degress
% chord = a*(r/R)^b; %chord length as a function of radius at local section
%r = r*R; %radius distribution (m)
rhub = 0.1*R;
dr(1)=(r(1)+r(2))/2-rhub;
dr(2)=((r(2)+r(3))/2)-((r(1)+r(2))/2);
dr(3)=((r(3)+r(4))/2)-((r(2)+r(3))/2);
dr(4)=R-((r(3)+r(4))/2);
%initialize the matrices
rmat=zeros(4,len);
chordmat=zeros(4,len);
omegamat=zeros(4,len);
axif=zeros(4,len);
atif=zeros(4,len);
Re=zeros(4,len);
pitch=zeros(4,len);
alphamat=zeros(4,len);
phimat=zeros(4,len);
clmat=zeros(4,len);
cdmat=zeros(4,len);
constmat=ones(4,len);
CT=zeros(4,len);
tolaxmat=zeros(4,len);
tolatmat=zeros(4,len);
ratiomat=zeros(4,len);
Fmat=zeros(4,len);
drmat=zeros(4,len);
rmat(1,:)=r(1);
rmat(2,:)=r(2);
rmat(3,:)=r(3);
rmat(4,:)=r(4);
chordmat(1,:)=chord(1);
chordmat(2,:)=chord(2);
chordmat(3,:)=chord(3);
chordmat(4,:)=chord(4);
pitch(1,:)=pitch(1);
pitch(2,:)=pitch(2);
pitch(3,:)=pitch(3);
pitch(4,:)=pitch(4);
drmat(1,:)=dr(1);
drmat(2,:)=dr(2);
drmat(3,:)=dr(3);
drmat(4,:)=dr(4);
%Initialize induction factors
for i=1:4 %number of radial stations
  omegamat(i,:)=omega;
  for j=1:len
     tsr=omega(j).*r(i)./V;
     m=(9-3*(tsr)^2);
     n=((tsr)^2-1);
     coeff=[16 -24 m n];
     p=roots(coeff);
```

```
        p=sort(p);
        axif(i,j)=p(2);
        atif(i,j)=(1-3.*axif(i,j))/(4.*axif(i,j)-1);
    end
end
finished=0
iter=1;
axifmat=cell(1,5);
atifmat=cell(1,5);
axifmat{1}=axif;
atifmat{1}=atif;
while (finished==0)
    %calculation of angle of attack
    phimat=atan(V.*(1-axif)./((1+atif).*omegamat.*rmat));
    phideg=phimat*180/pi;
    alphamat=phimat-pitch;
    Vrot=omegamat.*rmat.*(1+atif);
    Vax=V.*(1-axif);
    Vrel=sqrt(Vrot.^2+Vax.^2);
  %Re=(chordmat*rho*Vrel)/visc
  %calculation of lift and drag coefficient
  for i=1:4
      for j=1:len
 clmat=-(0.000005.*(alphamat).^4)-(0.000008.*(alphamat).^3)-(0.001.*(alphamat).^2) +
0.0987.*alphamat+0.7388.*constmat;
 cdmat=(0.0000002.*(alphamat).^5)-
(0.0000033.*(alphamat).^4)+(0.000002.*(alphamat).^3)+(0.0003.*(alphamat).^2)+0.001.*alphamat+0.013
4.*constmat;
      end
  end
  f=0.5*N*(R-rmat)./(rmat.*sin(phimat));
  F=2/pi.*acos(exp(-f)); %Prandtl's tip loss factor
  solidity=N*chordmat./(2*pi.*rmat);
  cn=(clmat.*cos(phimat))+(cdmat.*sin(phimat)); %calculation of normal forces
  ct=(clmat.*sin(phimat))-(cdmat.*cos(phimat)); %calculation of tangential forces
  %Recalculation of induction factors
  atifnew=(4.*F.*sin(phimat).*cos(phimat)./(solidity.*ct)-1).^-1;
  k=4*F.*sin(phimat).^2./(solidity.*cn);
  for j=1:len
      for i=1:4
          if axif(i,1)<= ac %Glauert's correction factor for high values of ax induction factor
              axifnew(i,j)=(k(i,j)+1)^-1;
          else
              axifnew(i,j)=0.5*(2+k(i,j)*(1-2*ac)-sqrt((k(i,j)*(1-2*ac)+2)^2+4*(k(i,j)*ac^2-1)));
          end
      end
  end
  tolax=abs(axif-axifnew);
  tolat=abs(atif-atifnew);
  if tolax<0.0001,
      if tolat<0.0001,
          finished=1;
      end
  end
  axif=axifnew;
  atif=atifnew;
```

```
  iter=iter+1;
  if (iter>5)
     finished=1;
  end
  axifmat{iter}=axif
  atifmat{iter}=atif;
end
%calculation of power coefficient
tsr =omegamat.*rmat./V;
dtsr=omegamat.*drmat./V;
CT=(1-axifnew).^2.*cn.*solidity./(sin(phimat).^2);
FT=0.5*rho*Vrel.^2.*chordmat.*(clmat.*sin(phimat)-cdmat.*cos(phimat));
dM=rmat*N.*FT.*drmat;
dP=omegamat.*dM;
P=sum(dP);
CP=sum(dP)./(0.5*rho*V.^3*pi*R^2);
ratio=clmat./cdmat;
CP
```

BIBLIOGRAPHY

[1] "Annual Energy Outlook Early Release Overview," 2010.

[2] R. Newell, "Annual Energy Outlook 2010 Reference Case," The Paul H.Nitze School of Advanced International Studies, Washington, D.C.2009.

[3] "http://www.eia.doe.gov/oiaf/aeo/assumption/pdf/renewable.pdf," *US Energy Information Administration, Annual Energy Outlook-2010*, 2010.

[4] R. Bedard, "Overview of U.S. Ocean Wave and Current Energy: Resource, Technology, Environmental and Business Issues and Barriers ", Electric Power Research Institute2007.

[5] *http://www.usbr.gov/lc/hooverdam/*.

[6] I. S. Hwang, *et al.*, "Optimization of cycloidal water turbine and the performance improvement by individual blade control," *Applied Energy*, vol. 86, pp. 1532-1540, 2009.

[7] A. Date and A. Akbarzadeh, "Design and cost analysis of low head simple reaction hydro turbine for remote area power supply.," *Renewable Energy*, vol. 34, pp. 409-415, 2009.

[8] F. Giudice and G. L. Rosa, "Design, prototyping and experimental testing of a chiral blade system for hydroelectric microgeneration," *Mechanism and Machine Theory*, vol. 44, pp. 1463-1484, 2009.

[9] O. Paish, "Micro-hydropower: status and prospects," *Proceedings of Institution of Mechanical Engineers, Part A: Journal of Power and Energy*, vol. 216, pp. 31-40, 2002.

[10] K. V. Alexander and E. P. Giddens, "Microhydro: Cost-effective, modular systems for low heads," *Renewable Energy*, vol. 33, pp. 1379-1391, 2008.

[11] K. V. Alexander, *et al.*, "Axial flow turbines for low head microhydro systems," *Renewable Energy*, vol. 34, pp. 35-47, 2009.

[12] K. V. Alexander, *et al.*, "Radial and mixed flow turbines for low head microhydro systems," *Renewable Energy*, vol. 34, pp. 1885-1894, 2009.

[13] M. J. Khan, *et al.*, "River current energy conversion systems: Progress, prospects and challenges," *Renewable and Sustainable Energy Reviews*, vol. 12, pp. 2177-2193, 2008.

[14] M. J. Khan, *et al.*, "Hydrokinetic energy conversion systems and assessment of horizontal and vertical axis turbines for river and tidal applications: A tecnology status review," *Applied Energy*, vol. 86, pp. 1823-1835, 2009.

[15] "Proceedings of the Hydrokinetic and Wave Energy technologies technical and environmental issues workshop," Washington, D.C.2006.

[16] W. M. J. Batten, *et al.*, "The prediction of the hydrodynamic performance of marine current turbines," *Renewable Energy*, vol. 33, pp. 1085-1096, 2008.

[17] J. F. Manwell, *et al.*, *Wind Energy Explained: Theory, Design and Application*. New York: John Wiley and Sons., 2002.

[18] "http://www.enchantedlearning.com/usa/rivers/."

[19] E. Amromin, *et al.*, "Hydrofoil drag reduction by partial cavitation," *Journal of Fluids Engineering*, vol. 128, pp. 931-936, 2006.

[20] L. Myers and A. S. Bahaj, "Power output performance characteristics of a horizontal axis marine current turbine," *Renewable Energy*, vol. 31, pp. 197-208, 2006.

[21] W. M. J. Batten, *et al.*, "Hydrodynamics of marine current turbines," *Renewable Energy*, vol. 31, pp. 249-256, 2006.

[22] A. S. Bahaj, *et al.*, "Experimental verifications of numerical predictions for the hydrodynamic performance of horizontal axis marine current turbines," *Renewable Energy*, vol. 32, pp. 2479-2490, 2007.

[23] B. Kirke and L. Lazauskas, "Variable pitch Darrieus water turbines," *Journal of Fluid Science and Technology*, vol. 3, pp. 430-438, 2008.

[24] J. Zanette, *et al.*, "A design methodology for cross flow water turbines," *Renewable Energy*, vol. 35, pp. 997-1009, 2010.

[25] C. A. Consul, *et al.*, "Influence of solidity on the perfromance of a cross-flow turbine," in *Proceedings of the 8th European Wave and Tidal Energy Conference*, Uppsala, Sweden, 2009, pp. 1-10.

[26] S. L. Dixon, *Fluid Mechanics and Thermodynamics of Turbomachinery*, 5 ed. Burlington, MA,USA: Elsevier Butterworth Heinemann, 2005.

[27] P. Garman, "Water current turbines: Providing pumping, power in remote areas," *Hydro Review Worldwide*, vol. 6, pp. 24-28, 1998.

[28] L. Rutten, "Au fil de l'eau, une roue a aubes," *Systemes Solaires*, vol. 100, 1994.

[29] D. Levy, "Power from natural flow at zero static head," 1995.

[30] *Marlec Engineering Co Ltd.* Available: www.marlec.co.uk/index.htm

[31] "Technology evaluation of existing and emerging technologies-water current turbines for river current applications," Natural Resources, Canada2006.

[32] *Alternative Hydro Solutions Ltd.* Available: www.althydrosolutions.com

[33] "Hydro Green Energy," *http://www.hgenergy.com/index.html*.

[34] *Thropton Energy Services, UK*.

[35] *Underwater Electric Kite Corporation (USA).*

[36] D. Dixon, "Assessment of waterpower potential and development needs, Tech Report No-1014762," 2007.

[37] Available: http://www.windustry.org/how-much-do-wind-turbines-cost

[38] "Hydrokinetic Turbines in Canals: Potential and Reality," Seattle,WA.

[39] L. F. D. Gaden and E. L. Bibeau, "A numerical investigation into the effect of diffusers on the performance of hydrokinetic turbines using a validated momentum source model," *Renewable Energy*, vol. 35, pp. 1152-1158, 2010.

[40] D. Sale, *et al.*, "Hydrodynamic optimization method and design code for stall-regulated hydrokinetic turbine rotors," *28th ASME International Conference on Ocean, Offshore and Arctic Engineering*, 2009.

[41] W. M. J. Batten, *et al.*, "Hydrodynamics of marine current turbines," *Renewable Energy*, vol. 31, pp. 249-256, 2006.

[42] F. M. White, *Fluid Mechanics*: McGraw Hill Publishers, 1998.

[43] O. de Vries, "Fluid Dynamic Aspects of Wind energy conversion," *Advisory Group for Aerospace Research and Development, North Atlantic Treaty Organization, AGARD-AG-243*, 1979.

[44] B. Sanderse, "Aerodynamics of wind turbine wakes," 2009.

[45] M. O. L. Hansen, *Aerodynamics of wind turbines*: Earthscan Publications Limited, 2001.

[46] T. Burton, *et al.*, *Wind Energy Handbook*: John Wiley & Sons Limited, Chichester, 2001.

[47] L. J. Vermeer, *et al.*, "Wind turbine wake aerodynamics," *Progress in Aerospace Sciences*, vol. 39, pp. 467-510, 2003.

[48] J. D. Anderson, *Fundamental of Aerodynamics*: McGraw-Hill Book Company, 1984.

[49] D. Hu and Z. Du, "Near wake of a model horizontal axis wind turbine," *Journal of Hydrodynamics,* vol. 21, pp. 285-291, 2009.

[50] F. Massouh and I. Dobrev, "Exploration of the vortex wake behind of wind turbine rotor," *Journal of Physics: Conference Series,* vol. 75, pp. 012036 1-9, 2007.

[51] L. Myers and A. S. Bahaj, "Wake studies of a 1/30th scale horizontal axis marine current turbine," *Ocean Engineering,* vol. 34, pp. 758-762, 2007.

[52] D. Hu, *et al.*, "A study on stall-delay for horizontal axis wind turbine," *Renewable Energy,* vol. 31, pp. 821-836, 2006.

[53] E. P. N. Duque, *et al.*, "Numerical predictions of wind turbine power and aerodynamic loads for the NREL phase II combined experiment rotor," *American Institute of Aeronautics and Astronautics,* pp. 0038 1-9, 2000.

[54] J. L. Tangler, "The nebulous art of using wind-tunnel airfoil data for predicting rotor performance: Preprint," presented at the 21st ASME Wind Energy Conference, Reno, Nevada, 2002.

[55] N. Mandas, *et al.*, "Numerical prediction of horizontal axis wind turbine flow," in *European Wave Energy Conference,* Athens, Greece, 2006.

[56] J. D. Anderson, *Computational Fluid Dynamics: The basics with applications*: McGraw Hill International, 1995.

[57] "Ansys Fluent 12.0. Theory Guide," ed: Ansys. Inc., 2009.

[58] G. K. Batchelor, *An Introduction to Fluid Dynamics*: Cambridge University Press, Cambridge, England, 1967.

[59] D. C. Wilcox, *Turbulence modeling for CFD*. La Canada, CA: DCW Industries, 1993.

[60] D. C. Wilcox, "Multiscale model for turbulent flows," *American Institute of Aeronautics and Astronautics,* vol. 26, pp. 1311-1320, 1988.

[61] F. R. Menter, "Performance of popular turbulence models for attached and separated adverse pressure gradient flows," *American Institute of Aeronautics and Astronautics,* vol. 30, pp. 2066-2072, 1992.

[62] F. R. Menter, "Two-equation eddy-viscosity turbulence models for engineering applications," *American Institute of Aeronautics and Astronautics,* vol. 32, pp. 1598-1605, 1994.

[63] E. Ferrer and X. Munduate, "Wind turbine blade tip comparison using CFD," *The Science of Making Torque from Wind, Journal of Physics: Conference Series,* vol. 75, pp. 012005 1-10, 2007.

[64] P. Spalart and S. Allmaras, "A one-equation turbulence model for aerodynamic flows.," *American Institute of Aeronautics and Astronautics, Technical Report* vol. AIAA-92-0439, 1992.

[65] S. B. Pope, *Turbulent Flows*: Cambridge University Press, New York, 2000.

[66] B. E. Launder and D. B. Spalding, "The numerical computation of turbulent flows," *Computer Methods in Applied Mechanics and Engineering,* vol. 3, pp. 269-289, 1974.

[67] T. H. Shih, *et al.*, "A new k-ε eddy viscosity model for high Reynolds number turbulent flows - Model development and validation," *Computers and Fluids,* vol. 24, pp. 227-238, 1995.

[68] B. E. Launder and D. B. Spalding, "The numerical computation of turbulent flows " *Computer Methods in Applied Mechanics and Engineering,* vol. 3, pp. 269-289, 1974.

[69] P. Giguere and M. S. Selig, "New airfoils for small horizontal axis wind turbines," *Journal of Solar Energy Engineering,* vol. 120, pp. 108-114, 1998.

[70] M. M. Duquette, *et al.*, "Solidity and blade number effects on a fixed pitch, 50W horizontal axis wind turbine," *Wind Engineering,* vol. 27, pp. 299-316, 2003.

[71] M. M. Duquette and K. D. Visser, "Numerical implications of solidity and blade number on rotor performance of horizontal axis wind turbines," *Journal of Solar Energy Engineering,* vol. 125, pp. 425-432, 2003.

[72] http://www.ae.illinois.edu/m-selig/ads/coord_database.html [Online].

[73] S. Patankar, *Numerical Heat Transfer and Fluid Flow*: Hemisphere Publishing Corporation, USA, 1980.

[74] "Ansys Fluent 12.0 User's Guide, Ansys Inc.," ed, 2009.

[75] A. K. Singhal, *et al.*, "Mathematical basis and validation of the full cavitation model," *Journal of Fluids Engineering,* vol. 124, pp. 617-624, 2002.

[76] S. Huang, *et al.*, "Simulation of cavitating flow around a 2-D hydrofoil," *Journal of Marine Science and Applications,* vol. 9, pp. 63-68, 2010.

[77] M. M. Duquette and J. Swanson, "Solidity and blade number effects on a fixed pitch, 50W horizontal axis wind turbine," *Wind Engineering,* vol. 27, pp. 299-316, 2003.

[78] T. H. Shih, *et al.*, "A new k-ε eddy viscosity model for high Reynolds number turbulent flows-model development and validation," *Computers and Fluids,* vol. 24, pp. 227-238, 1995.

[79] P. Spalart and S. Allmaras, "A one-equation turbulence model for aerodynamic flows: Technical report," *American Institute of Aeronautics and Astronautics,* vol. AIAA-92-0439, 1992.

[80] R. Howell, *et al.*, "Wind tunnel and numerical study of a small vertical axis wind turbine," *Renewable Energy,* vol. 35, pp. 412-422, 2010.

[81] G. H. Schnerr and J. Sauer, "Physical and Numerical modeling of unsteady cavitation dynamics," *Fourth International Conference on Multiphase flow, New Orleans, USA,* 2001.

[82] M. F. Ashby, *Materials Selection in Mechanical Design*, 3rd ed. Oxford, UK: Elsevier-Butterworth-Heinemann, 2005.

[83] A. Thakker, *et al.*, "A novel approach to materials selection strategy case study: Wave energy extraction impulse turbine blade," *Materials and Design,* vol. 29, pp. 1973-1980, 2008.

[84] D. A. Griffin and T. D. Ashwill, "Alternative composite materials for megawatt-scale wind turbine blades: Design considerations and recommended testing," *American Institute of Aeronautics and Astronautics,* pp. 0696 1-11, 2003.

VITA

Suchi Subhra Mukherji was born in Calcutta (now Kolkata), India on 12th June, 1985. He received his BE in Mechanical Engineering from Jadavpur University, Kolkata, India in June, 2008. During his undergraduate studies, he did two internships; one at National Chemical Laboratory, Pune, India (2006) and the other at R&D Division of Tata Steel Limited, Jamshedpur, India (2007). In August 2008, he joined Missouri University of Science and Technology (formerly University of Missouri, Rolla) as a graduate research assistant. He received his M.S. degree in Mechanical Engineering from the Missouri University of Science and Technology, Rolla, Missouri, USA, in December 2010.

Suchi Subhra has published two conference papers and currently has two journal papers under review. He has been members of American Society of Mechanical Engineers (ASME) and American Physical Society (APS) both since 2008.